1-1-2014

Computational Modeling of Nanocrystal Superlattices

Mehdi Bakhshi Zanjani
University of Pennsylvania, mehdibakhshi1987@gmail.com

Recommended Citation

Bakhshi Zanjani, Mehdi, "Computational Modeling of Nanocrystal Superlattices" (2014). *Publicly Accessible Penn Dissertations*. 1201.
http://repository.upenn.edu/edissertations/1201

Computational Modeling of Nanocrystal Superlattices

Abstract

Nanocrystal superlattices (NCSLs) are materials formed by assembly of monodisperse nanocrystal building blocks that are tunable in composition, size, shape, and surface functionalization. Such materials offer the potential to realize unprecedented combinations of physical properties, however, theoretical prediction of such properties remains a challenge. Because of the different length scales involved in these structures, modeling techniques at different scales, from ab-initio methods up to continuum models, can be used to study their behavior. This presents a challenge of understanding when and for which properties we can use computationally inexpensive continuum or mesoscopic models and when we will have to use microscopic models. Our goal here is to develop models that can predict phononic and thermal properties of different NCSLs. This includes (1) predicting bulk mechanical properties of NCSLs such as Young's and bulk modulus which are related to the behavior of low frequency acoustic phonons (2) predicting phononic band gaps through finding phonon dispersion curves of NCSL (3) predicting thermal conductivity of NCSLs. We also study the topic of one-way phononic devices that can possibly be implemented with acoustic metamaterials such as NCSLs or phononic crystals in general. This idea of one-way phonon isolation is investigated in a theoretical framework by considering systems such as acoustic waveguides and low dimensional materials.

Degree Type

Dissertation

Degree Name

Doctor of Philosophy (PhD)

Graduate Group

Mechanical Engineering & Applied Mechanics

First Advisor

Jennifer R. Lukes

Keywords

Acoustic Metamaterials, Multiscale Modeling, Nanocrystal Superlattices, One-way isolation, Phonons, Thermal Conductivity

Subject Categories

Mechanical Engineering

COMPUTATIONAL MODELING OF NANOCRYSTAL SUPERLATTICES

Mehdi Bakhshi Zanjani

A DISSERTATION

in

Mechanical Engineering and Applied Mechanics

Presented to the Faculties of the University of Pennsylvania
in
Partial Fulfillment of the Requirements for the
Degree of Doctor of Philosophy

2014

Dr. Jennifer R. Lukes, Associate Professor of Mechanical Engineering and Applied Mechanics
Supervisor of Dissertation

Dr. Prashant K. Purohit, Associate Professor of Mechanical Engineering and Applied Mechanics
Graduate Group Chairperson

Dissertation Committee:
Dr. John L. Bassani, Professor of Mechanical Engineering and Applied Mechanics
Dr. Christopher B. Murray, Professor of Chemistry and Materials Science
Dr. Jennifer R. Lukes, Associate Professor of Mechanical Engineering and Applied Mechanics

Acknowledgments

I would like to thank Professor Jennifer R. Lukes for proposing and guiding this project. She has been a major source of motivation, encouragement, and useful advice throughout my graduate studies. She has also made many significant contributions to this dissertation and the technical papers from which it is based. I consider myself very lucky to have learned from her and been one of her students.

I would like to thank Professor Christopher B. Murray for his great guidance and many useful comments on different topics of my work and also for serving on my committee. I wish to thank Professor John L. Bassani for serving on my committee and for his helpful ideas for directing my research projects. I would like to thank Professor Nader Engheta for his great ideas and guiding me through different projects during my graduate studies. I would also like to thank Professor Marija Drndic, Professor Cherie R. Kagan, and Professor Jay Kikkawa, the engineering and applied sciences faculty from whom I have learned so much.

I am very thankful for the research support given to me by the current and former members of Professor Lukes' research group: Anuj Chaudhri, Jack Franklin, Neil Zuckerman, Ian Cosden, Drew Cheney, Paul Barclay, and Ruiyuan Ma. I am also thankful to

Arthur Davoyan, Soong Ju Oh, Taejang Paik, Nathaniel E. Berry, and Kimberly Venta for their great help in different collaborative projects. A very special thanks should be given to Hoda Heidari for caring for me and being my number one supporter during my graduate study. Finally, I am very grateful to my family, especially my parents, for their unconditional love and support.

This work has been funded by the National Science Foundation and the Office of Naval Research.

ABSTRACT

COMPUTATIONAL MODELING OF NANOCRYSTAL SUPERLATTICES

Mehdi Bakhshi Zanjani

Dr. Jennifer R. Lukes

Nanocrystal superlattices (NCSLs) are materials formed by assembly of monodisperse nanocrystal building blocks that are tunable in composition, size, shape, and surface functionalization. Such materials offer the potential to realize unprecedented combinations of physical properties, however, theoretical prediction of such properties remains a challenge. Because of the different length scales involved in these structures, modeling techniques at different scales, from ab-initio methods up to continuum models, can be used to study their behavior. This presents a challenge of understanding when and for which properties we can use computationally inexpensive continuum or mesoscopic models and when we will have to use microscopic models. Our goal here is to develop models that can predict phononic and thermal properties of different NCSLs. This includes (1) predicting bulk mechanical properties of NCSLs such as Young's and bulk modulus which are related to the behavior of low frequency acoustic phonons (2) predicting phononic band gaps through finding phonon dispersion curves of NCSL (3) predicting thermal conductivity of NCSLs. We also study the topic of one-way phononic devices that can possibly be implemented with acoustic metamaterials such as NCSLs or phononic crystals in general. This idea of one-way phonon isolation is investigated in a theoretical framework by considering systems such as acoustic waveguides and low dimensional materials.

Contents

Chapter 1

Introduction

1.1 Experimental and Theoretical Background

One of the exciting features of nanostructures is that matter organized at the nanoscale may have properties significantly different from the common bulk materials. These interesting size-dependent properties are related to a variety of physical phenomena such as high surface to volume ratio and thermal effects [1, 2]. Nanocrystal superlattices (NCSLs) constitute a novel type of nanoscale artificial solids whose properties are determined both by individual nanocrystal building blocks and by their collective interactions [3]. Self-assembly of monodisperse nanocrystals yields an enormously rich variety of superlattice structures [3]. These superlattices are typically formed from assembly of building blocks in the 1-10 nm size range, which then organize into larger domains with sizes around hundreds of nanometer or even few microns. Figure 1.1 shows a schematic demonstration of NCSLs. The nanocrystals themselves consist of hundreds to thousands of core atoms of one or two types, such as Au, Pb, Se, and Cd that are spaced angstroms apart and surrounded by long hydrocarbon chains of capping ligands such as oleic acid and hexylthiol.

The unique properties of these materials may be fine-tuned to be used for specific purposes. In order to be able to synthesize and manipulate matter at the nanoscale, however, high precision tools and complicated synthesis methods are required in order to measure and modify the physical and chemical characteristics of these nanostructures. Several previous studies have successfully investigated the synthesis and experimental characterization of nanocrystal superlattices of different shapes, sizes, and compositions [4, 5, 3, 6, 7, 8, 9]. In these studies, TEM images show ordered structures of nanocrystals extended over fairly large domains. Structural characterization of these superlattices show a large variety of metamaterials with precisely controlled composition and tight placement of components. Structural properties of nanocrystal superlattices have also been studied theoretically through predicting energetically and entropically favorable arrangement of nanocrystals based on models at different scales [10, 11, 9, 5]. However, other physical properties such as mechanical, phononic, and thermal properties of these materials have just been considered in limited previous studies [12, 13].

1.2 Motivating Applications

Colloidal semiconductor nanocrystals have attracted broad interest due to their composition, size, and shape tunability. They possess many interesting electronic and optical properties [14, 15, 16] and have been used for applications such as transistors and circuits, light-emitting devices, photodetectors and solar cells [17, 18, 19, 20, 21]. Another

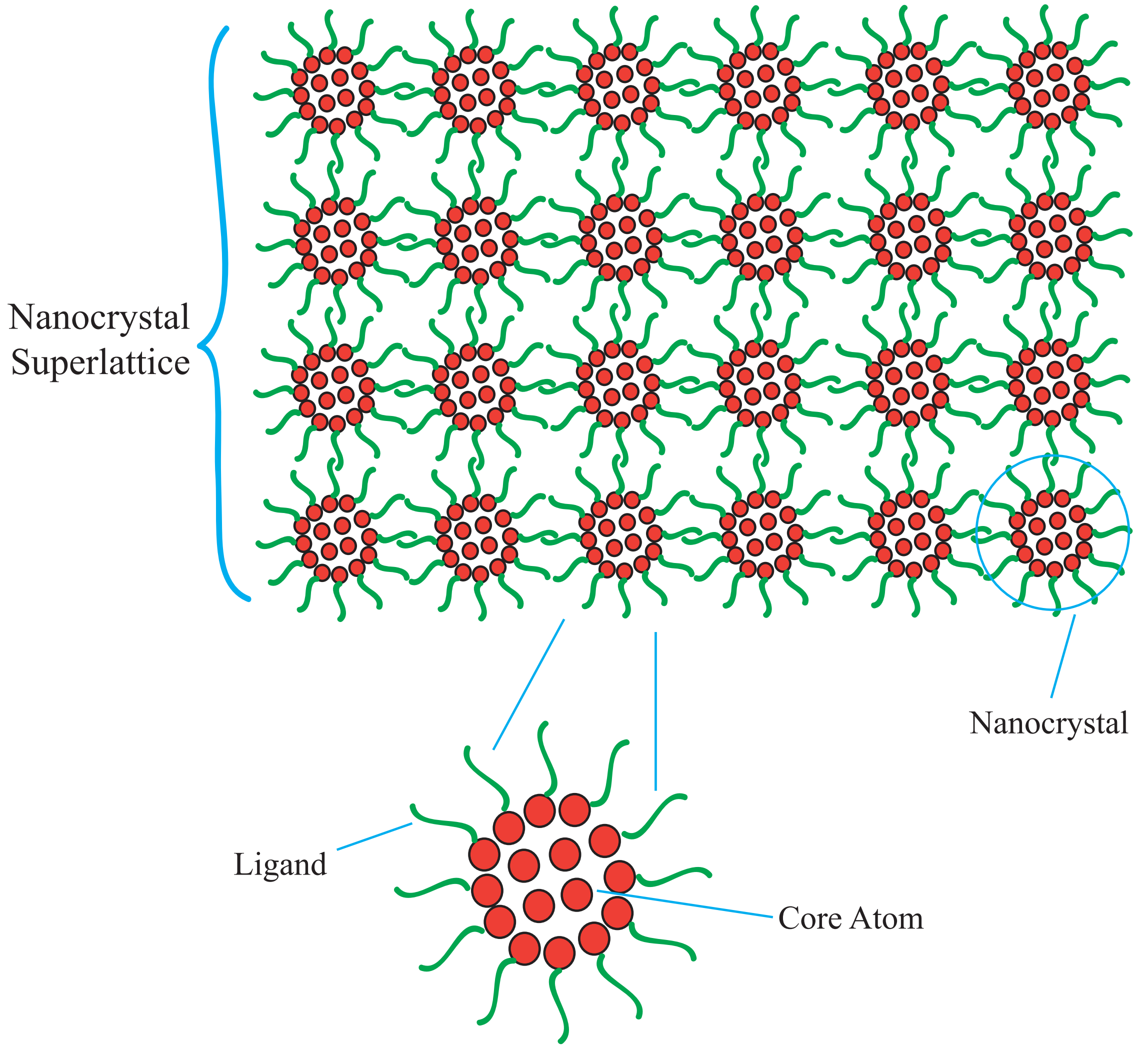

Figure 1.1: A typical nanocrystal superlattice structure

interesting and potentially immediate application for nanocrystals is in the area of thermoelectric materials [22, 23] to convert temperature differences to electric voltage and vice-versa. The performance of a thermoelectric material is determined by the thermoelectric figure of merit [24]

$$ZT = \frac{S^2 \sigma T}{k} \tag{1.2.1}$$

where S is the Seebeck coefficient, σ is the electrical conductivity, T is the temperature, and k is the thermal conductivity. In order to obtain better thermoelectric materials, one strategy is to use nanostructures that reduce thermal conductivity without adversely affecting the electrical conductivity. The ability to increase the electron mobility in thin film nanocrystal superlattices which increases the electrical conductivity makes them suitable candidates for thermoelectric applications [8]. Additionally, nanocrystal superlattices provide new directions in designing phononic interdimensional materials where the variations of matter density and sound velocity provides opportunities for introducing phononic analogs of photonic behaviors such as waveguiding and bandgaps.

1.3 Project Overview

The goal of this dissertation is to develop models at different length scales to help predict many interesting properties of nanocrystal superlattices. Computer models provide an effective and flexible tool for discovery and optimization of new materials through computational materials by design. As an alternative to conventional methods, computational approaches can significantly reduce the development time and lead to materials of higher performance and cheaper innovative products. With computer resources also becoming less expensive, numerical models, more than ever, provide an invaluable tool to investigate and design new materials with better functionality. Predictive computer models are therefore a useful tool for understanding the mechanisms and the physics behind different phenomena involving NCSLs. With the limited previous efforts invested in studying thermal and phononic properties of NCSLs [12, 13, 25], this work will focus on understanding theoretical aspects of phonon transport in NCSLs using computational models. Chapter 2 discusses models at different scales that are useful for understanding the behavior of nanocrystals. First principles calculations based on ab-initio models are introduced corresponding to the smallest length scales present in these structures. Atomistic models are the next level where individual or groups of atoms are considered as the building blocks of the system with the atomic interactions described based on empirical or ab-initio based force fields. The fully coarse grained and continuum models are described next, where neglecting faster degrees of freedom helps us study systems with much larger number of atoms. In chapter 3, mechanical and thermal properties of nanocrystal superlattices are studied using these different modeling techniques. Chapter 4 focuses on phononic properties of nanocrystal superlattices. Nanocrystals of different shapes and superlattices with different structures are shown to provide interesting phononic properties for applications such as waveguiding and bandgaps that involve manipulating phonons. Finally, in chapter 5 the concept of one-way phonon transport is discussed. Motivated by optical equivalents, the design of a one-way phonon isolator and its implementation in systems such as acoustic waveguides and graphene nanoribbons is presented.

Chapter 2

Computational Models of NCSLs at Different Scales

2.1 Overview

As discussed in Chapter 1, in order to study the behavior of NCSLs, we need to pay attention to various phenomena at different length/time scales. If the internal structure of nanocrystal building blocks is being considered, atomic scale or ab-initio models are required to study individual atoms. Moving to larger scales, the superlattice can also be considered as an assembly of coarse grained particles that represent individual nanocrystals. NCSLs can also be studied by considering continuum level approximation for the superlattice film. In this chapter, we discuss models for NCSLs at different scales. First principles based and atomistic demonstration of these materials are introduced first. Next, coarse grained models are explained. Finally, continuum models that can be used to study different properties of the superlattices are discussed.

2.2 First Principles Based Models

Ab-initio methods have been established and used frequently to study systems with small number of atoms [26]. Such methods calculate material properties from first principles by solving quantum-mechanical Schrödinger or Dirac equations numerically. Ab-initio methods are capable of producing information on electronic, structural, mechanical, and thermal behavior of different materials[26]. They can also predict different properties accurately without the need to any input or empirical data fitting. These methods are nonetheless computationally expensive and can only be used for small number of atoms, i.e. for applications where the desirable behavior can be approximated with a small sized unit cell.

One of the efficient methods to solve the required quantum mechanical equations is density functional theory (DFT). DFT has evolved into a practical method to study properties of many-electron systems from the original work of Hohenberg and Kohn [27]. The theoretical basis of their work is based on two fundamental theorems[27]: first, for any system of interacting particles in an external potential, the potential is determined uniquely, except for a constant, by the ground state particle density. Second, a universal functional for the energy expressed in terms of particle density can be defined which is valid for any external potential. The global minimum value of this functional is the exact ground state energy of the system and the corresponding particle density is the exact ground state density.

In the Kohn-Sham [28] formulation of DFT, the total energy of an electronic system is given by

$$E[n] = \sum_{\alpha} \epsilon_\alpha - \frac{1}{2}\int \frac{n(r)n(r')}{|r-r'|} dr dr' + E_{xc}[n] - \int \frac{\delta E_{xc}}{\delta n(r)} n(r) dr \tag{2.2.1}$$

where $n(r)$ is the electron density, E_{xc} is the exchange and correlation energy [29], ϵ_α are the eigenvalues of the Kohn-Sham equation, $H|\psi_\alpha\rangle = \epsilon_\alpha|\psi_\alpha\rangle$. The self consistent Hamiltonian in an external field v_{ext}, is given by

$$H = -\frac{1}{2}\nabla^2 + v_{ext} + \frac{1}{2}\int \frac{n(r)n(r')}{|r-r'|} dr dr' + E_{xc}[n] \tag{2.2.2}$$

The ground state density of the system is $n(r) = \sum_{\alpha} \psi^*_\alpha(r)\psi_\alpha(r)$.

Later on, in order to improve the efficiency of DFT calculations and to find more effective ways to calculate the first-order and second-order corrections to the wavefunction and energy respectively, Baroni et al. introduced the use of perturbation theory in DFT [30]. In this work, we use the Density-Functional Perturbation Theory (DFPT) framework as implemented in the Quantum-ESPRESSO package [31] to calculate interatomic force constants, the second order derivatives of energy with respect to atomic displacements, which are then directly used to calculating phonon dispersion relations. This involves performing self-consistent electronic structure calculations followed by the calculation of the dynamical matrix on a grid of **k**-vectors [31].

2.3 Atomistic Models

Atomistic models typically use empirical or ab-initio based force fields together with statistical mechanics to determine thermodynamics and transport properties [32]. Such methods can be used to understand the microscopic structure of more complex systems with up to millions of atoms. They also facilitate the study of dynamical processes on longer timescales up to microseconds. The results are however dependent on the quality of the force fields used to represent the systems.

Molecular dynamics (MD) is a popular technique used in atomistic simulations [32]. In MD simulations, the forces between the particles are obtained from interatomic potentials and then equations of motion based on Newton's second law are solved numerically to determine the positions and velocities of the particles at different times by assuming appropriate initial positions and velocities for the particles inside the simulation box. The timesteps suitable for the numerical integration in such simulations are typically around few femto seconds for typical solids.

More specifically, the governing equations are written in the form of Newton's second law of motion,

$$\mathbf{F}_i = m_i \frac{d^2\mathbf{r}_i}{dt^2} \tag{2.3.1}$$

Where m_i is the mass of particle i, $\mathbf{r}_i$ is the particle position, and $\mathbf{F}_i$ is the total force acting on the particle. The assumption of conservative radial forces between the particles, leads us to a potential function and a simplified equation

$$\mathbf{F}_i = -\frac{du}{d\mathbf{r}_i} \tag{2.3.2}$$

where u is the potential energy function. A popular choice for the interaction energy is the Lenard-Jones potential function, also referred to as the L-J potential, or the 6-12 potential. This is a mathematically simple model that describes the interaction between a pair of neutral atoms or molecules as

$$u(r) = 4\epsilon\{(\frac{\sigma}{r})^{12} - (\frac{\sigma}{r})^{6}\} \tag{2.3.3}$$

Using this equation we can compute the corresponding forces,

$$\mathbf{F}(r) = 48\frac{\epsilon}{\sigma}\{(\frac{\sigma}{r})^{13} - 0.5(\frac{\sigma}{r})^{7}\} \tag{2.3.4}$$

where ϵ is the depth of the potential well, σ is the (finite) distance at which the inter-particle potential is zero, and r is the distance between the particles.

After calculating the forces using the specific potential energy, we should integrate the equations of motion in order to find the trajectory and velocity of different particles. There are many different numerical techniques available to perform this integration. one standard method is the *Verlet* algorithm [32] where the calculations are based on position and acceleration at time t ($\mathbf{r}(t)$ and $\mathbf{a}(t)$) and the position at time $t + dt$ ($\mathbf{r}(t + dt)$). Modifying this method, using the *leap frog* scheme, will result in a better method, with lower round-off errors, called the *velocity Verlet* method. This algorithm takes the form

$$\mathbf{r}_i(t + dt) = \mathbf{r}_i(t) + dt\mathbf{v}_i(t) + \frac{1}{2}dt^2\mathbf{a}_i(t) \tag{2.3.5}$$

$$\mathbf{v}_i(t + dt) = \mathbf{v}_i(t) + \frac{1}{2}dt[\mathbf{a}_i(t) + \mathbf{a}_i(t + dt)] \tag{2.3.6}$$

The algorithm involves two stages. First, using the previous equation, we calculate the new positions and the velocities at mid step

$$\mathbf{v}_i(t + \frac{1}{2}dt) = \mathbf{v}_i(t) + \frac{1}{2}dt\mathbf{a}_i(t) \tag{2.3.7}$$

Then the accelerations(forces) at time $t + dt$ are calculated based on the new positions

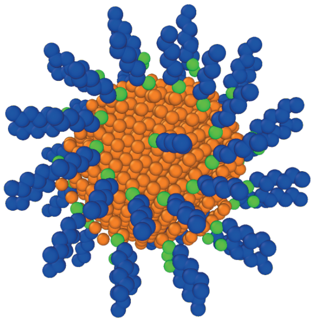

Figure 2.1: Atomistic model of a functionalized nanocrystal

and then the velocities at time $t + dt$ are computed by means of

$$\mathbf{v}_i(t + dt) = \mathbf{v}_i(t + \frac{1}{2}dt) + \frac{1}{2}dt\mathbf{a}_i(t + dt) \tag{2.3.8}$$

At this point the correct velocity (also the correct kinetic energy or temperature) at time $t + dt$ is in hand. By using similar techniques we can numerically solve the equations of motion for a system of atoms and calculate different properties of the system accordingly.

For studying the behavior of nanocrystal superlattices, such models will include the individual core and ligand atoms as separate units. An example atomistic model for a spherical nanoparticle covered with ligands is shown in Figure 2.1.

2.4 Coarse Grained Models

In coarse grained models, groups of atoms are considered as one entity and therefore the number of degrees of freedom are reduced. In other words, coarse grained models provide simplified versions of atomistic models by removing the faster degrees of freedom. Such models can be used to study systems with up to a billion atoms for timescales up to a few seconds. The most important and challenging aspect of coarse grained models is finding

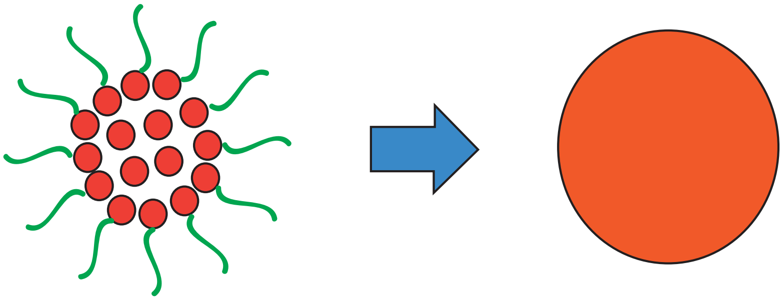

Figure 2.2: Coarse graining a nanocrystal

effective interaction potentials that describe the forces between the groups of atoms that form the coarse grained particles.

For modeling nanocrystal superlattices, different levels of coarse graining may be implemented. The core atoms could be considered as solid units while ligand atoms are considered individually [33]. Ligand atoms themselves can also be coarse grained in different manners [34]. However, all these partial coarse grained models will still require some level of atomic detail and can be computationally expensive. On the other hand, fully coarse grained models of NCSLs consider each nanocrystal as one individual unit as shown in Figure 2.2. Such models are computationally much cheaper and prove to be useful if the interactions between nanoparticles are described accurately.

2.5 Continuum Models

Continuum models assume that matter is continuous and treat the properties of the system as field quantities. We can then numerically solve balance equations coupled with phenomenological equations to predict the properties of the system. Such methods can in principle handle systems of any size and dynamic processes on long time scales. However,

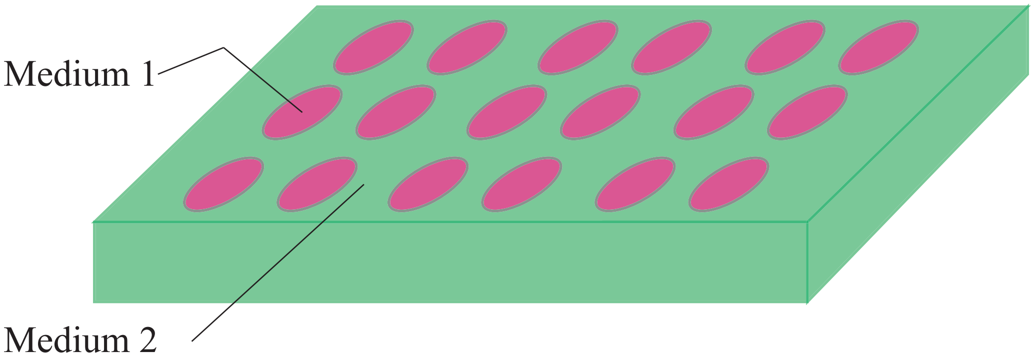

Figure 2.3: Representation of NCSLs with continuum models where medium 1 and medium 2 respresent the core and ligands respectively.

they require inputs from experiments or from lower scale methods and cannot explain phenomena that depend on electronic, atomic or molecular levels of detail.

In dealing with NCSLs, as sketched in Figure 2.3, one can approximate the superlattice domain as the combination of two different types of material representing the core and the surrounding ligands. By using appropriate properties for the different domains and solving the continuum equations either analytically or numerically, problems such as acoustic or electromagnetic wave propagation in such materials can be studied.

2.6 Summary

In summary, different modeling techniques can be used to study NCSLs, from ab-initio models all the way up to continuum models. Such models have different accuracy in predicting the properties of NCSLs as well as their different computational costs. Because of the complicated nature of NCSLs, it is very important to understand when each of these modeling techniques can be used. In the following chapters, therefore, we determine and use the most appropriate modeling technique based on the specific property being studied. We also discuss the conditions under which the use of each specific modeling technique is reasonable.

Chapter 3

Mechanical and Thermal Properties of Nanocrystal Superlattices

3.1 Overview

Computational models at different scales provide a useful tool to study different properties of nanocrystal superlattices. In this chapter, mechanical and thermal properties of NCSLs are studied. First, we study mechanical properties by calculating elastic moduli of NCSLs using atomistic and coarse grained models. The elastic moduli incorporate properties of low frequency acoustic phonons which are important in thermal transport. Evaluation of the accuracy of different computational models in predicting mechanical properties of NCSLs will provide valuable insight in using suitable models for calculating thermal properties. Thermal conductivity of NCSLs is then studied using appropriate atomistic and first principles based computational models.

3.2 Mechanical Property Calculations

3.2.1 Introduction

While many studies have focused on the structural properties of NCSLs, limited studies have been performed to determine their mechanical properties. A few groups probed such properties experimentally. Podsiadlo et al. reported elastic moduli for different kinds of 2D and 3D NCSLs [35]. Yin et al. used nanoindentation to measure elastic moduli of a monolayer of colloidal hollow silica nanoparticles [36]. Tam et al. reported elastic properties of PbS nanocrytals [37]. Marquardt et al. measured elastic properties of MgO nanocrystals at high pressures [38]. Computer simulations provide another route to obtain mechanical properties of NCSLs [39] with the advantage that a wide variety of nanocrystal sizes, shapes and capping ligands can be explored to identify NCSL with desired mechanical properties. A key ingredient of such simulations is the model used to represent the interactions between the NCSLs. In the only theoretical study of NCSL mechanical properties to date, Landman and Luedtke [39] used molecular dynamics simulations [32] to calculate elastic moduli of gold NCSLs by considering an atomistic model for the ligands and a single rigid core of gold. The disadvantage of using fully atomistic methods for modeling NCSLs is that it is computationally very expensive to model these systems directly. For example, a superlattice of 108 nanocrystals of 4nm diameter CdSe capped with hexylthiol contains more than 100,000 atoms. For these reasons, most previous theoretical studies of NCSLs have been based on simpler coarse grained models in the form of an effective potential energy for the nanocrystal-nanocrystal interaction [10, 3, 40, 41]. Such a model neglects the internal details of the nanocrystals but enables treatment of a larger number of nanocrystals.

The use of modeling to calculate physical properties of NCSL systems is still in its early stages. Modeling can provide a valuable complement to experimental methods for predicting bulk and local properties of NCSLs, provided that the models are validated against known material properties. In this section, we investigate the accuracy of previously proposed atomistic and coarse grained models for CdSe nanocrystals by comparing properties calculated from these models for CdSe NCSLs to those measured experimentally. Specifically Young's and bulk moduli are computed. We also investigate the dependence of NCSL elastic properties on size: both the size of nanocrystal and the size of the entire NCSL array. Finally, we use continuum effective medium theory to study the size dependence of the moduli and compare the observed trends to those predicted from the atomistic model.

3.2.2 Atomistic Model

Model details and computation of mechanical properties

Molecular dynamics simulations are performed to calculate elastic moduli of CdSe NCSLs structures as a function of CdSe core size. CdSe nanocrystals functionalized with organic capping ligands are the building blocks of the superlattice [42, 43]. The interactions between the core atoms (Cd and Se) are best described by a combination of Lennard-

Jones and Coulomb forces developed by Rabani [44]

$$U_{ij}(r_{ij}) = U_{LJ} + U_{Coulomb} \tag{3.2.1}$$

where

$$U_{LJ} = 4\epsilon \left[(\frac{\sigma}{r_{ij}})^{12} - (\frac{\sigma}{r_{ij}})^{6} \right] \tag{3.2.2}$$

and

$$U_{Coulomb} = C\frac{q_i q_j}{r_{ij}} \tag{3.2.3}$$

where r_{ij} is the distance between atoms i and j, q_i and q_j are the charges on atoms i and j, C is a constant depending on the units used and σ and ϵ are Lennard-Jones potential parameters [32]. The LJ parameters for Cd and Se are obtained from Reference [44] . A cut off radius of $10\mathring{A}$ was used for the LJ potential.

In this study, we consider nanocrystals with hexylthiol (C_6SH) capping ligands. For ligand molecules, CH_2 and CH_3 groups are considered as pseudoatoms and treated as one point particles in MD simulations [45, 43]. Also, hydrogen atoms in the SH group are modeled as point charges. These point particles interact via intermolecular and intramolecular forces. Intermolecular interactions are modeled as the sum of LJ and Coulomb terms. LJ cross terms are obtained from arithmetic and geometric averages for σ and ϵ, respectively [43]. The partial charges for different (pseudo)atoms are listed in the literature [42, 43]. Within the ligand molecules, the atoms interact via bond stretch, bond angle and torsional forces. The appropriate expressions and parameters for these intramolecular forces are described in the TraPPE [45] force field. Additionally, atoms that are separated by more than three bonds interact via intermolecular Coulomb and LJ interactions [45].

In a molecular dynamics simulation the elastic properties of the system can be studied by applying appropriate strains to the system and calculating the resulting stresses. The Young's modulus (E) of a nanocrystal superlattice describes the slope of the stress-strain curve in the linear regime. We calculated the Young's modulus by applying a uniaxial strain (ϵ_{xx}) to the superlattice and calculating the resulting axial stress (T_{xx}) [46, 47]. The stress tensor at the atomic level is calculated by [47]

$$\mathbf{T} = -\frac{1}{V}\left[\sum_{\text{atom}\, i} m_i \mathbf{v}_i \otimes \mathbf{v}_i + \frac{1}{2}\sum_{\text{atom}\, i}\sum_{\text{atom}\, j\neq i} \mathbf{F}_{ij} \otimes \mathbf{r}_{ij}\right] \tag{3.2.4}$$

where $\mathbf{T}$ is the stress tensor, V is the volume of the system and $\mathbf{r}$, $\mathbf{v}$ and $\mathbf{F}$ are the position, velocity and force vectors. To calculate the stress-strain curve, we applied a small strain in the x direction and then let the system relax while keeping the stress in y and z directions fixed at zero. The resulting axial stress T_{xx} was then calculated. We also calculated the bulk modulus (B). Bulk modulus $B = -\frac{\Delta p}{\Delta V/V}$ is calculated by applying gradually increasing strain uniformly in x,y, and z directions and calculating the resulting pressure p which is equal to the negative diagonal elements of the stress tensor.

Initialization of individual nanocrystals and nanocrystal superlattices

CdSe nanocrystals were prepared by cutting out a sphere with a given radius from a bulk CdSe wurtzite lattice [42, 43]. We then imported these initial structures into LAMMPS [48] and let the structure relax using a steepest descent minimization algorithm. Next, we created single capping ligand molecules of C_6SH. To do so, we used Chimera [49] to obtain an initial configuration of the atoms for each ligand molecule and then optimized the geometry by performing energy minimization. The ligand molecules were then added to the core one by one and energy minimization was performed each time to relax the system [42]. Passivated nanocrystals were then used to create superlattices by placing

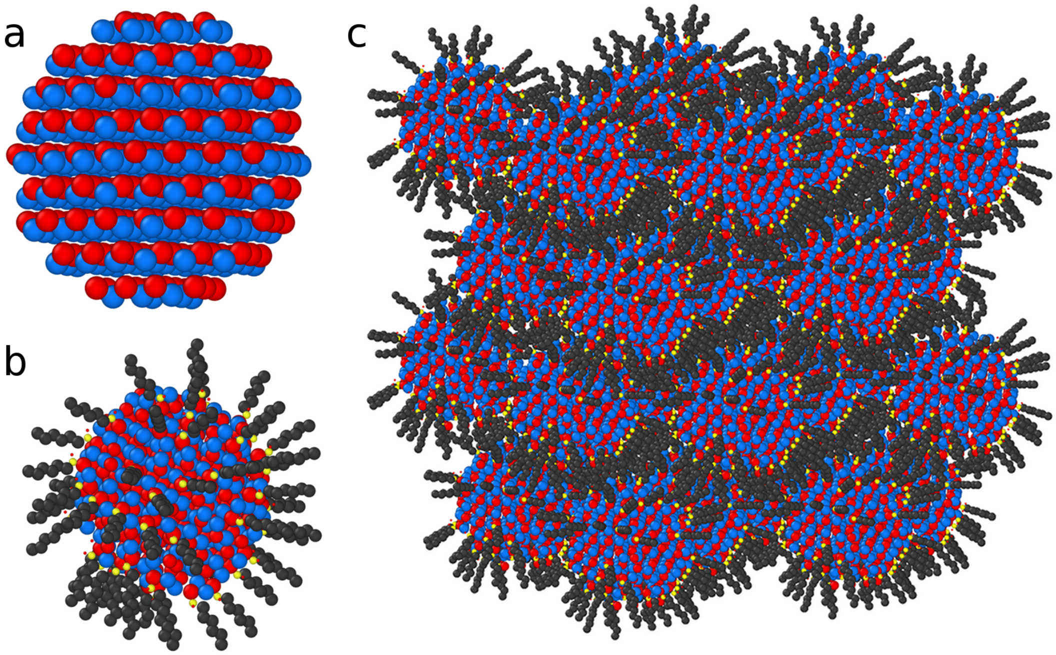

Figure 3.1: Superlattice structure of CdSe nanocrystals. (a) CdSe core. (b) CdSe nanocrystal with hexylthiol ligands. (c) FCC nanocrystal superlattice structure.

them at the positions of the desired superlattice unit cell. Here we placed passivated CdSe nanocrystals at positions of a face-centered cubic structure (Figure 3.1). The lattice constant chosen initially is large enough so that there is no interaction between different cores. Next, constant pressure simulations of the superlattice system are performed by applying a gradually decreasing external pressure to allow the nanocrystals to form a close packed structure [39]. Periodic boundary conditions were used in these simulations. Finally the system is equilibrated at zero pressure. The temperature is kept constant (300 K) using the Nose-Hoover thermostat [32]. A time step of 2 fs is used in the simulation and the equilibration takes about 5ns. After this final equilibration the superlattice system is ready for further studies to calculate elastic properties.

3.2.3 Coarse Grained Model

In the coarse grained model of NCSLs each nanocrystal plus the capping ligands is considered as a single spherical unit interacting with other nanocrystals (Figure 2.2). The pairwise interaction energy for nanocrystals in a superlattice has been described previously as summation of repulsive, van der Waals and electrostatic interactions [10, 6].

$$U(r) = U_{vdW}(r) + U_{electrostatic}(r) + U_{repulsive}(r) \tag{3.2.5}$$

where r is the center to center distance of the nanocrystals.

The van der Waals forces are attractive forces between nanocrystals described by [50]

$$\begin{aligned} U_{vdW}(r) = -\frac{A}{6}[&\frac{2a_1a_2}{r^2-(a_1+a_2)^2} + \frac{2a_1a_2}{r^2-(a_1-a_2)^2} \\ &+\ln\left(\frac{r^2-(a_1+a_2)^2}{r^2-(a_1-a_2)^2}\right)] \end{aligned} \tag{3.2.6}$$

A is the Hamaker constant and a_1 and a_2 are the radii of the two nanocrystals. The electrostatic forces arise from the interaction between charges and permanent and induced dipoles [51]

$$U_{charge-charge} = \frac{q_1q_2}{4\pi\epsilon_0\epsilon_r\, r} \tag{3.2.7}$$

$$U_{charge-dipole} = \frac{1}{4\pi\epsilon_0\epsilon_r r^2}(\mathbf{p}_1\cdot\hat{\mathbf{r}}q_2 - \mathbf{p}_2\cdot\hat{\mathbf{r}}q_1) \tag{3.2.8}$$

$$U_{charge-induceddipole} = -\frac{q_1^2\alpha_2 + q_2^2\alpha_1}{2(4\pi\epsilon_0\epsilon_r)^2r^4} \tag{3.2.9}$$

$$U_{dipole-dipole} = \frac{1}{4\pi\epsilon_0\epsilon_r r^3}[\mathbf{p}_1\cdot\mathbf{p}_2 - 3(\mathbf{p}_1\cdot\hat{\mathbf{r}})(\mathbf{p}_2\cdot\hat{\mathbf{r}})] \tag{3.2.10}$$

$$U_{dipole-induceddipole} = \frac{-[p_2^2\alpha_1(1+3(\hat{\mathbf{p}_2}\cdot\hat{\mathbf{r}})^2) + p_1^2\alpha_2(1+3(\hat{\mathbf{p}_1}\cdot\hat{\mathbf{r}})^2)]}{2(4\pi\epsilon_0\epsilon_r)^2r^6} \tag{3.2.11}$$

Here $\mathbf{r}$ is the vector connecting nanocrystals 1 and 2, q_1 and q_2 are the net charges, $\mathbf{p}_1$ and $\mathbf{p}_2$ are the dipole moments, and α_1 and α_2 are the dipole polarizabilities of nanocrystals 1 and 2. The short range repulsive forces between nanocrystals are usually estimated by the equation proposed by de Gennes [52, 53]

$$U_R^{steric} = \frac{100S\delta^2}{(r-2S)\pi\sigma_l^2} kT \exp\left(-\frac{\pi(r-2S)}{\delta}\right) \tag{3.2.12}$$

where $S = \frac{2a_1a_2}{a_1+a_2}$ is a factor related to the nanoparticle radii, δ is the apparent thickness of the ligand shell around the nanocrystal core, and σ_l is the diameter of the area occupied by the ligand on the particle surface.

The coarse grained nanocrystals were set up in an FCC lattice. The Hamaker constant A, the dipole moments and the electronic polarizability of CdSe nanocrystals are obtained from previously reported data [54, 10, 42]. $\epsilon_r \simeq 2$ was used based on reported values in the literature [10]. Here the charge-charge and charge-(induced)dipole terms vanish because the nanocrystals do not carry a net charge. In order to avoid dealing with quantities that are too big or too small, we scaled all of the parameters according to Table 3.1 using the Hamaker constant (A) as the energy unit, the diameter of the nanocrystals (d) as the length unit, and the mass of the nanocrystal (m) as the mass unit. Since we only have one type of nanocrystal in each superlattice, $a_1 = a_2 = \frac{d}{2}$ or $a_1^* = a_2^* = \frac{1}{2}$ in the nondimensional form for the U_{vdW} term.

To calculate Young's and bulk moduli of CdSe NCSL from the coarse grained model, a simple approach based on the deformation of the NCSL can be used. Applying varying amounts of deformation to the NCSL leads to a quadratic variation of energy. The curvature of the energy-strain curve yields the elastic moduli [46].

Table 3.1: Dimensionless Quantities

Quantity	Dimensionless Form
Length	$L^* = L/d$
Energy	$U^* = U/A$
Force	$F^* = Fd/A$
Stress	$S^*_{ij} = S_{ij}d^3/A$
Time	$t^* = \frac{t}{d}\sqrt{\frac{A}{m}}$
Charge	$q^* = \frac{q}{\sqrt{4\pi\epsilon_0 dA}}$
Polarizability	$\alpha^* = \frac{\alpha}{4\pi\epsilon_0 d^3}$
Electric Dipole	$p^* = \frac{p}{\sqrt{4\pi\epsilon_0 d^3 A}}$

3.2.4 Results

Figure 3.2 shows the values of Young's and bulk moduli calculated from atomistic models. As simulation box size is known to affect MD results when the box is too small, we investigate this effect on Young's and bulk moduli for cubic arrays of NCSL with 32, 108, and 256 nanocrystals (Figure 3.3) that have equal box size in all dimensions. There is negligible dependence on NCSL array size, with a maximum error of less than 4% observed for the 32 nanocrystal case as compared to 256 nanocrystal case. As the 108 nanocrystal results are substantially the same as those for 256 nanocrystals with much smaller computational cost, all reported results here are for the array size of 108.

Young's and bulk moduli were also calculated from coarse grained models for different sizes of nanocrystals and the results are shown in Figure 3.4.

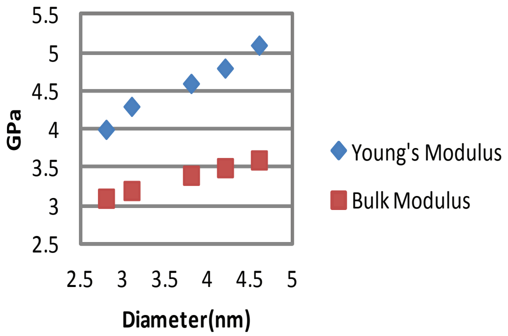

Figure 3.2: Young's and bulk moduli of CdSe NCSLs with different core sizes calculated from atomistic models

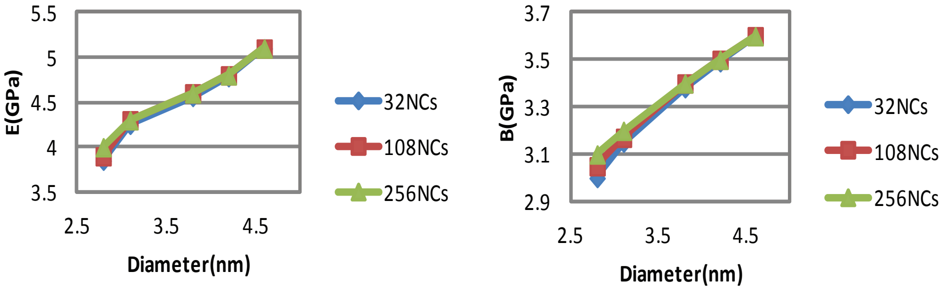

Figure 3.3: Young's (left) and bulk (right) moduli calculated from atomistic models for NCSL arrays of different sizes

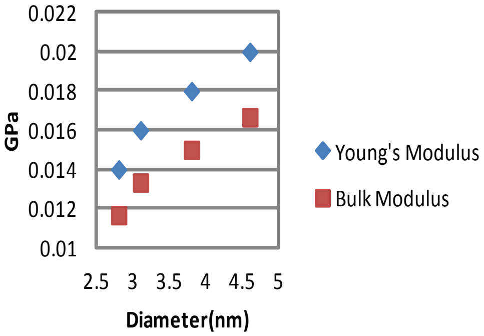

Figure 3.4: Young's and bulk moduli of CdSe NCSLs calculated from coarse grained model

3.2.5 Discussion

The elastic moduli calculated using the atomistic model ranged from 3 to 5 GPa for CdSe core sizes between 2.5 and 5 nm. These values agree well with experimental measurements on nanocrystal assemblies [35, 36, 37] and with previous calculations of elastic properties of gold nanocrytals [39]. Podsiadlo et al. reported elastic moduli of a few GPa for 4.6 nm CdSe NCSLs[35]. Yin et al. reported values between 2 and 8 GPa for elastic moduli of a monolayer of colloidal hollow silica nanoparticles [36] . Tam et al. reported a Young's modulus of 1.7GPa for PbS nanocrytals [37]. Landman and Luedtke [39] reported elastic moduli values between 1 to 8 GPa for gold NCSLs.

Notably, the Young's and bulk moduli both demonstrate a clear increase with CdSe core size. A similar size dependence has been observed by Podsiadlo et al. [35]. To understand such a trend, we compare these results to those computed using effective medium theory [55]. Effective medium theory is a macroscopic approach used to estimate the effective elastic moduli of a composite system in terms of the properties and volume fractions of its constituents. Considering the NCSL as a combination of core and ligand atoms, we calculated upper and lower bound estimates of Young's and bulk moduli from the Voigt-Reuss effective medium model (Figure 3.5). The Voigt-Reuss model is a simple model that gives wide upper and lower bounds for possible values of elastic moduli. The upper bound (Voigt) is found by assuming that the strain is everywhere uniform and the lower bound (Reuss) is found by assuming that the stress is everywhere uniform

$$M_{Voigt} = \sum f_i M_i \tag{3.2.13}$$

$$M_{Reuss}^{-1} = \sum \frac{f_i}{M_i} \tag{3.2.14}$$

Here f_i and M_i are the volume fraction and modulus of constituent i. For CdSe NCSLs the two constituents of the system are the CdSe core and the hexylthiol ligands. We used average values of 50 GPa and 49 GPa for Young's and bulk moduli of bulk CdSe [44]. Young's and bulk moduli of the ligands constituents are not reported in the literature, so we estimate them as 3 GPa and 2.9 GPa respectively, from the elastic properties of bulk polymer chains [56]. It is evident that the effective medium model overpredicts elastic moduli, with the upper and lower bounds both exceeding the MD-calculated values. More accurate models such as that by Hashin and Shtrikman [57] or those incorporating geometrical information [58, 59, 60] yield narrower bounds within those of Voigt-Reuss.

The differences between effective medium and MD predictions indicate that atomistic features neglected in the effective medium models, such as the dependence of the moduli of individual nanocrystals on size and the details of the interface, may play an important role in determining the moduli of NCSL. In general the elastic moduli of nanostructures can either increase or decrease when the size of the nanostructures is reduced[61, 62, 63].

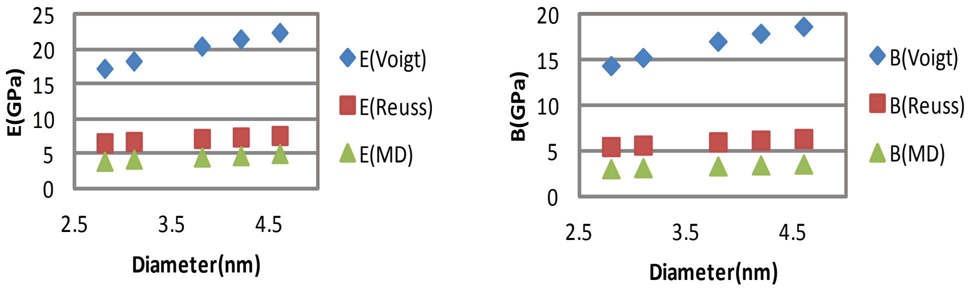

Figure 3.5: Effective medium theory prediction of elastic moduli of CdSe NCSLs.

No clear evidence of size dependence on individual nanocrystal moduli is found in the present results for aggregate NCSL moduli, as the NCSL moduli increase with core size. However, the core volume fraction also increases with core size, so it is possible that reduction of individual nanocrystal moduli is occurring but that this effect is more than compensated by the increased volume fraction of higher-modulus (relative to the ligands) nanocrystals. A more likely reason for the differences between effective medium and MD model predictions is that the details of the ligand-nanocrystal interface are important for determining the elastic properties of NCSLs. This is consistent with recent findings about thermal properties of NCSLs, which indicate that the interface, rather than the core is dominant [12].

Coarse grained calculations of elastic moduli, similarly to atomistic calculations, show a clear increase with core size. The increase is slightly more pronounced: it is roughly 30% for an increase of core size in the range 2.5 - 5 nm for compared to about 14-20% calculated with the atomistic model. However, the absolute values, for example E = 0.02 GPa and B = 0.01GPa for 4.6nm core sizes, are two orders of magnitude lower than both our atomistic results and previously reported results from other groups. This indicates that the typical coarse grained models used in studying structural characteristics of nanocrystals[6, 10] are not effective in predicting elastic properties of NCSLs. One reason for this may be that higher order electrostatic interaction terms such as quadrupole moments, which become increasingly important at small nanocrystal spacing, are neglected in such models. Another reason may be that the ligand-ligand and ligand-core interactions are incorrectly represented in the coarse grained models, which assume only repulsive interactions and neglect attractions between ligands that could significantly increase the cohesion between nanocrystals and thus increase the moduli of the NCSL. One of the main advantages of coarse grained models is the rather simple form of interactions, but finding pair potentials that appropriately represent higher order electrostatics and ligand-ligand interactions is difficult [64]. Thus, for accurate computations of NCSL elastic properties, it is necessary at this time to use computationally expensive atomistic models rather than simpler coarse grained models.

3.3 Thermal Conductivity Calculations

3.3.1 Introduction

Thermal management is an important task in realizing practical applications of NCSLs in areas such as electronics and optics [14, 15, 16] since high operating temperatures could degrade device performance and lifetime. Thermal conductivity describes the ability of a material to dissipate heat; for this reason, understanding and predicting thermal conductivity of NCSLs is an integral part of understanding their practical applications.

Additionally, for evaluating NCSLs as high performance thermoelectrics [22, 24], thermal conductivity calculations are required. Computer simulations offer significant promise for predicting thermal properties because they enable rapid exploration of a wide parameter space of nanocrystal sizes, shapes, materials, and capping ligands. Regarding thermal conductivity calculations, quantum dot superlattices have been previously studied theoretically and experimentally [65, 66, 67]. Ong et al. [12] reported the first experimental and theoretical studies of the thermal conductivity of NCSL, using frequency-domain thermoreflectance measurements and nonequilibrium method thermal conductivity calculations on one-dimensional chains of nanocrystals. While their thermal conductivity model predicted results qualitatively similar to the experimental results, no quantitative predictions for 3D bulk NCSL thermal conductivity can be made from such a model due to its simplified 1D nature. Hence there is a need to develop more realistic models that capture the full 3D geometrical configuration of the NCSL.

Here two different types of NCSLs are studied for thermal conductivity calculations. First, we study thermal conductivity of NCSLs that are fully covered with ligands which are in general important thermal materials but due to the low electron mobility are not particularly appropriate for thermoelectic applications. Since we showed that the coarse grained models underpredict NCSL elastic moduli, it is expected that atomistic rather than coarse grained models will be required to calculate accurate phononic and thermal properties. A key ingredient of such simulations is the model used to represent the interactions between the nanocrystals, which needs to describe core-core, ligand-ligand, and core-ligand atomic interactions [42, 68]. Using suitable interaction potentials, atomistic simulations can be very helpful in predicting different properties of nanocrystal superlattices. Here, we use three dimensional fully atomistic models to calculate thermal conductivity of nanocrystal superlattices. We use molecular dynamics (MD) simulations with the Green-Kubo method to calculate thermal conductivity of spherical NCSLs of different size and surface ligand density. Next, we consider NCSLs with different shapes and compositions and compare empirical potential and first principles based predictions of thermal conductivity. The second category of NCSLs that are considered in thermal conductivity calculations are those with higher electron mobility [8] which are suitable for thermoelectrics. We use a parallel thermal resistance model and compare empirical potential calculations with first principles based models for predicting thermal conductivity of octahedral lead selenide NCSLs.

3.3.2 Thermal Conductivity Calculation Using Equilibrium Molecular Dynamics

Details of Atomistic model

In this study we consider gold nanocrystals with hexylthiol (C_6SH) capping ligands. First, a single nanocrystal is constructed. The gold core of this nanocrystal is built by cutting a spherical domain out of face-centered cubic gold crystal. The ligand chains are added by placing them close to the surface of the core. The pair potential functions for the interactions between different core and ligand atoms in a nanocrystal were obtained from Ref. [68]. For the ligand chains, bond stretch (U_s), bond bending (U_θ), and torsion (U_τ) interactions are considered as the following terms

$$U_s = \frac{1}{2}k_s(r - r_o)^2 \tag{3.3.1}$$

$$U_\theta = \frac{1}{2}k_\theta(\theta - \theta_o)^2 \tag{3.3.2}$$

$$U_\tau = \sum_{i=0}^{5} a_i \cos^i(\phi) \tag{3.3.3}$$

where r is the bond length, θ is the bending angle, and ϕ is the dihedral angle. For the nonbonded interactions, a combination of Lennard-Jones (U_{LJ}) potential with the Lorentz-Berthelot mixing rule used [32] and Morse (U_M) potential is used.

$$U_{LJ} = 4\epsilon\left[(\frac{\sigma}{r_{ij}})^{12} - (\frac{\sigma}{r_{ij}})^{6}\right] \tag{3.3.4}$$

$$U_M = De[(1 - \exp(-a(r_{ij} - r_{mo})))^2 - 1] \tag{3.3.5}$$

The constant parameters used for different bonded and nonbonded interaction potentials are listed in Table 3.2.

The structure of the nanocrystal is relaxed for 1 ns at 300 K using MD simulations in LAMMPS [48] with a time step of 5 fs. The final relaxed structure is shown in Fig 3.6 (a). Each nanocrystal consists of 688 Au atoms and is passivated by 72 hexylthiol capping ligand chains.

The thermal conductivity, k, is determined using the Green-Kubo approach, which predicts k for an isotropic material by relating the dissipation of thermal fluctuations in an equilibrium system to its thermal conductivity [69, 70]

$$k = \frac{1}{3k_b V T^2}\int_0^\infty \langle \mathbf{J}(t) \cdot \mathbf{J}(0)\rangle \, dt \tag{3.3.6}$$

Table 3.2: Potential function parameters used in MD simulation of gold NCSLs

Quantity	value
k_s (for both S-C and C-C bonds)	14.00 eV/$\AA^2$
r_o (S-C bond)	1.815 Å
r_o (C-C bond)	1.523 Å
k_θ (for both S-C-C and C-C-C angles)	5.388 eV/rad^2
θ_o (S-C-C angle)	114.4
θ_o (C-C-C angle)	109.5
Torsion parameter a_0	0.09617 eV
Torsion parameter a_1	0.125988 eV
Torsion parameter a_2	-0.13598 eV
Torsion parameter a_3	-0.0317 eV
Torsion parameter a_4	0.27196 eV
Torsion parameter a_5	-0.32642 eV
$\epsilon_{LJ}/\sigma_{LJ}$: C-C	0.00513 eV / 3.914 Å
$\epsilon_{LJ}/\sigma_{LJ}$: S-S	0.01724 eV / 4.250 Å
$\epsilon_{LJ}/\sigma_{LJ}$: Au-Au	0.001691 eV / 2.934 Å
De: Au-Au	0.475 eV
De: Au-S	0.380 eV
a/r_{mo}: Au-Au	1.583 $\AA^{-1}$ / 3.0242 Å
a/r_{mo}: Au-S	1.470 $\AA^{-1}$/ 2.650 Å

where k_b is the Boltzmann constant, $\mathbf{J}$ is the heat current, V is the volume of the simulation cell, T is temperature, t is time, and $\langle \mathbf{J}(t) \cdot \mathbf{J}(0) \rangle$ is the heat current autocorrelation function(HCACF). To calculate thermal conductivity using this method, we first construct the superlattice. This is done using the procedure of Landman and Luedtke [39], in which a single relaxed nanocrystal (Fig. 3.6 (a)) is replicated in a face-centered cubic lattice. The superlattice structure is equilibrated using the NPT ensemble in MD for 5 ns at 300 K to form the final structure shown in Fig. 3.6 (b).

Large oscillations in the heat current autocorrelation function are observed as a result of the relative motion of bonded atoms and the high frequency of such oscillations is indicative of optical phonons [71, 72, 73]. The time integral of the HCACF converges to yield the value of thermal conductivity k (Eq. 3.3.6). Eight independent simulations using different initial velocities for atoms inside the system were performed for a $3 \times 3 \times 3$ superlattice in order to get a good sampling of the phase space. The HCACFs were integrated up to 6 ns resulting in an average value of $k = 0.25$W/m-K with a standard error of 0.03W/m-K. This value falls within the 0.1-0.4 W/m-K range experimentally measured for various types of NCSLs [12]. It is also close to the thermal conductivity of the passivating hexylthiol ligands, which is reported to be around 0.15 W/m-K. [74] More specifically a value of $k \simeq 0.18$ W/m-K with an error bar of about 0.04 W/m-K was reported for gold nanocrystal with n-dodecanethiol ligands which are almost two times longer than the ligands used in our simulations. The slightly lower reported values compared to our results is expected since longer passivating ligands will further increase the dominance of the thermally insulating components and, therefore, result in NCSLs with lower thermal conductivity. Reported values of quantum dot superlattice thermal

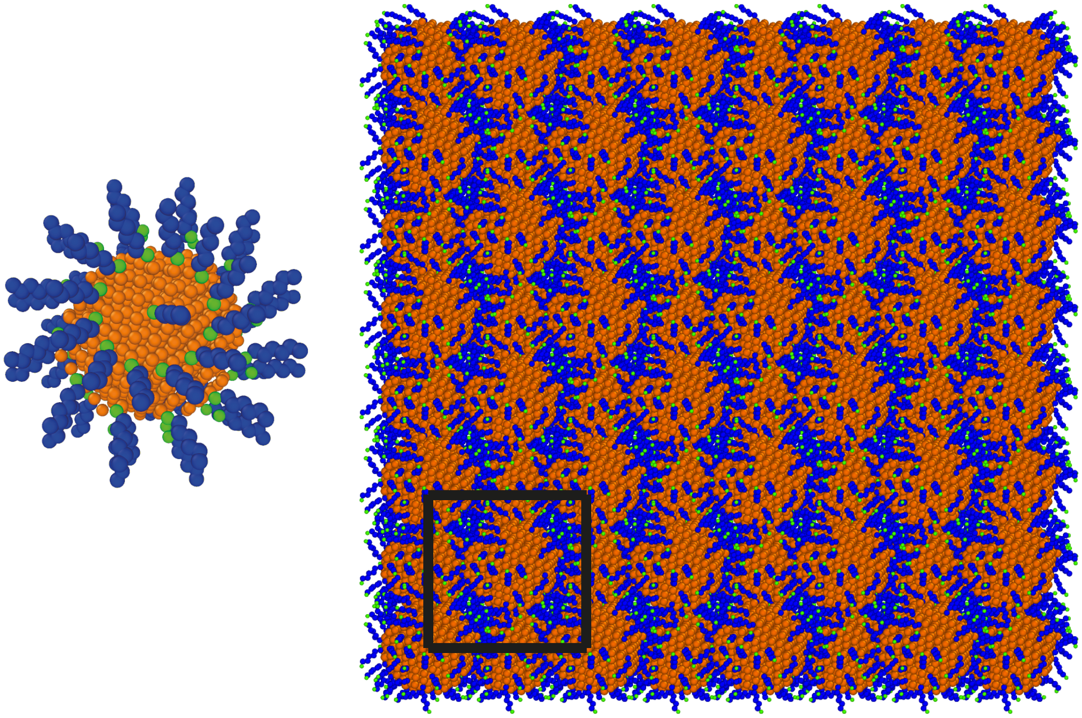
(a) (b)

Figure 3.6: (a) Single 2.8 nm gold nanocrystal capped with 72 hexylthiol ligands. Orange particles are the core gold atoms, blue particles represent CH_2 and CH_3 groups, and green particles are the sulfur atoms of the capping ligands. (b) A 4 × 4 × 4 face-centered cubic configuration of 2.8nm diameter gold nanocrystals with hexylthiol ligands used in MD simulations. The black box shows the top view of a conventional unit cell of the FCC superlattice.

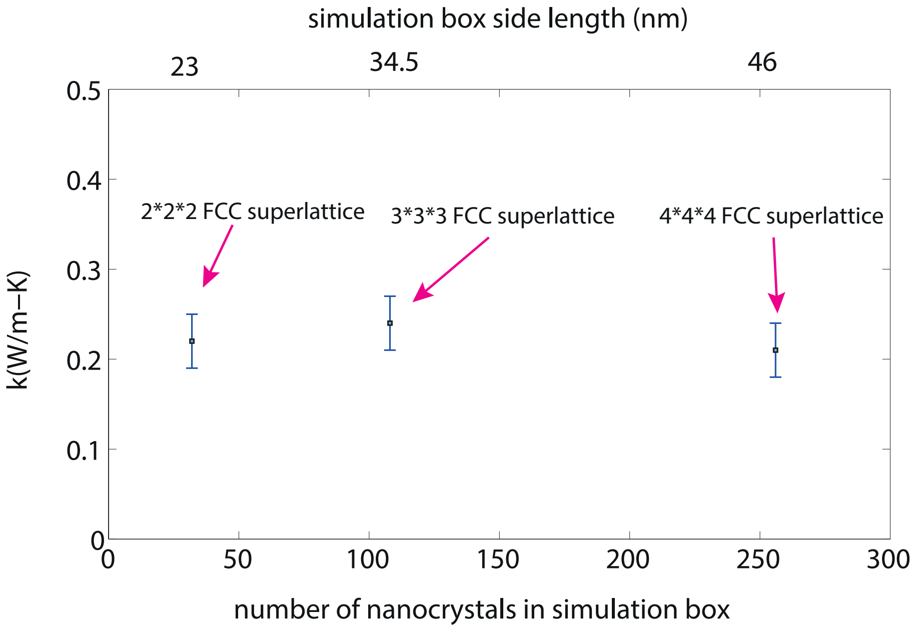

Figure 3.7: Dependence of thermal conductivity on the simulation box size for 2.8nm gold nanocrystal superlattice.

conductivities [65], on the other hand, are orders of magnitude higher (8-12 W/m-K) which is due to the absence of passivating organic ligands.

We also investigated the dependence of thermal conductivity on the simulation box size for sizes ranging from $2 \times 2 \times 2$ to $4 \times 4 \times 4$ FCC unit cells. Finite size effects can artificially reduce the computed values of thermal conductivity by disallowing phonons with wavelengths larger than the simulation box size [75, 76]. A simulation is considered converged at and above the size when the computed thermal conductivity shows no size dependence. As shown in Fig. 3.7, even the smallest $2 \times 2 \times 2$ box sizes are converged. Within error, there is no dependence of thermal conductivity on box size. This result is compatible with previous studies of elastic properties of nanocrystal superlattices [77, 39] which also show no box size dependence.

Effect of core size and surface coverage on thermal conductivity

We followed the same steps discussed earlier to calculate thermal conductivity of NCSLs with the same number (72) of capping ligands per each nanocrystal but different core sizes (equivalently, different number of gold atoms in the core). The results are presented in Fig. 3.8 (a). MD simulations show an increase in thermal conductivity with increasing core size. This result was also expected intuitively, due to the larger volume fraction of high thermal conductivity core particles compared to the ligands.

Also, as shown in Fig. 3.8 (b), increasing surface ligand density of the nanocrystals results in a decrease in thermal conductivity. Two potential explanations for this trend are as follows. First, the side length of the FCC unit cell increases from 23 to 27 nm as the ligand surface coverage increases from 50 to 80 %. The increase in spacing between thermally conductive cores is expected to reduce the effective thermal transport in the NCSLs. Second, at lower surface ligand densities, the ligands tend to arrange as individual chains in between core atoms. Isolated ligand chains are expected to exhibit larger thermal conductivities than bulk-like entangled ligands [78].

Another interesting observation is related to the contribution of free electrons to the thermal conductivity of NCSLs. Using the approximate value of 0.027 $\Omega^{-1}cm^{-1}$ taken from the measured electrical conductivity of thiol-capped gold nanoparticle films at 300 K [79], we estimate from the Wiedemann-Franz law a value of 2×10^{-5} W/m-k for the electronic contribution of the thermal conductivity. This value is negligible compared to the phononic contributions obtained from MD calculations, which shows the applicability of MD simulations for NCSL thermal conductivity predictions.

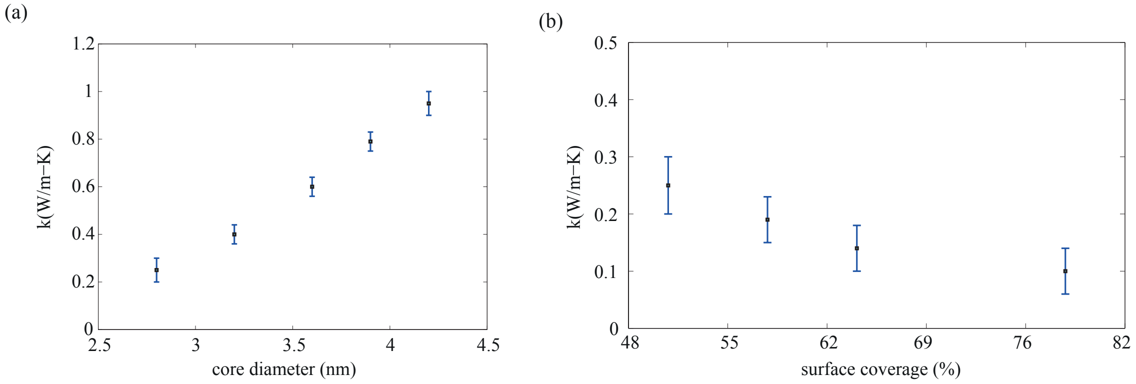

Figure 3.8: (a) Thermal conductivity dependence on the core size with 72 capping ligands covering the surface. (b) Thermal conductivity dependence on surface coverage for 2.8nm gold nanocrystals.

3.3.3 Thermal Conductivity of Lead Selenide NCSLs

As mentioned earlier, in order to develop materials with better thermoelectric performance, one of the major parameters that needs to be increased is the electrical conductivity or electron mobility. If the nanocrystals are fully covered with ligands, as was the case in the previous sections, the electron mobility is very small and thus ZT will be small. Recently, lead chalcogenide nanocrystals have been synthesized that show higher electrical mobility and are therefore promising for thermoelectric applications [8]. Here we use computational models to calculate thermal conductivity of these nanocrystals which is another important parameter in determining their thermoelectric performance.

We consider a lead selenide (PbSe) nanocrystal superlattice formed from 5.9 nm nanocrystals with truncated octahedron shape assembled in a close-packed simple cubic structure (Figure 3.9). Typical MD methods using empirical pair potentials have been proposed to study structural properties of PbSe nanocrystals [80]. However, the ac-

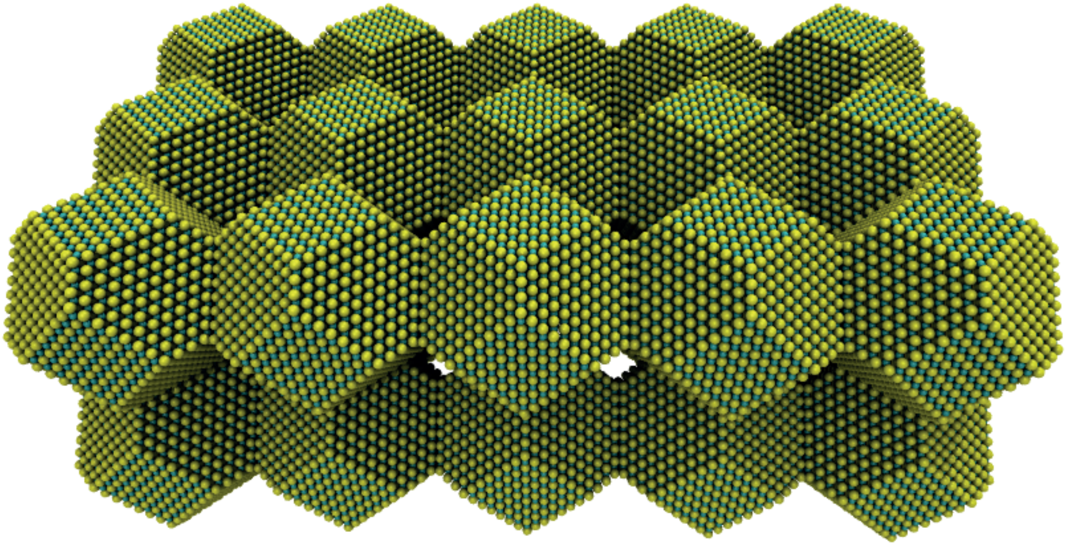

Figure 3.9: Simple cubic PbSe nanocrystal superlattice.

curacy of such empirical potentials in predicting thermal properties should be examined. Additionally, the relaxed structure of the nanocrystals in an acceptable MD simulations should resemble its specific shape; however, for nonspherical shapes, the empirical potentials may not necessarily recreate the specific shape of the nanocrystal. For these reasons, typical MD methods are not used in the following section, rather the accuracy of empirical potential in predicting thermal conductivity of PbSe NCSLs are examined using a simplified parallel resistance model.

Thermal Conductivity: Parallel Resistance Model

In order to calculate the thermal conductivity of PbSe NCSLs we adopt a parallel resistance model. The superlattice is formed from a close-packed bed of nanocrystals with air in between them. There are three main contributions to the total thermal resistance of the NCSL, as shown in Figure 3.10. The first contribution comes from the constriction resistance, which is denoted by R_{nc}. Another contribution comes from the combined air-solid interface resistance and air resistance denoted by R_{air}, and the final contribution is due to radiation resistance denoted by R_{rad}. In Fig. 3.10, $l_{uc} = 6.2\text{nm}$ is the unit cell length. We define $A_{uc} = 34.3\text{nm}^2$ as the unit cell area, and $A_{air} = 27.5\text{nm}^2$ is the unit cell area minus the contact area of the nanocrystals. Typically, in order to increase electron mobility in these NCSLs, the concentration of ligands are decreased significantly to the point that there are hardly any ligands present in between the nanocrystals [8]. For this reason we neglect the effect of ligands. We also neglect surface disorders that might exist and contribute to diffuse thermal transport and consider a primarily ballistic thermal transport. The total thermal resistance, R_{tot}, is then calculated from these contributions

$$\frac{1}{R_{total}} = \frac{1}{R_{nc}} + \frac{1}{R_{air}} + \frac{1}{R_{rad}} \tag{3.3.7}$$

The air and radiation resistances can be approximated based on material properties and temperature [81, 82]. For the air-solid interface (R_1 in Fig. 3.10 (c)) , expressed in terms of conductance per unit area G_1, we have [82]

$$\frac{1}{G_1} = 2[(2-\beta)/\beta][2/(\psi+1)][1/(\mu C_\nu)]l_{air} \tag{3.3.8}$$

where β is the accommodation coefficient, l_{air} is the mean free path of air molecules, ψ is the ratio of specific heats, μ is the viscosity of air, and C_ν is the specific heat of air at constant volume. β for air [82] is typically around 0.9, μ is $1.98 \times 10^{-5}\text{Pa}\cdot\text{s}$, $\psi = 1.4$, $C_\nu = 0.718\text{KJ/Kg K}$, $l_{air} = 68nm$ at room temperature [83]. The air resistance (R_2 in Fig. 3.10 (c)) can be approximated based on the thermal conductivity of air, $G_2 = \frac{k_{air} l_{uc}}{A_{air}}$ where $k_{air} = 0.05\text{W/m}-\text{K}$. This equation yields a value of $G_{air} \approx 1.12\times10^7\text{W/m}^2-\text{K}$ for the conductance corresponding to air-solid interfaces and the air in between nanocrystals.

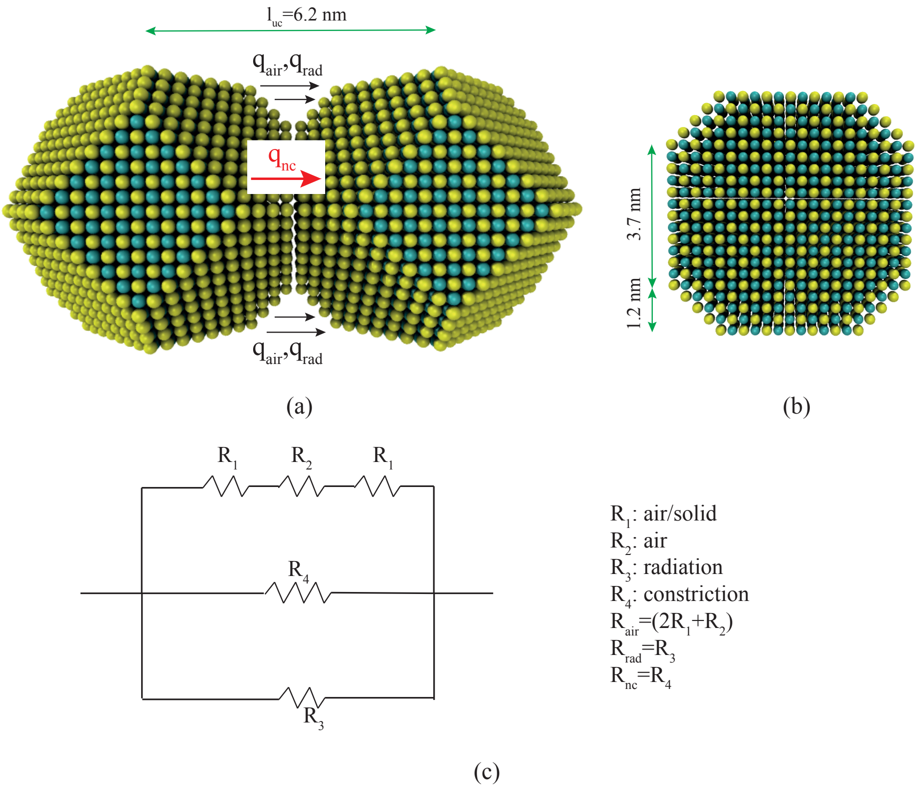

Figure 3.10: (a) Top view of a unit cell of simple cubic PbSe NCSL. (b) Cross section of the unit cell. (c) Representation of the parallel thermal resistance model.

The radiation effect can be approximated based on the near-field thermal radiation theory [84]. Due to closeness of the nanocrystals in the superlattice structure, the wavelength of the photons can be comparable to the gap size between the nanocrystals, making the near-field effects important. The radiation conductance can be defined based on [85]

$$G_{rad} = \lim_{T_A \to T_B} \frac{q''(T_A, T_B)}{T_A - T_B}$$

where $q''(T_A, T_B)$ is the radiative heat flux between two surfaces at temperatures T_A and T_B. It is possible to derive an expression for this radiative heat conductance between two nanocrystals separated by a very small gap from the well known results of radiative heat transfer between semi-infinite objects [85, 86]. Based on the approximation for the maximum near-field heat flux between two semi-infinite media [84, 87], the radiation conductance for nanocrystals at temperature T is given by $G_{rad} = \frac{k_b^2 \beta_c^2}{24\hbar} T$. Here we have $\beta_c = \frac{\pi}{a_{uc}}$ where a_{uc} is the periodicity of the superlattice. Consequently, $G_{rad} \approx 2 \times 10^4 T$ $[\mathrm{W/m^2-K}]$. The contribution of radiation will therefore be around $10^7 \mathrm{W/m^2-K}$ for typical temperatures.

R_{nc} can be calculated from phonon transport properties at the nanocrystal constriction [88]

$$\frac{1}{R_{nc}} = \frac{1}{2}[\sum \int \int \frac{\partial f_{BE}}{\partial T} \hbar\omega D_\omega v_\omega \tau(\omega, \theta) \sin\theta d\theta d\omega] A \tag{3.3.9}$$

Here $f_{BE} = \frac{1}{\exp(\hbar\omega/k_b T) - 1}$ is the Bose-Einstein distribution, ω is the phonon frequency, D_ω and v_ω are phonon density of states and phonon group velocity, θ is the phonon incidence angle, and τ is the transmissivity of phonons. In general, one method to calculate τ is to solve the acoustic wave equations through the constriction assuming stress free boundary conditions. When the constriction diameter, denoted by a, is much bigger than the dominant wavelength of the thermal phonons, λ_D, τ can be approximated [81] as the ratio of the projected area of the constriction in the direction of the incident wave and the area of the constriction, i.e. as $\cos\theta$. λ_D can be approximated from $2\pi\hbar v/\lambda_D = k_b T$, where v is the phonon group velocity. Phonon group velocities for bulk PbSe [89] are below 4000 m/s. This results in $\lambda_D < 1.3$ nm for temperatures above 150 K, while here $a \simeq 3$nm. Thus, $\tau = \cos\theta$ is a reasonable assumption. The only missing information for calculating R_{nc} is the phonon density of states and group velocities for which we need to calculate the phonon dispersion curves. The group velocity $v_\omega = \frac{\partial\omega}{\partial k}$ is calculated from the slope of the dispersion curve and density of states is calculated from $D_\omega = \frac{k^2}{2\pi^2}\frac{1}{v_\omega}$. For the size of nanocrystals here, we can approximate the phonon dispersion curve with the bulk dispersion relation of PbSe. To calculate the phonon dispersion we use the lattice dynamics method as described in the following section.

Phonon Dispersion Curve Calculation Using Lattice Dynamics

In the harmonic lattice dynamics theory, after establishing the equilibrium position of atoms in a unit cell, the displacement from equilibrium of any atom in the unit cell is expressed as a summation over all normal modes of vibration of the atoms [90]:

$$\mathbf{u}(lj,t) = \sum_{k,\nu} A_{k,\nu}\mathbf{U}(j,k,\nu)\exp\left(i\left(\mathbf{k}\cdot\mathbf{r}\begin{pmatrix} j \\ l \end{pmatrix} - \omega t\right)\right) \tag{3.3.10}$$

Here j is the index of an atom in a unit cell and l is the index of each unit cell. $A_{k,\nu}$ is the mode amplitude, $\mathbf{r}$ is the equilibrium position of the atom in the unit cell, $\mathbf{k}$ represents the wavevector, and ν denotes a mode type. $\mathbf{U}(j,k,\nu)$ is the polarization vector of atom j in the unit cell 0 associated with the normal mode (k,ν). The displacement of any atom

j in any unit cell l is determined by $A_{k,\nu}\mathbf{U}(j,k,\nu)$ multiplied by an exponential factor. In the standard lattice dynamics method, Eq. 3.3.10 is substituted into Newton's second law resulting in

$$m_j \ddot{\mathbf{u}}(jl,t) = -\sum_{j'l'} \Phi \begin{pmatrix} jj' \\ \\ ll' \end{pmatrix} \mathbf{u}(j'l',t) \tag{3.3.11}$$

Here j' runs through all the atoms in the unit cell and l' runs through all the unit cells. m_j is the mass of atom j and Φ is the interatomic force constant matrix. This matrix is a $3n \times 3n$ matrix with n being the number of atoms per unit cell. Φ is comprised of n 3×3 submatrices:

$$\Phi_{\alpha\alpha'}(jl,j'l') = \frac{\partial^2 W}{\partial r_\alpha \begin{pmatrix} j \\ \\ 0 \end{pmatrix} \partial r_{\alpha'} \begin{pmatrix} j' \\ \\ l' \end{pmatrix}} \tag{3.3.12}$$

α and α' are the Cartesian components x, y, and z and W is the total lattice potential energy. Using the vector

$$\mathbf{e}(k,\nu) = m_j^{1/2}[U_x(1,k,\nu)U_y(1,k,\nu)U_z(1,k,\nu)....U_z(n,k,\nu)]^T \tag{3.3.13}$$

Eq. 3.3.11 simplifies to the following eigenvalue problem:

$$\omega^2(k,\nu)\mathbf{e}(k,\nu) = \mathbf{D}(k)\mathbf{e}(k,\nu) \tag{3.3.14}$$

where the dynamical matrix, **D**, is defined as

$$D_{3(j-1)+\alpha,3(j'-1)+\alpha'}(\mathbf{k}) = \frac{1}{\sqrt{m_j m_{j'}}} \sum_{l'} \frac{\partial^2 W}{\partial r_\alpha \begin{pmatrix} j \\ 0 \end{pmatrix} \partial r_{\alpha'} \begin{pmatrix} j' \\ l' \end{pmatrix}} |_o \exp(i\mathbf{k} \cdot [\mathbf{r} \begin{pmatrix} j' \\ l' \end{pmatrix} - \mathbf{r} \begin{pmatrix} j \\ 0 \end{pmatrix}]) \tag{3.3.15}$$

The phonon dispersion relation, the relationship between **k** and ω, is calculated from the eigenvalues of **D** as the wavenumber is changed. In calculating the dynamical matrix, the interatomic force constants are an integral part which depend on the interatomic potential functions. We compare two different approaches to calculate the interatomic force constants: The first approach is based on empirical pair potentials used to describe the interaction between Pb and Se atoms. The second method is based on the more computationally involved and more accurate first principles calculations.

Phonon Dispersion Results

The empirical potential is based on a combination of Lennard-Jones and Coulomb potentials

$$U_{LJ} = 4\epsilon \left[(\frac{\sigma}{r_{ij}})^{12} - (\frac{\sigma}{r_{ij}})^6 \right] \tag{3.3.16}$$

$$U_{Coulomb} = C\frac{q_i q_j}{r_{ij}} \tag{3.3.17}$$

The parameters for this potential are listed in Table 3.3. The cross terms are obtained from the Lorentz-Berthelot mixing rule. The resulting phonon dispersion curve based on the empirical potentials is shown in Figure 3.11.

The first principles calculations were performed in the framework of density functional perturbation theory (DFPT) using the Quantum ESPRESSO package [31]. In the ground

Table 3.3: Empirical Potential Parameters

Parameter	Pb	Se
q [e]	1.29	-1.29
σ_{LJ} [nm]	0.329	0.436
ϵ_{LJ}/k_b [K]	30.0	45.3

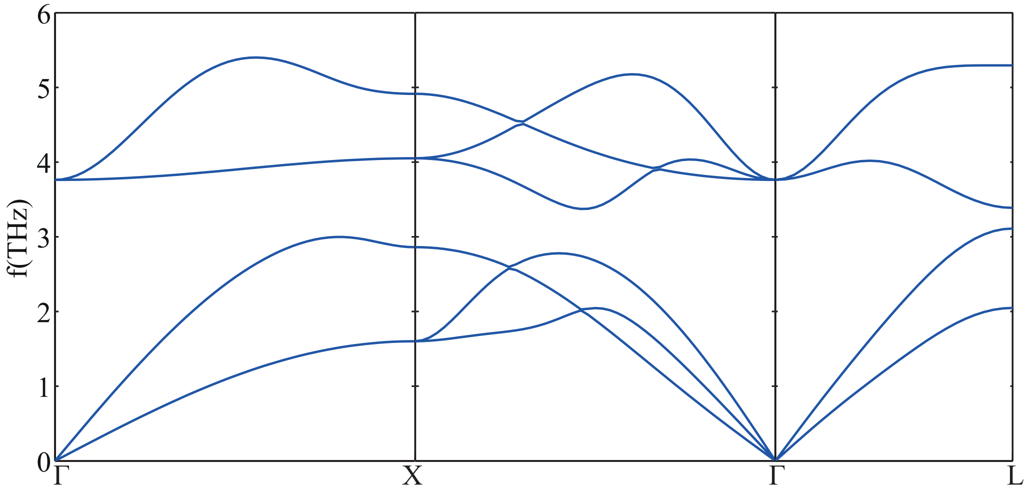

Figure 3.11: Phonon dispersion relation of bulk PbSe in the main symmetry directions of the first Brillouin zone based on the empirical potentials.

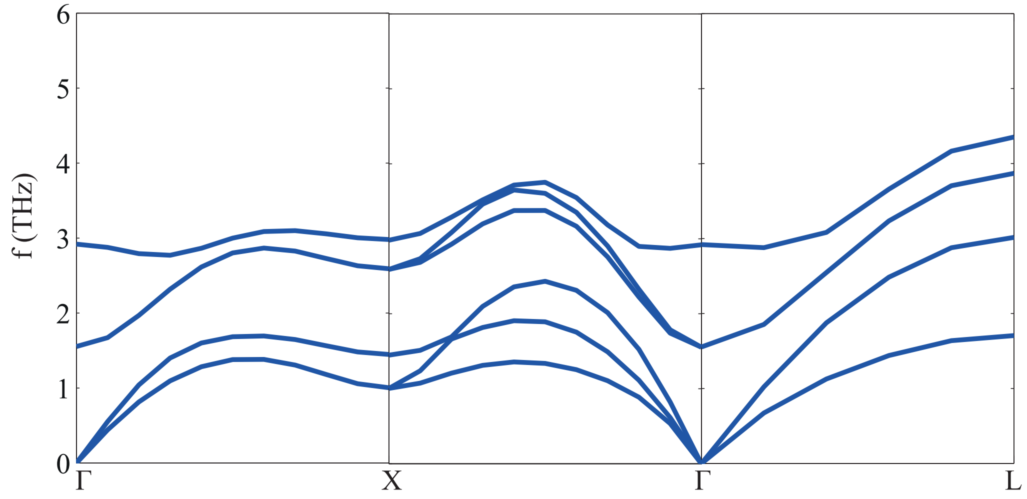

Figure 3.12: Phonon dispersion relation of bulk PbSe in the main symmetry directions of the first Brillouin zone based on first principles calculations.

state calculations, we used relativistic pseudopotentials Pb.rel-pz-dn-kjpaw_ psl.1.0.0.UPF and Se.rel-pz-dn-kjpaw_ psl.1.0.0.UPF from the PSlibrary of QEforge distribution. The resulting phonon dispersion curve is shown in Figure 3.12.

Thermal Conductivity Calculations

Based on the dispersion curve calculations, the constriction resistance can be calculated from Eq. 3.3.9. The resulting constriction conductance is between $2.9 \times 10^8 \mathrm{W/m^2 - K}$ and $3.1 \times 10^8 \mathrm{W/m^2 - K}$ for temperatures between 150 K and 400 K, about 7 times larger than the combined air and radiation conductance. The effective thermal resistance is then given by

$$\frac{1}{R_{total}} = \frac{1}{R_{nc}} + A_{air}G_{air} + A_{air}G_{rad} \tag{3.3.18}$$

and the thermal conductivity is given by $k = \frac{l_{uc}}{R_{tot}A_{uc}}$. The total thermal conductivities calculated from both the empirical potentials and first principles are shown in Figure 3.13.

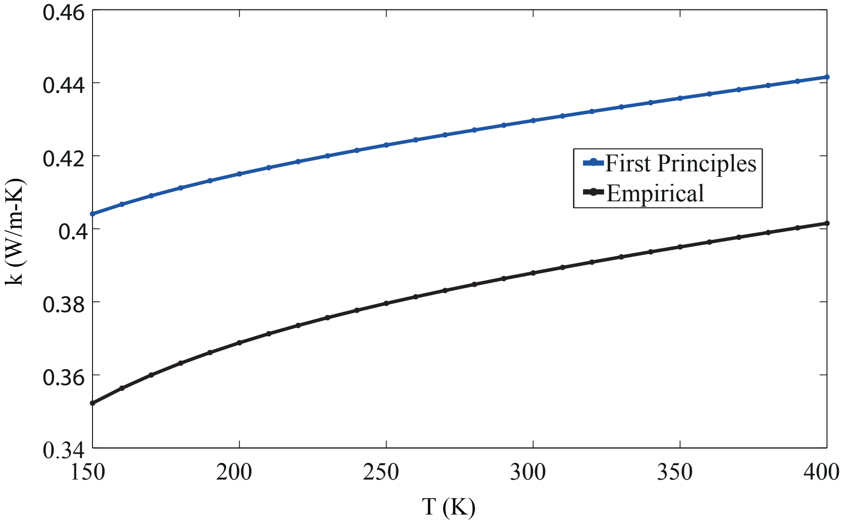

Figure 3.13: Comparison of thermal conductivity of PbSe NCSLs obtained from empirical potentials and first principles.

We observe that first principles calculations predict thermal conductivity values between 0.40W/m-K and 0.44W/m-K for temperatures between 150 K and 400 K, while empirical potentials predict values in the range 0.35 – 0.41W/m-K. Therefore, approximately a 15% difference between the empirical potential and the first principles calculations of thermal conductivity is observed. These predictions are also similar to the available experimental results [12] which reported values between 0.10W/m-K and 0.20W/m-K for 7.5 nm spherical PbSe NCSLs for temperatures between 150 K and 400 K. Additionally, these values for the thermal conductivity are smaller than that of bulk PbSe which agrees with the presence of interface resistances and phonon confinement effects in nanocrystal superlattices compared to the bulk.

3.4 Summary

In this chapter we first studied mechanical properties of NCSLs which also represent low frequency acoustic phonons. The elastic properties of CdSe nanocrystal superlattices were calculated using molecular dynamics, existing coarse grained nanocrystal-nanocrystal interaction models, and effective medium theory. In the molecular dynamics simulations, detailed atomic interactions for CdSe nanocrystals and the capping ligand atoms are considered. In the coarse grained model, the ligand-capped nanocrystal cores are treated as point particles interacting via pair potentials. In the effective medium theory, calculations include only the moduli and volume fractions of CdSe cores and ligands. Although computationally expensive, the atomistic simulations predict elastic properties that agree well with available experimental and theoretical results for similar systems. In contrast, more efficient approaches yield less accurate results. Based on this observation that relates to low frequency phonons and also to take into account the whole phonon spectrum, atomistic models were used to proceed with thermal conductivity calculations. From equilibrium molecular dynamics, the thermal conductivities of spherical nanocrystal superlattices were successfully predicted in reasonable agreement with experimental results. Thermal conductivity of PbSe NCSLs with octahedral shape nanocrystals was also calculated by providing a comparison between empirical potentials and first principles calculations. In addition to providing an alternative to experiments, these models can be useful to investigate the effect of shape, size, and composition on phononic and thermal properties of nanocrystal superlattices.

Chapter 4

Phonic Band Structure of Nanocrystal Superlattices

4.1 Introduction

Phonon engineering, which involves controlling phonon transport via tuning phonon dispersion relation, is increasingly important for basic science and also for many applications that require manipulation of the flow of vibrational energy, i.e. sound and heat [91, 92, 93, 94, 95, 96, 97, 98, 99, 100, 101, 102, 103]. As a primary example, periodic composite materials, also known as phononic crystals, have been shown to exhibit a strong modification of the phononic band structure and introduce complete bandgaps due to the scattering of mechanical waves at the interface between materials with different mechanical properties[104, 105, 106, 107]. Such composite materials have important applications in acoustic filtering [108], waveguiding [109, 110, 111], focusing [112], noise control [113], and vibrational control for mechanical systems [114].

Recent advances in material processing techniques at the micro- and nanoscale have created enormous opportunities for phononics areas such as RF communication technologies and optomechanics [115, 116]. Nanocrystal superlattices (NCSLs) [4, 3, 5, 7], as discussed earlier, are periodically ordered nanoscale materials in which complex interactions between low-dimensional building blocks of the superlattice give rise to many interesting and unusual properties such as their photonic band structure and the introduction of photonic bandgaps [117, 118, 119, 120]. It has been shown that shape and structure of building blocks play an important role in tuning the photonic bandgaps in the context of photonic crystals [121, 122, 123]. Similar phononic effects are also expected in NCSLs. The vibrational dissimilarities of the inorganic core atoms and their capping hydrocarbon ligands introduces the phononic mismatch required to create phononic bandgaps. Additionally, the ability to vary the core size, shape, and material provides possibilities for tuning the phononic band structures. Prior to this work, phonon dispersion studies have been limited to spherical nanocrystals [124] and arrays of embedded orthorhombic quantum dots [25, 125]. However, the effect of nanocrystal shape, size, and structural arrangement on the phononic band structure as well as their applications for tuning phononic bandgaps have not been studied.

In this chapter, we calculate the phononic band structure of a variety of nanocrystal superlattices with different shapes and structures. Among these are included binary nanocrystal superlatties, whose unit cells are constructed from two different types of nanocrystals rather than a single nanocrystal type. We discuss different possibilities for tuning the phononic bandgaps through changing nanocrystal size, shape, core volume fraction, and superlattice structure.

4.2 Methods

Both continuum level [25, 125] and atomistic level [124] methods have been previously used to study phonon dispersion in NCSLs. Atomistic methods are in general computationally expensive and mainly advantageous for studying phonon dispersion in systems with a small number of atoms per unit cell. They also face major limitations with regard to the lack of properly posed pair-potential functions that can describe the particle interactions accurately for different material types and structures. Continuum models on the other hand are applicable to a wide variety of materials with different structures while also being computationally a lot less expensive [100]. It has also been shown that phonon dispersion calculations based on continuum models agree well with atomistic models for frequencies below about 1 THz [126, 127]. In this study we are focused on dispersion branches with low frequencies, where deviations of continuum models from atomistic models are expected to be minimal.

In this study, we use continuum models to calculate phonon dispersion curves with frequencies up to about three hundred GHz for different NCSLs as listed in Table 4.1. This was done by using the finite element method to numerically solve the three dimensional acoustic wave equations

$$-\rho\omega^2\mathbf{u} = \frac{E}{2(1+\nu)}\nabla^2\mathbf{u} + \frac{E}{2(1+\nu)(1-2\nu)}\nabla(\nabla\cdot\mathbf{u}) \tag{4.2.1}$$

where $\mathbf{u}$ is the displacement vector and ω is the frequency. Here E and ν are the Young's modulus and the Poisson's ratio, and ρ is the density of the material. Bloch's periodic boundary conditions are considered in all three Cartesian directions for the boundaries of the unit cells. The unit cells consist of the core domains with properties, $(E_{core}, \nu_{core}, \rho_{core})$, and the surrounding ligand domains with with properties, $(E_{lig}, \nu_{lig}, \rho_{lig})$. For the ligands we use average properties of (3 GPa, 0.4, 1050 Kg/m^3) as the Young's modulus, Poisson's ratio, and the density respectively [56]. For the platinum cubic cores, gold nanocrystals in BNSLs and nanorods, the silver, palladium, and iron oxide nanocrystals in BNSLs, we used bulk properties [56], i.e. (168 GPa, 0.38, 21450 Kg/m^3) for Pt, (79 GPa, 0.44, 19300 Kg/m^3) for Au, (83 GPa, 0.37, 10490 Kg/m^3) for Ag, (121 GPa, 0.39, 12023 Kg/m^3) for Pd, and (180 GPa, 0.3, 5242 Kg/m^3) for Fe_2O_3. For PbSe nanocrystals in BNSLs and octahedral nanocrystals we used bulk properties of (65 GPa, 0.24, 8100 Kg/m^3) [128], and for PbS nanocrystals in AlB_2 BNSLs we used the values (75 GPa, 0.3, 7600 Kg/m^3) [128].

Bandgap width calculations for different core volume fractions, ϕ, were performed by changing the unit cell dimensions while keeping the core dimensions constant. The band structure calculations were then performed for each unit cell separately and the bandgap width was obtained from the phonon dispersion curves. For SC and FCC cubic NCSLs, we used nanocrystals of 5.5 nm and 4.7 nm size respectively [9]. The SC superlattice contains one nanocrystal per unit cell and the FCC superlattice contains four nanocrystals per unit cell.

4.3 Phononic Band Structure of NCSLs

We studied phononic band structure for a variety of NCSLs using the computational framework outlined in the Methods section. In Figure 4.1 (a) shows a typical simple cubic three dimensional superlattice with cubic nanocrystals as the building block, and

Table 4.1: NCSLs studied in phononic band structure calculations

Material	Shape	Superlattice Structure
Pt	Cubic	SC
PbSe	Octahedron	SC
Au	Nanorod	Hexagonal
PbSe and Au	Spherical	CuAu (Binary)
PbSe and Ag	Spherical	Cu_3Au (Binary)
PbSe and Pd	Spherical	CaB_6 (Binary)
$\gamma - Fe_2O_3$ and Au	Spherical	NaCl (Binary)
PbS and Pd	Spherical	AlB_2 (Binary)

Fig. 4.1 (b) shows the corresponding unit cell used in phonon dispersion calculations. The unit cell consists of a platinum cubic core surrounded by octylamine ligands [9]. The calculated phonon dispersion curve in the main symmetry directions is shown in Fig. 4.1 (c) . Complete phononic bandgaps (PBGs) can be observed from the dispersion curve. The largest PBG for the cubic nanocrystal is centered at a frequency about 99 GHz with a width of 81 GHz. A smaller bandgap of 27 GHz width centered around 166 GHz is also observed. The phononic band structure also shows interesting features in different symmetry directions; the first bandgap is largest in the ΓX direction, while the second bandgap is slightly larger in the MH symmetry direction than in other directions.

We calculated the phononic band structure for cubic NCSLs of different core sizes to investigate the effect on bandgap width and central frequency f_C. Ligand length was

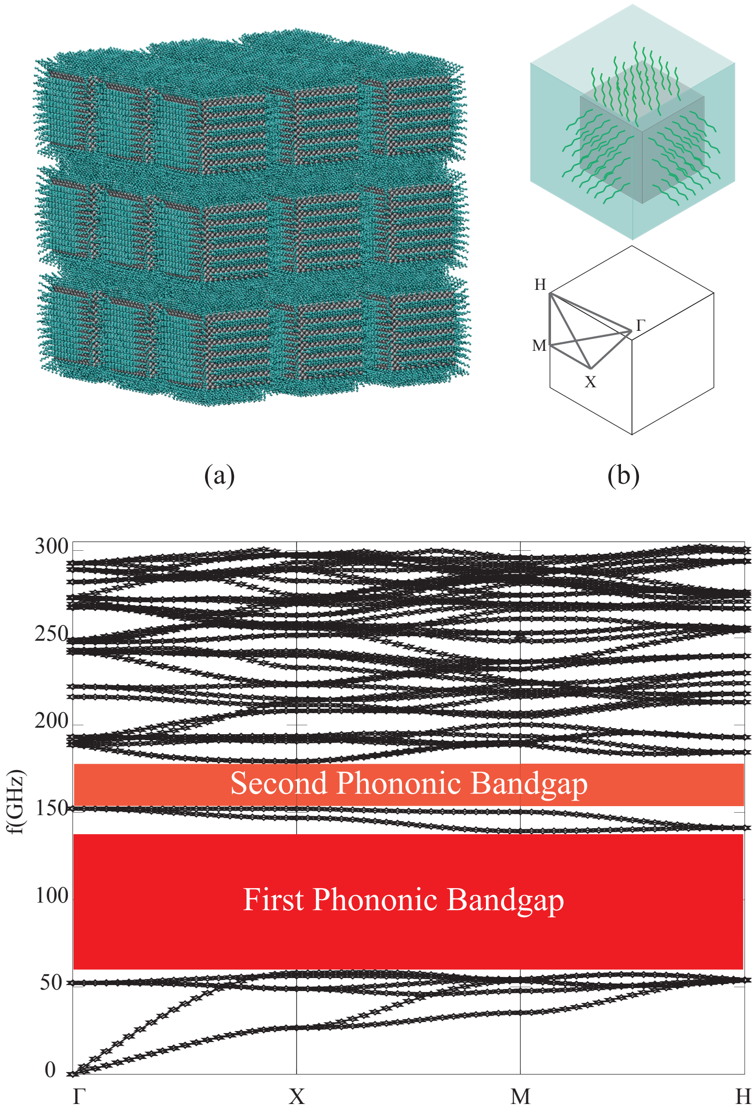

(a) (b)

(c)

Figure 4.1: (a) Simple cubic 3D superlattice with cubic nanocrystal building blocks. (b) A representative unit cell used in band struture calculations (top figure) and the corresponding first Brillouin Zone in **k**-space (bottom figure) . The unit cell edge length is 7.5 nm with a cubic core edge length of 5.5 nm. (c) Phonon dispersion curve of the cubic NCSL. The red and orange regions indicate the first and the second complete phononic bandgaps.

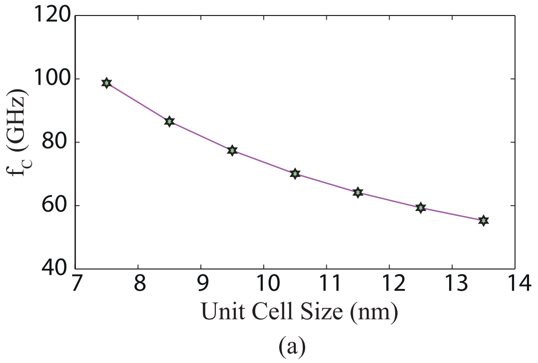

(a)

(b)

Figure 4.2: (a) First Bandgap central frequency as a function of unit cell size for cubic NCSLs. (b) Bandgap width as a function of unit cell size.

kept constant in these calculations. In Fig. 4.2 (a) and Fig. 4.2 (b), the variations of f_C and the larger bandgap width versus the unit cell size are shown. We observe that the central frequency and bandgap width decrease with increasing unit cell size which is consistent with previously observed trends for phononic crystals [92]. Doubling the core size decreases the bandgap widths and central frequencies are decreased by about 50% which suggests an approximate inverse proportionality between the unit cell size and the bandgap central frequency and width. This plot also shows that NCSLs with nanocrystals of different core size can provide an effective way to tune bandgaps and thus filter waves with specific wavelengths and frequencies.

We also studied the effect of the core volume fraction (ϕ) on the bandgaps of the NCSLs. ϕ is defined as the ratio of the core volume to the unit cell volume of the nanocrystals. We performed band structure calculations for simple cubic NCSLs with cubic building blocks of different core volume fractions by changing the ligand length for the same core to obtain different volume fractions. To study the trend more carefully we considered two different sizes for the building blocks of the superlattice with cube edges of 5.5 nm and 10 nm. In Fig. 4.3 (a), the width of the phononic bandgap (corresponding the to larger bandgap) is plotted as a function of the core volume fraction for both NCSLs. The bandgap width does not change monotonically with the volume fraction; rather it shows a maximum bandgap corresponding to a volume fraction around $\phi = 0.4$. This value of ϕ, as shown in Fig. 4.3 (a), was obtained independently for both superlattices with different core sizes. It corresponds to a volumetric combination of the core and the surrounding ligands that maximizes the effect of material property difference in introducing bandgaps; for the two ends of the spectrum, $\phi = 0$ and $\phi = 1$, no acoustic mismatch and thus no bandgaps would be present in the system. The fact that this value is the same for different core sizes in Fig. 4.3 (a) also implies that the value of ϕ corresponding to this peak is essentially dependent on the shape of the nanocrystal and the material properties. We also performed bandgap calculations for similar systems by considering the same cubic shape for the core with elastic moduli half of that in platinum cubic cores and we observed a peak in PBG width at $\phi = 0.32$. Similarly, keeping the material the same and changing the core shape from a cube to a sphere resulted in $\phi = 0.5$ for the peak. This shows that the interplay between nanocrystal shape and material determines the volume fraction that maximizes bandgap width.

Next, we consider bandgap variations resulting from nanocrystals organizing into different types of superlattice structures. Fig. 4.3 (b) shows the larger bandgap width of cubic nanocrystals forming simple-cubic (SC) and face-centered cubic (FCC) superlattices. Both structures have been observed experimentally [9]. The SC structure shows around 33 % larger bandgap compared to the FCC structure. The FCC superlattice has a

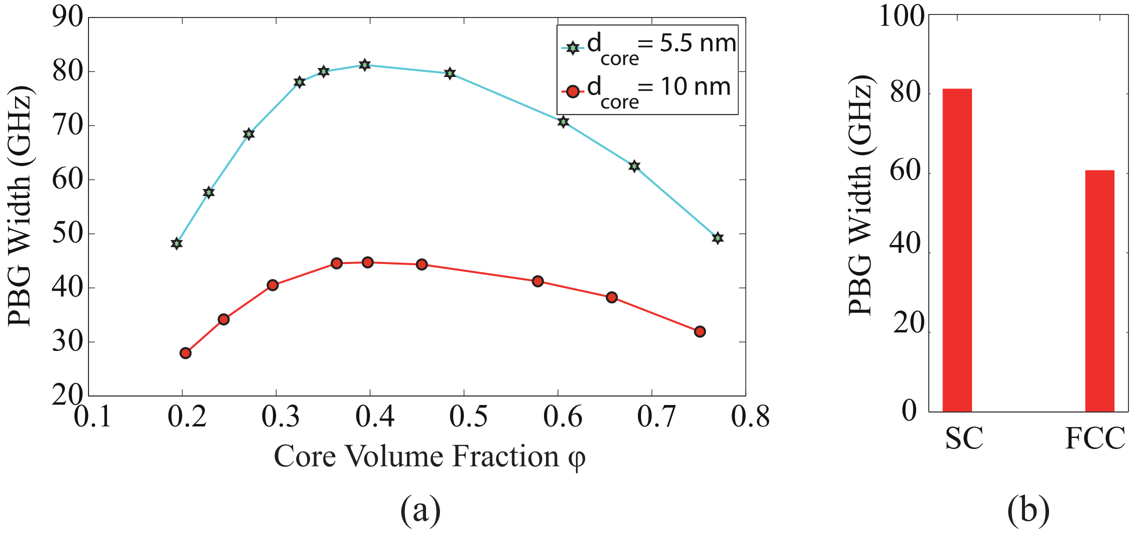

(a) (b)

Figure 4.3: (a) Phononic bandgap width of simple cubic NCSLs with cubic building blocks as a function of core volume fraction. (b) Bandgap width for NCSL of cubic building blocks with simple cubic and face-centered cubic structures.

larger unit cell size which is consistent with having a smaller bandgap. This result shows that through changing the superlattice structure, significant variations are introduced to phononic bandgaps with bandgap widths changed by as much as about 30% .

Nanocrystal shape provides another way to tune NCSL band gaps. In addition to cubic NCSLs, we also studied the band structure of simple cubic superlattices with PbSe octahedron [8] and gold nanorod [129] building blocks, as shown in Fig. 4.4. The octahedron and nanorod superlattices present smaller bandgap widths than the Pt cube superlattices studied previously: around 24 GHz and 50 GHz, respectively. In general, the width of the bandgap is expected to increase with the difference between the densities and elastic properties of the components that introduce the phononic mismatch. Consistent with this fact, in our case the difference between properties of the core and

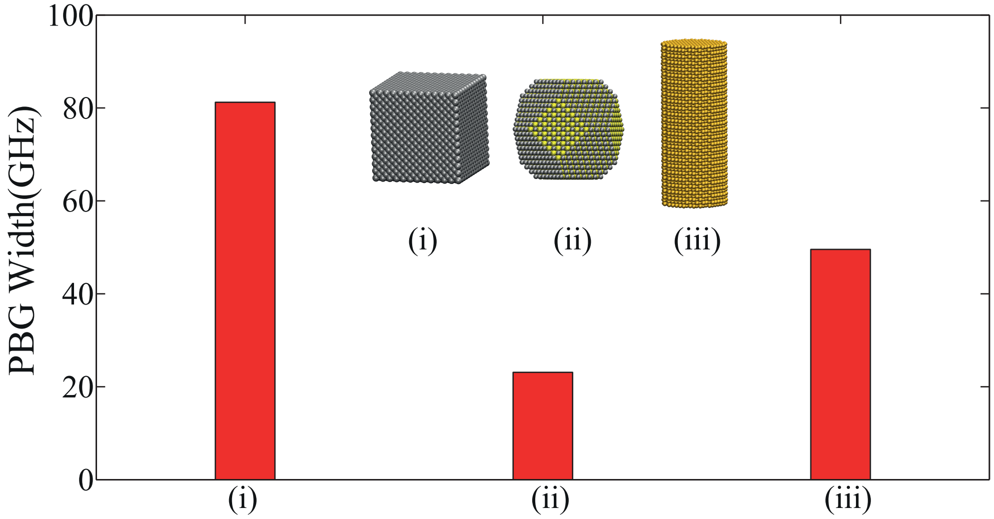

Figure 4.4: Bandgap width for NCSL with building blocks of different shapes. The cubic core is 5.5 nm is size, the octahedron is a 6 nm nanocrystals, and the nanorod is 11 nm in diameter and 50 nm in length.

the ligands is the largest for the cubic nanocrystals, and the smallest for the octahedron nanocrystals (see Methods).

We have also calculated the phonon band structure of the different BNSLs described in Ref. [3]. A schematic drawing of these BNSLs is shown in Fig. 4.5 (a). Each BNSL consists of two different types of nanocrystals organized in a specific crystal structure. Sample dispersion curves for cubic Cu_3Au and hexagonal AlB_2 type structures are shown in Fig. 4.5 (b), and (c). One interesting observation is that the first bandgap is the larger bandgap for the cubic superlattice while it is the opposite for the hexagonal structure. The smaller of the two bandgap widths in both BNSLs are about a few GHz, which is much narrower than the corresponding smaller bandgap in NCSLs with one type of nanocrystal. The larger bandgap width for different BNSLs is shown in Fig. 4.5 (d).

AlB_2 and CuAu type structures show the largest bandgaps width of 61 GHz and 77 GHz respectively. The CaB_6 structure on the other hand, present very small bandgap width of 1.1 GHz. This wide range of achievable bandgaps demonstrates that BNSLs in general provide more flexibility in tuning bandgaps compared to NCSLs with only one type of nanocrystal. This is due to a combination of a larger variety of available nanoparticle types as well as the different structures that BNSLs can assume compared to simple or face-centered cubic structures that are often observed for NCSLs with one type of nanocrystal. The photonic bandgaps and the photonic band structure of binary photonic crystals have also shown similar behavior. Previous studies of photonic crystals [130, 131, 132], have shown existence of one or two bandgaps as well as the existence of very small and large bandgaps in binary systems. Our results show that BNSLs provide equivalent tunable phononic bandgaps.

NCSLs and BNSLs studied here provide great opportunities for engineering and manipulating phononic band structure. For superlattices with only one type of nanocrystal as the building block, changing core size, volume fraction, superlattice structure, and core shape can help tune the bandgap width and central frequency. Using these parameters, we can design superlattice structures that filter out frequencies between 30 GHz and 100 GHz. Choosing a core volume fraction of about $\phi = 0.4$ will help design a superlattice with maximum bandgap width. Using nanocrystals of different shape such as octahedrons and nanorods, we can reduce the bandgap width by as much as 75% and 40% respectively compared to the cubic nanocrystals. The structural variety of BNSLs provides even better opportunities for tuning and controlling phononic bandgaps. The CaB_6 structure is useful for designing pass bands since they present a very small bandgap. NaCl and Cu_3Au

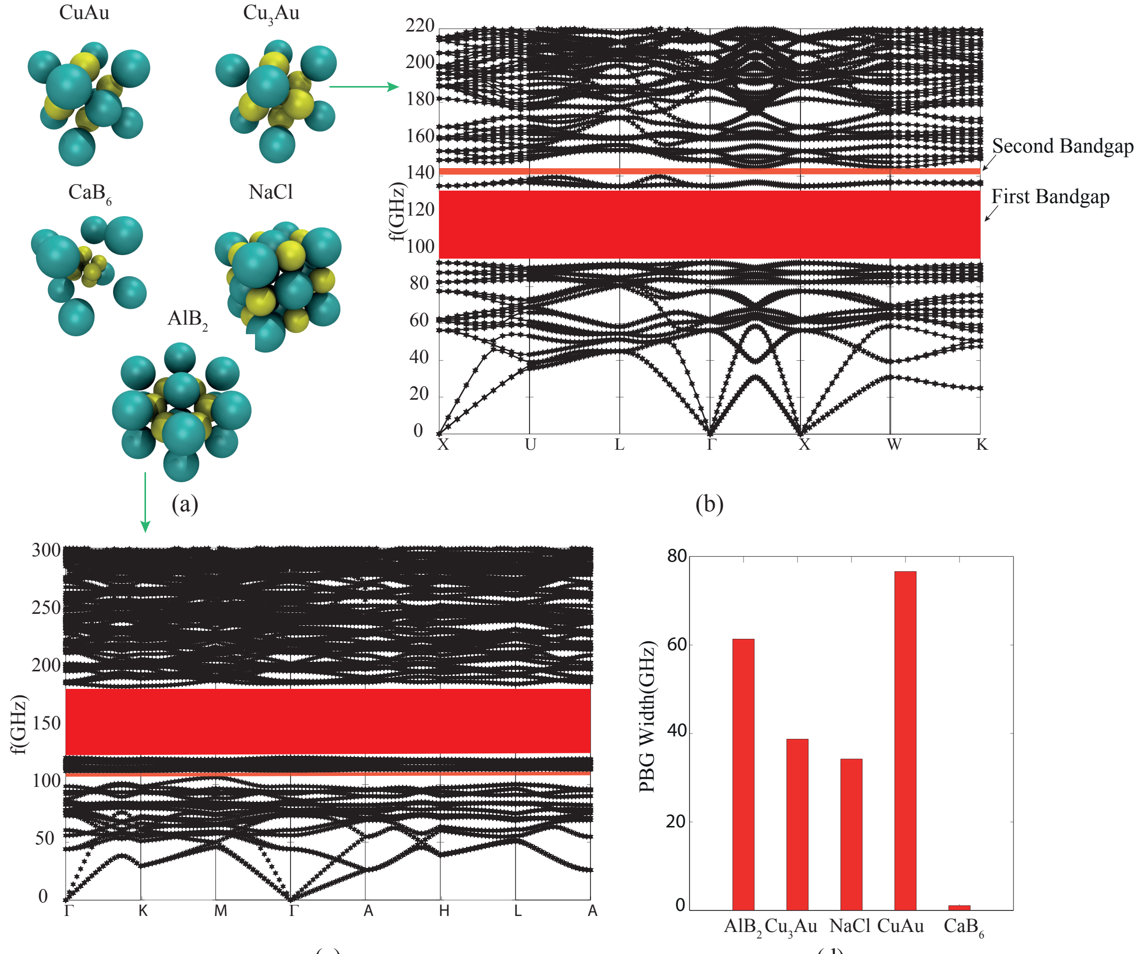

(a) (b)

(c) (d)

Figure 4.5: (a) Schematic picture of the crystal structure of different binary nanocrystal superlattices described in Ref. [3]. CuAu structure with 7.6 nm PbSe and 5.0 nm Au nanocrystals; Cu_3Au structure with 7.2 nm PbSe and 4.2 nm Ag nanocrystals; CaB_6 structure with 5.8 nm PbSe and 3.0 nm Pd nanocrystals; NaCl structure with 13.4 nm $\gamma - Fe_2O_3$ and 5.0 nm Au nanocrystals; AlB_2 structure with 6.7 nm PbS and 3.0 nm Pd nanocrystals. (b) and (c) Phononic band structure of cubic Cu_3Au and hexagonal AlB_2 structures. (d) Bandgap width for the larger bandgaps of the BNSLs described in (a).

BNSLs present larger bandgaps. CuAu and AlB_2 structures increase the bandgap width by almost a factor of two and are thus more suitable for designing acoustic filters.

Finally it is worth mentioning that the elastic moduli of the nanocrystals may deviate from those of the bulk, especially for smaller sizes [133, 134]. To study this effect, we also calculated the bandgap width of Pt cubic crystals by increasing or decreasing the core Young's modulus by as high as 50%. As a result, we observed as high as 5% change in the bandgap width. However, the general trends and tunable effects observed in this work will still hold independent of the specific choice of the properties. In order to take into account the effect of local size-dependents properties one can also consider Raman spectroscopy data for different nanoparticles [135] which helps adjust dispersion curve calculations by comparing specific optical phonon frequencies to experimental measurements. For future studies, such Raman measurements or better experimental evaluation of elastic moduli of the nanocrystals can provide more realistic inputs to computational studies.

4.4 High Frequency Phonons in NCSLs: Atomistic Model Case Study

In this section we investigate phonon dispersion calculations for NCSLs using atomistic models. As mentioned earlier, the finite element calculations are usually accurate for frequencies below 1 THz and atomistic models are needed to represent higher frequencies. However, atomistic models suffer from high computational cost as well as the lack of suitable force fields that effectively describe particle interactions for many of the experimentally synthesized NCSLs. In fact, for the BNSLs and NCSLs of different shapes studied in previous sections, there are no established atomistic potentials that can describe the interatomic forces accurately and at the same time preserve the specific shape of the building blocks. For this reason, we turn our attention to the spherical gold nanoparticles studied in section 3.3.2. Using the relaxed structure of gold nanocrystals, lattice dynamics calculation is performed to capture the full phonon spectrum of the superlattice.

4.4.1 Lattice Dynamics Model for Gold Nanocrystal Superlattice

Revisiting the basics of the lattice dynamics method, the dynamical matrix D is a $3n_{cell} \times 3n_{cell}$ matrix where n_{cell} is the number of atoms per unit cell. The unit cell can be chosen as either the primitive unit cell or the conventional unit cell [136]. For a FCC nanocrystal superlattice the primitive unit cell can be considered as a single nanocrystal with n_{nc} atoms per basis where n_{nc} is the total number of core and ligand atoms for one nanocrystal. The dispersion curve will therefore have $3n_{nc}$ branches. In order to calculate the components of the dynamical matrix we need to consider the nearest neighbors of the unit cell [90] which for FCC superlattice structures includes 12 neighboring nanocrystals.

In order to calculate the dynamical matrix, the initial configuration of each nanocrystal is prepared according to the interatomic interactions and the procedure described in section 3.3.2. Then this initial configuration is cooled down to an arbitrarily low temperature of $T = 0.001K$ using the NVT ensemble with the Nose-Hoover thermostat [32]. Next, the nanocrystals are placed at FCC unit cell positions with a fairly large initial lattice parameter [39]. Finally, the superlattice structure is relaxed using NPT ensemble at zero pressure with periodic boundaries [39]. The interatomic force constants are then calculated by moving atom j of the reference nanocrystal (0) and calculating the forces on atom j' of nanocrystal l'. Each nanocrystal consists of 100 atoms (44 core gold atoms plus 56 capping ligand atoms) resulting in a supercell with 100 atoms. Due to the small number of atoms, the core is not exactly spherical but rather octahedral or tetrahedral in shape.

4.4.2 Results and Discussion

The phonon dispersion curves calculated for the FCC gold superlattice are presented in Figs. 4.6 (a) and 4.6 (b). Fig. 4.6(a) shows the full dispersion. Fig. 4.6 (b) shows the low frequency region of the dispersion curve, where the three acoustic modes (in red) are shown with several low frequency optical modes. As far as the contribution of core and ligand atoms, the core atoms will contribute to frequencies below the highest allowable frequency observed in bulk gold which is around 5 THz [137]. Higher frequency optical modes arise from faster vibrations in ligand atoms. Similar to phononic crystals [107, 138], phonon band gaps can be studied from the dispersion curves. For this structure, we observe small band gaps in the 8 to 13 THz range and also in the 20 to 26 THz range. A larger band gap is observed in the 13 to 20 THz range. The dispersion curve also shows the maximum allowed frequency for phonons in the superlattice to be about 26.6 THz. Most of the optical branches are observed to be nearly flat curves with small group velocities suggesting that their contribution to thermal transport is insignificant. Similar behavior has been observed for optical branches of structures with large numbers of particles per unit cell [139].

The acoustic modes of the dispersion curve are related to elastic properties of the superlattice. Elastic stiffness constants can be derived from the slope of acoustic branches

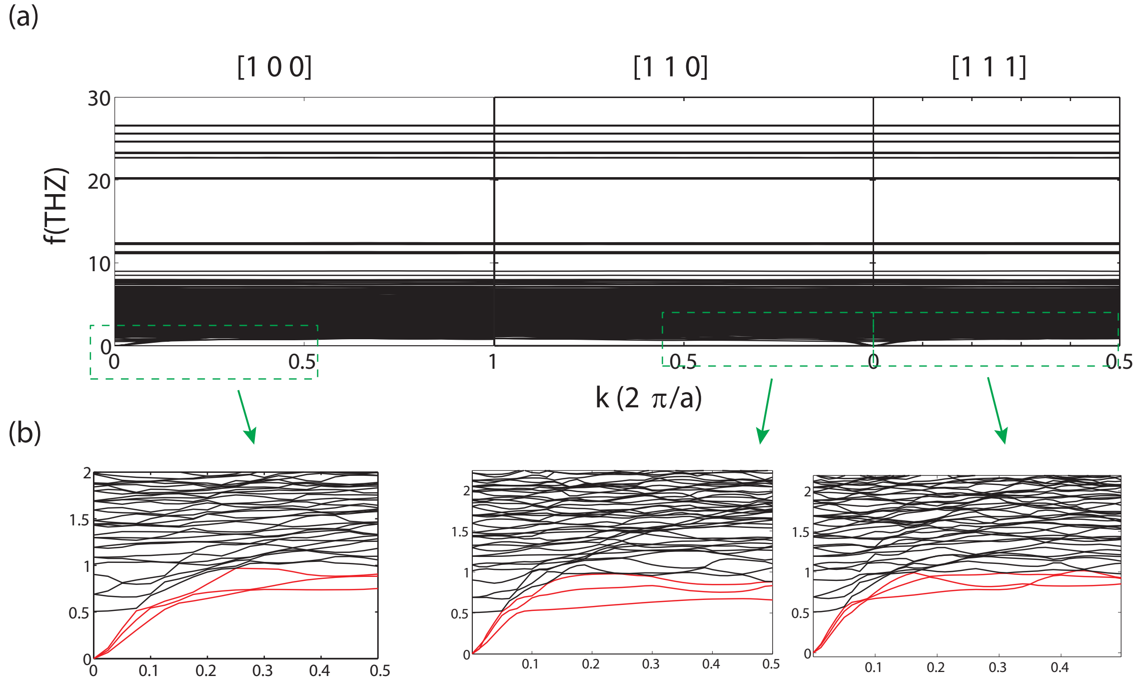

Figure 4.6: (a) Phonon dispersion curve of gold nanocrystal superlattices. (b) The low frequency modes of the dispersion curve. Three acoustic modes (in red) are distinguished from the optical modes. The middle plot has been rotated to be consistent with the other two plots.

in the long wave length limit. We can calculate $C_{11} = \rho(\frac{d\omega_{[100]}}{dk})^2$ as $k \rightarrow 0$, using the slope of the longitudinal acoustic mode in the [1 0 0] direction [90]. We obtain a value of $C_{11} =$ 15.7 GPa. This value can be compared to results from direct MD calculations. Using Young's (E) and bulk (B) modulus of gold superlattices obtained in Ref. [39], the value of $C_{11} = \frac{3EB+9B^2}{9B-E}$ is about 10.4 GPa which shows reasonable agreement with the prediction from the dispersion curves. Here the exact values of the two calculations are not expected to match as the size (3.5 nm) and ligand type (alkylthiol) for reported MD calculations [39] is different from the system that we used for LD calculations in our system. The smaller ligand chains bonded to the core atoms in our calculations form a stiffer structure compared to the longer, more freely moving ligands in Ref. [39] which explains the higher value of elastic stiffness constant obtained here. Importantly, the dispersion curves in Fig. 4.6 (a) show the existence of full phonon band gaps in all directions. We also observe a strong similarity among dispersion curves belonging to different superlattice symmetry directions, particularly at high frequencies. This may arise from the fact that ligands, which provide the only contribution to high frequency vibrations, have a spatially isotropic distribution in the relaxed nanocrystal (Fig. 3.6(a)). To further investigate, we estimate the anisotropy from the parameter $A = \frac{2c_{44}}{c_{11}-c_{12}}$, where $A = 1$ represents an isotropic material [140]. c_{44} and c_{12} were calculated from the transverse [1 0 0] and slow transverse [1 1 0] acoustic wave velocities [141]. Here the resulting values of $c_{44} = 8.01$ GPa and $c_{12} = 4.39$ GPa result in anisotropy of about 1.4. This estimate reveals a small degree of anisotropy in the low frequency, low wavevector continuum limit which is consistent with slight differences in the acoustic branches shown in Fig. 4.6 (b). For comparison it is observed that the anisotropy lies between that of bulk argon (1.3)[141] and bulk silicon (1.6)[140]. It is important to note here that the elastic stiffness calculations are approximate, as the equations used for such calculations are originally derived for bulk atomic crystals [140]. Their generalization to NCSL, in which the unit cells are very large with complex atomic arrangements that can vary slightly depending on initialization, may introduce small errors.

4.5 Conclusion

In this chapter, we calculated the phononic band structure of a variety of NCSLs with different shapes and structures. We showed that through changing the core volume fraction, nanocrystal size, shape, and the superlattice structure phononic bandgaps can be tuned and manipulated for different design purposes. Binary structures were also studied which show an even wider range of tunable phononic band structures useful for manipulating pass bands or stop bands. Such tuning presents new opportunities for phononic effects similar to well-known photonic behavior such as waveguiding and signal filtering. This work also motivates future experimental studies for measuring phononic band structure of NCSLs and BNSLs with different shapes, sizes and structures as well as using them for designing effective sound and heat manipulation devices.

Chapter 5

One-way Phonon Isolation

5.1 Overview

In the previous chapters we have studied phonons in nanocrystal superlattices. The interesting phononic properties of NCSLs and phononic crystals in general are promising for many interesting applications that involve engineering and manipulating phonons. For example thermal diodes and rectifiers have attracted great interest [142]. In such problems, the focus is to achieve different heat current flow in forward and backward directions passing through a device. Another interesting problem is to pay attention to individual phonons and manipulate their transmission in different directions. In this chapter, the idea of one-way isolation of individual phonons is proposed. We adopt a more fundamental type of analysis by considering individual phonons in acoustic waveguides and graphene nanoribbons. We show that one-way isolation is possible by introducing a spatio-temporal modulation of mechanical properties. This idea is quite general and can be used beyond these sample systems. At the same time, similar to the comparison between phononic versus photonic crystals discussed in the previous chapter, this chapter reflects on the similarities between phonon and photon isolation within the framework of acoustic-electromagnetic analogy.

5.2 One-way Phonon Isolation in Acoustic Waveguides

5.2.1 Introduction

Recent progress in microfabrication and microelectromechanical systems (MEMS) has highlighted the potential of compact and miniaturized devices for on-chip acoustic signal generation, detection, manipulation and processing [143, 144]. In particular, many important MEMS-based applications have been suggested lately, including acousto-optic modulators [145], acoustic MEMS filters [146], and biosensors [147]. A typical device consists of several key components, which include resonant transmitters and receivers that generate and receive mechanical vibrations, and a signal transmission line, i.e. waveguide network, along which phonon waves are guided between the signal processing modules [148]. Common examples of such transmission lines include surface acoustic wave (SAW) delay lines [149, 150] and flexural plate waveguides [151].

An important challenge facing on-chip acoustics is the design of modularized components placed on the same integrated platform that manipulate an acoustic signal independently of each other [152, 153]. To reach such functionality it is critically important to develop one-way interconnects that isolate different components from specific vibrational modes. Such interconnects, being somewhat similar to electronic diodes, transmit a desired signal in one direction only, and provide the potential to build one-way communication channels for acoustic waves.

Recently, the concept of acoustic rectification has attracted great interest [154, 155, 156, 157, 158]. Based on a nonlinear frequency conversion mechanism, the idea of an acoustic diode was proposed theoretically and demonstrated experimentally [157, 159]. In these systems a direction- dependent nonlinear frequency conversion is achieved due to the structural asymmetry of the geometry [157, 159]. However, the low frequency conversion efficiency implies low transmission properties of such isolators [159, 160]. Furthermore, such devices are often quite bulky and would be difficult to implement as isolating interconnects for on-chip acoustics applications. A similar mechanism of nonlinear isolation has also been employed in optical systems, using a combination of nonlinearity and structural asymmetry [161, 162].

In Refs. [163, 164] another conceptually different mechanism for highly efficient optical isolation in a waveguide was proposed by Yu and Fan. There, it was shown that the symmetry of wave propagation in an optical waveguide in forward and backward directions can be broken with spatio-temporal modulations of the waveguide properties. Such symmetry breaking is achieved due to a one-way conversion between the guided modes. Inspired by this work, we apply this principle for the analogous design of an acoustic waveguide isolator.

In this section we study phonon wave propagation in an acoustic waveguide and demonstrate that the symmetry of wave propagation may be broken by introducing spatio-temporal modulation of waveguide properties such as density or elastic stiffness. We show that in one of the propagation directions coupling and conversion between the waveguiding modes occurs, whereas in the other direction the signal is transmitted without any perturbations, analogous to the optical case. Using analytical techniques and numerical simulations, we also show that such a mode conversion may be employed for the design of miniaturized acoustic isolators. Furthermore, we discuss possibilities for experimental realization and other potential applications of such a device.

5.2.2 Governing Equations and Results

Figure 5.1(a) shows the geometry of our problem. In particular, we consider an unbounded plate acoustic waveguide with thickness b. Such a waveguide supports shear horizontal (SH) waves, i.e. waves of transverse displacement, as well as Lamb waves which are longitudinal waves traveling along the waveguide [165]. These waves propagate in the waveguide independently of each another; therefore they can be studied separately. For the sake of simplicity, we will consider propagation of SH waves in a two-dimensional cubic crystal waveguide, where there is no field variation in the z direction. The principles developed in this work can be easily extended to the case of Lamb waves. We write the Helmholtz type wave equation for SH waves as follows [165]:

$$\rho \frac{\partial^2 u_z}{\partial t^2} = \frac{\partial T_{xz}}{\partial x} + \frac{\partial T_{yz}}{\partial y} \tag{5.2.1}$$

where ρ is the density of the material, $T_{xz} = c_{44} \frac{\partial u_z}{\partial x}$ and $T_{yz} = c_{44} \frac{\partial u_z}{\partial y}$ are components of the stress tensor and c_{44} is a component of the elastic stiffness tensor for a cubic crystal.

For a planar waveguide with constant density and stiffness, the dispersion relation for the SH waves is $k^2 = (\frac{\omega}{V_s})^2 - (\frac{n\pi}{b})^2$, where $V_s = (c_{44}/\rho)^{\frac{1}{2}}$ is the shear wave velocity in a bulk medium, and $n = 0, 1, 2, 3, 4, ...$ denotes the mode number. In Fig.5.1(b) we plot the first two phonon dispersion branches, i.e. symmetric mode with n=0, henceforth denoted

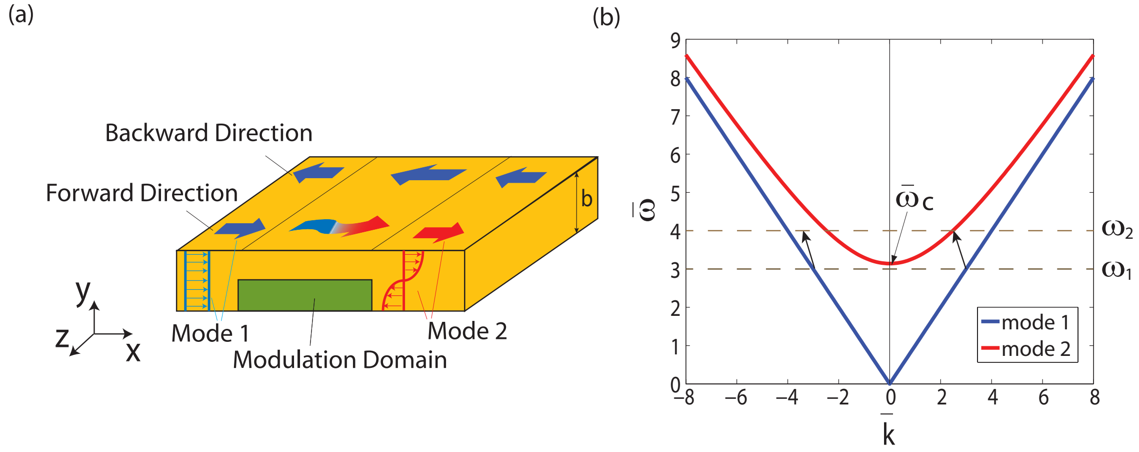

Figure 5.1: (a) Unbounded plate acoustic waveguide with stress free surfaces. The shaded area denotes the domain where material properties are spatio-temporally modulated. (b) Dispersion curves for the first two SH modes of the waveguide. $\overline{k} = k\,b$ and $\overline{\varpi} = \omega b/V_s$ are normalized wavevector and angular frequency, respectively. Arrows indicate the direction of interband transition due to spatio-temporal modulation of the acoustic waveguide.

mode 1, and antisymmetric mode with n=1, henceforth denoted mode 2. We note that below the cut-off frequency, $\omega_c = \frac{V_s \pi}{b}$, only the symmetric branch exists.

Clearly, the dispersion curves plotted in Fig.5.1 (b) are symmetric with respect to wave number k. This implies that the wave propagation in such a waveguide is reciprocal: i.e. waves traveling in forward and backward directions have the same properties. In order to break this symmetry in the wave propagation we follow the technique suggested in Refs. [163, 164]. In particular, we consider wave propagation in a spatio-temporally modulated waveguide. In this case we expect that for an appropriately chosen modulation, one-way conversion of one guided mode to another may be induced in one of the propagation directions only.

Here we assume a simple harmonic modulation of the form $P = P_0 + \delta P \cos(\Omega t - K\,x)$, where P_0 stands for either the elastic stiffness constant c_{44} or the density ρ, and δP is the modulation depth. Without loss of generality, we will explain the method for density modulation first. The general solution for Eq. 5.2.1 can be written as a superposition of the guided modes: $u_z = a_1(x) u_z^{(1)} \exp i(\omega_1 t - k_1 x) + a_2(x) u_z^{(2)} \exp i(\omega_2 t - k_2 x)$, where $k_{1,2}$ and $\omega_{1,2}$ are the wavevectors and frequencies of mode 1 and mode 2, $u_z^{(1)}$ and $u_z^{(2)}$ are their profiles (see Fig. 5.1 (a)), and $a_1(x)$ and $a_2(x)$ are their slowly varying spatial amplitudes. Exponentials are used here for mathematical convenience; the real part of the general solution represents the actual physical displacement. Using the standard techniques of perturbation theory, we derive a system of first-order ordinary differential equations for slowly varying amplitudes (detailed derivation can be found in appendix A):

$$\frac{d^2}{dx^2}\begin{pmatrix} a_1 \\ \\ a_2 \end{pmatrix} = \begin{pmatrix} -A_{12}A_{21}\exp i(k'x) & 0 \\ \\ 0 & -A_{21}A_{12}\exp i(k'x) \end{pmatrix}\begin{pmatrix} a_1 \\ \\ a_2 \end{pmatrix} \tag{5.2.2}$$

where $k' = k_2 - k_1 - K$ and $A_{pq} = \frac{\delta\rho\omega_q^2 \int_M u_z^{(q)} u_z^{(p)*} dy}{4c_{44}k_p \int_W u_z^{(p)} u_z^{(p)*} dy}$. Here $\{p, q\}$ represents either of $\{1, 2\}$ or $\{2, 1\}$ combinations, and $u_z^{(p)*}$ is the complex conjugate of $u_z^{(p)}$. $\int_W$ is performed over the whole waveguide thickness along the y axis and $\int_M$ is performed only over the modulation domain. Based on the incoming signal angular frequency ω_1 and the available modulation frequency Ω, a full mode conversion from mode 1 to mode 2 occurs for waves propagating in the positive x direction when $\omega_2 = \omega_1 + \Omega$ and when the K of the modulation is chosen such that $K = k_2 - k_1 = [(\frac{\omega_2}{V_s})^2 - (\frac{\pi}{b})^2]^{\frac{1}{2}} - \frac{\omega_1}{V_s}$. In order to maximize the coupling between the modes, or equivalently maximize the mode overlap integral for constants A_{12} and A_{21}, only half of the waveguide is modulated. Fig. 5.1 (b) shows the one-way isolation in this system. Waves of mode 1 propagating in the positive x direction, corresponding to $(+k_1, \omega_1)$ on the dispersion curve, are converted to mode 2 at $(+k_2, \omega_2)$. However, waves of the same wavelength and frequency that propagate in the negative x direction, corresponding to $(-k_1, \omega_1)$, cannot undergo mode conversion because the end point of the intended transition via the modulation $P = P_0 + \delta P \cos(\Omega t - K\, x)$ does not lie on mode 2 or on any other branches of the dispersion curve. Analogous to the optical case in Refs [163, 164], this behavior arises because the spatio-temporal modulation breaks both time-reversal and spatial-inversion symmetry.

The real part of the general solution of Eq. 5.2.2 is $u_z = \cos(\xi x) u_z^{(1)} \cos(\omega_1 t - k_1 x) + \sin(\xi x) u_z^{(2)} \cos(\omega_2 t - k_2 x)$ where $\xi = (A_{12}A_{21})^{\frac{1}{2}}$ is the conversion wavevector with the corresponding conversion length of $l_c = \frac{\pi}{2\xi}$. Using $u_1 = 1$ and $u_2 = \sin(\frac{\pi y}{b})$ as the mode profiles [165], we obtain $\xi = \frac{\delta\rho\omega_1\omega_2}{\pi c_{44}}\sqrt{\frac{1}{8k_1k_2}}$ and $l_c = \frac{\rho\pi^2V_s^2\sqrt{8k_1k_2}}{2\delta\rho\omega_1\omega_2}$. As expected, the convergence length is inversely proportional to the modulation depth. The conversion length will also be smaller for smaller values of shear wave velocity V_s. To analyze the conversion length, we investigate its dependence on the modulation parameters. We attain one-way mode conversion of an incoming signal by introducing a modulation domain with modulation frequency Ω and tunable modulation wavenumber K. As discussed earlier, signal at frequency ω_1 and wavenumber k_1 will be transformed to another mode with frequency $\omega_2 = \Omega + \omega_1$ and wavenumber k_2, where k_2 is simply determined from ω_2 and the corresponding dispersion relation for mode 2. Therefore, we have two independent design parameters, k_1 (or ω_1) and Ω. In terms of these design parameters we have $l_c = (\frac{\sqrt{2}\rho\pi^2V_s}{\delta\rho})\frac{((k_1+\frac{\Omega}{V_s})^2-(\frac{\pi}{b})^2)^{\frac{1}{4}}}{\sqrt{k_1}(k_1V_s+\Omega)}$. A plot of this conversion length for different values of Ω is shown in Fig. 5.2 (a). As we can observe in this plot, there is a minimum allowable value $k_1 = \frac{\pi}{b} - \frac{\Omega}{V_s}$ that corresponds to $l_c = 0$, for which $\omega_2 = \omega_c = \Omega + \omega_1$ and $k_2 = 0$. In this case the second mode is not a propagating wave which means we cannot have a conversion of mode 1 to a propagating wave of mode 2. Below this value of k_1, $\omega_2 = \omega_1 + \Omega$ does not exist and mode conversion is not possible. For k_1 above this minimum, we will have physically meaningful values for conversion length and mode conversion is observed. The conversion length increases with k_1 to reach a maximum that corresponds to minimum coupling between the modes. l_c will then decrease as it varies proportional to $\frac{1}{k_1}$ for large values of k_1. This type of plot is helpful in choosing the appropriate modulation length for acoustic waveguide design based on available values of Ω and other system parameters.

Moving further, we consider a slab waveguide similar to surface acoustic wave [150] and flexural plate wave [151] devices widely used in MEMS applications. To be more specific, we assume that the waveguide is $10\,\mu m$ thick silicon, with $c_{44} = 80GPa$ and $\rho_0 = 2000\frac{kg}{m^3}$.[165] The modulation depth $\delta\rho$ is chosen to be $0.1\rho_0$. It is worth mentioning that smaller values of the modulation depth will also provide the same one-way isolation effect. However, the required conversion length in this case will be larger. Furthermore, we consider the propagation of the mode 1 phonon with frequency $\omega_1 = 0.8\omega_c$, i.e below cut-off frequency ω_c which guarantees that at frequency ω_1 the acoustic waveguide supports only a single fundamental symmetric mode. Choosing the modulation frequency $\Omega = 0.4\omega_c = 0.8GHz$, we expect a full conversion into mode 2 after $l_c = 13.5\lambda_1$ where $\lambda_1 = \frac{2\pi}{k_1} = 25\,\mu m$, which is about 33 times the thickness of the waveguide.

While spatial density modulations of order 10% are difficult to achieve in bulk material, modulations up to about 99% have already been achieved in silicon-based phononic crystals with spatial periodicities of order $500 - 800$nm [166] and 10μm $-$ 10mm. [167] Such phononic crystals have the potential to improve the quality factor and yield of high-frequency Lamb-wave devices including waveguides, resonators, and filters [167]. Temporal property variation is also possible in practice, although more difficult to achieve. Dong et al. [168] realized a time-varying phononic crystal [169] by periodically varying the fluid medium between an acoustic wave source and detector via a rotating drum experiment. Modulation depths of 53% and 10%, respectively, were achieved for density and bulk modulus.

Other groups have experimentally demonstrated dynamically tunable material properties in solid state systems. Jang et al. [170] applied mechanical strain to PDMS/air phononic crystals to modify the phononic band structure. Casadei et al. [171] used an electrically driven array of piezoelectric resonators to tune phononic band structure and

Young's modulus in an aluminum phononic crystal plate. Cullen et al. [172] varied the magnitude and direction of a magnetic field applied to the rare earth iron compound $Tb_0.3Dy_0.7Fe_2$ and obtained a 50% change in the c_{44} elastic constant. Varga et al. [173] observed a similar change in the elastic modulus with magnetic field for an anisotropic composite of PDMS and chained carbonyl iron particles. While the above examples have not involved periodic modulation, it is feasible to apply mechanical strain, voltage, and magnetic fields to solid materials in a periodic fashion to obtain such modulation.

Furthermore, for mode 1 propagating in the waveguide, we have $a_1(0) = 1$ and $a_2(0) = 0$ since before encountering the modulation domain, the symmetric mode is the only mode present in the waveguide. Based on these conditions, the solution to Eq. 5.2.2 that describes the combination of the modes inside the modulation domain is written as $a_1(x) = \cos(\xi x)$ and $a_2(x) = \sin(\xi x)$, as plotted in Fig. 5.2 (b). Complete transition from mode 1 to mode 2 occurs after the wave propagates a distance l_c.

Next, we investigate numerically the wave propagation in such a waveguide with the help of the finite element method. In this case we consider that a small section of the waveguide with length l_c is modulated. The results of the numerical simulations are shown in Fig. 5.3. We observe a good agreement between analytical predictions and numerical simulations. When mode 1 propagates in the forward direction, we observe full conversion to mode 2 induced by spatio-temporal modulation. On the other hand, when mode 1 propagates in the opposite direction, the modulation has no effect on the traveling wave and the waveguide does not allow the conversion to happen. Therefore, time reversal symmetry is broken, analogous to observations for optical waveguides [163, 164].

We have also considered the case of elastic stiffness constant modulation such that

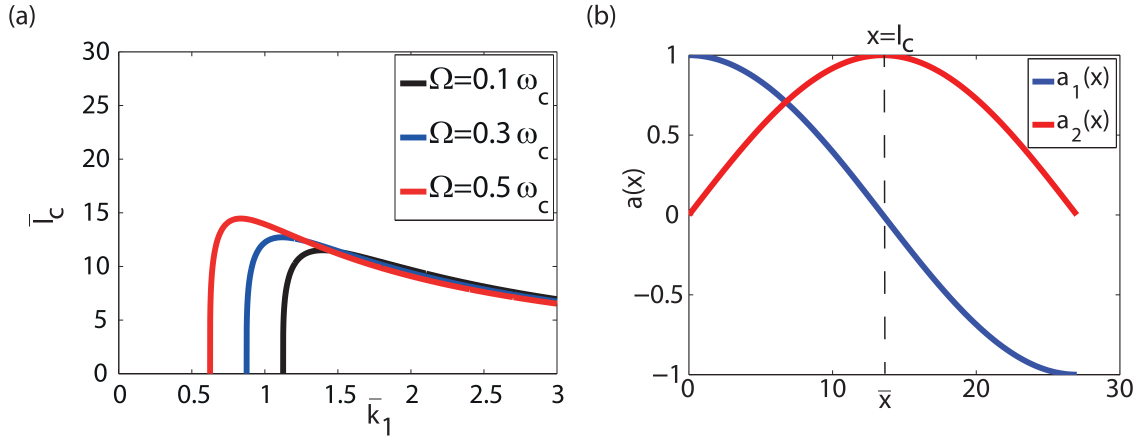

Figure 5.2: (a) Conversion length as a function of mode 1 wavenumber k_1 and modulation frequency Ω with $\delta\rho = 0.1\rho$. $\overline{l_c}$ and $\overline{k_1}$ are normalized values of l_c and k_1 with respect to wavelength and wavenumber of mode 1 at frequency ω_1, respectively. (b) Variation of slowly varying amplitudes along the modulation domain for a waveguide with $\Omega = 0.4\omega_c$ and $\omega_1 = 0.8\omega_c$.

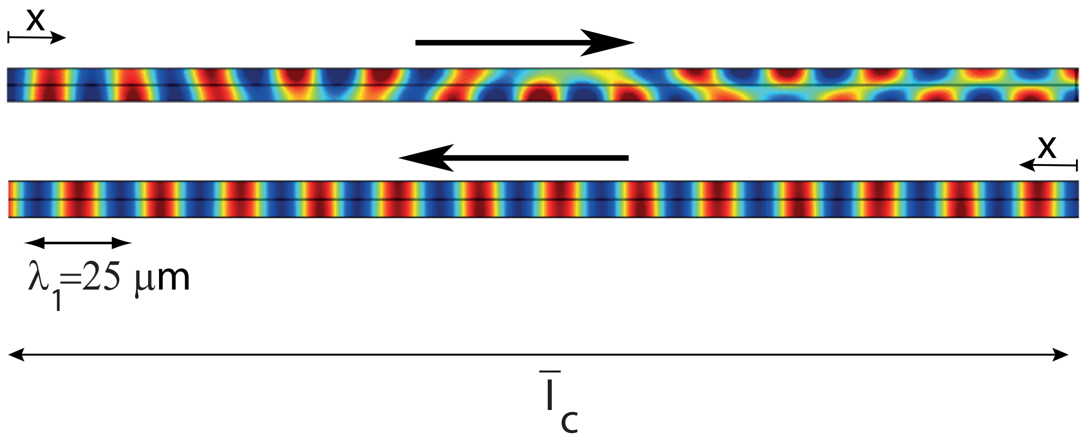

Figure 5.3: Numerical simulation of the wave propagation in forward and backward direction in a spatio-temporally modulated acoustic waveguide.

$c_{44} = c_{044} + \delta c \cos(\Omega t - K\,z)$, where c_{044} is the original elastic stiffness constant and δc is the modulation depth. This type of modulation will result in the same form of solution for $a_1(x)$ and $a_2(x)$. The resulting convergence length is driven as $l_c = \frac{\pi^2 c_{044}}{\delta c}\sqrt{\frac{2}{(\frac{\pi}{b})^2 + k_1 k_2}}$. Once again a larger modulation depth results in a smaller required conversion length. Also, for a forward propagating SH wave we observe full conversion of mode 1 to mode 2, while the SH wave traveling in the opposite direction passes thorough the waveguide unchanged (similar to Fig. 5.3, not shown here).

5.3 NEMS With Broken T Symmetry: Graphene Based Unidirectional Acoustic Transmission Lines

5.3.1 Introduction

Low dimensional materials such as graphene [174, 175, 176, 177], carbon nanotubes [178], boron nitride nanomaterials [179, 180, 181, 182], and atomically thin MoS_2 [183] have attracted great interest in recent years. The extraordinary electrical [184, 185], optical [186, 187], thermal [188, 189], and mechanical [190, 191] properties of graphene and analogous low-dimensional materials [192] make them promising candidates for practical applications in electronics, sensing, and energy storage devices.

Owing to their outstanding mechanical and electrical properties, these materials have been utilized as electromechanical oscillators in nanoscale memory cells and nanoelectromechanical switches [193, 194, 195, 196] and resonators [197, 198, 199]. The study of mechanical waves [200] and the ability to manipulate, control, and detect vibrational motion in such nanoelectromechanical systems (NEMS) [201, 202, 203, 204] provides unprecedented opportunities to employ them in fluidic [205], electronic [206], and optical networks [207]. NEMS based oscillators as mechanical sensors and actuators are also used in applications such as ultrasensitive force [208] and displacement detection [209, 210], scanning probe microscopy [211] and resonant mass sensing of chemical and biological species [212, 213] where an important functionality is to have one-way communication channels that transmit desired signals only in one direction.

Acoustic rectifiers and diodes [154, 155, 156, 157, 158] as well as one-way acoustic isolators [214] have been recently studied. The acoustic diode concept is based on a nonlinear frequency conversion mechanism [157, 159, 160]. Other studies have focused on nonreciprocity in acoustic circulators and acoustic metamaterials [215, 216]. More recently, the idea of one-way phonon isolation[214], motivated by optical equivalents [163, 164], was studied based on creating spatio-temporal modulation of mechanical properties. This leads to a one-way conversion between the guided modes, therefore, breaking the symmetry of wave propagation in a waveguide in forward and backward directions.

Here we study the idea of one-way signal isolation in low dimensional nanoelectromechanical oscillators where the symmetry of the system under time reversal transformation, also known as the T-symmetry, is broken. To explain the method, we consider a system of graphene nanoribbons (GNRs) on an elastic substrate and demonstrate that the symmetry of wave propagation may be broken by introducing spatial and temporal modulation of elastic properties of the system. We show, both analytically and numerically, that in one of the propagation directions conversion between the modes occurs, whereas in the other direction the signal is transmitted without any perturbations. We also discuss the extension of this method beyond graphene nanoribbons and mention its possible implementation for designing a phonon isolator in nanoelectromechanical oscillators.

5.3.2 Results

In Fig. 5.4(a), a double-layer graphene nanoribbon is shown. The system consists of two graphene nanoribbons with width b, each of which is perfectly adhered to an elastic substrate. We use the nonlocal elasticity theory to study wave propagation along the nanoribbons [217, 218]. In this model, shown in Fig. 5.5, each substrate is treated as a linear elastic medium with stiffness k_w [218], and the nanoribbons themselves interact via van der Waals forces that are also modeled as linear springs with stiffness c [218]. The governing equation for wave propagation in this system is driven from the nonlocal Euler-Bernoulli beam model [219, 220],

$$EI\frac{\partial^4 w_1}{\partial x^4} + \rho A\frac{\partial^2}{\partial t^2}(w_1 - (e_0 a)^2\frac{\partial^2 w_1}{\partial x^2}) = c(w_2 - w_1) - k_w w_1 \tag{5.3.1}$$

$$EI\frac{\partial^4 w_2}{\partial x^4} + \rho A\frac{\partial^2}{\partial t^2}(w_2 - (e_0 a)^2\frac{\partial^2 w_2}{\partial x^2}) = c(w_1 - w_2) - k_w w_2 \tag{5.3.2}$$

Here w_1 and w_2 are flexural displacements of nanoribbons 1 and 2 in the y direction, A is the cross sectional area of each GNR, ρ is the density, I is the moment of inertia, E is the Young's modulus, a is the C-C bond length and e_0 is a parameter representing nonlocal elastic effects in the GNR [218, 219]. Without loss of generality, we consider a simplified case with $e_0 a = 0$ and $k_w = c$ [218], and use the parameters obtained in Ref. [218]. The two governing equations (Eqs. 5.3.1 and 5.3.2) can then be written in the form $\mathbf{L}\overrightarrow{u} = 0$ where $\overrightarrow{u} = \begin{pmatrix} w_1 \\ w_2 \end{pmatrix}$, and $\mathbf{L}$ is a linear operator.

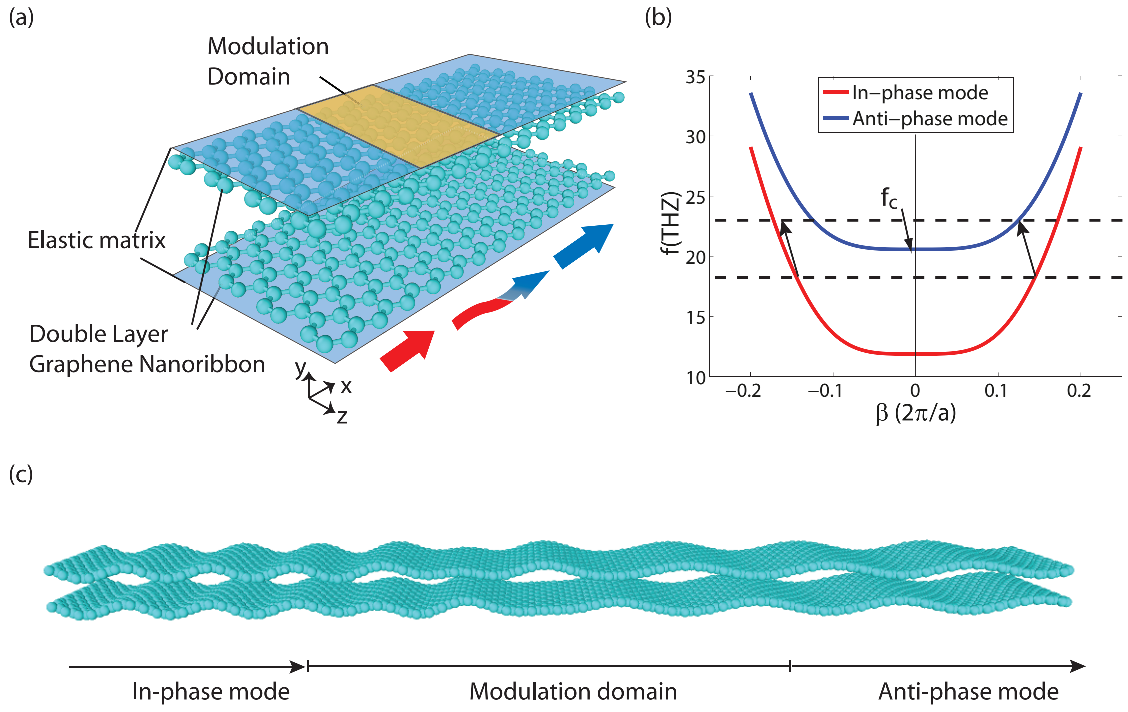

Figure 5.4: (a) A double-layer graphene nanoribbon on an elastic matrix. (b) Dispersion curve of the double-layer GNR obtained from Euler-Bernoulli beam model. The red and blue curves belong to the in-phase and anti-phase flexural modes respectively. (c) Schematic of in-phase to anti-phase mode conversion in a double-layer GNR system

Solutions of the form $\overrightarrow{u} = \begin{pmatrix} D_{w_1} \\ D_{w_2} \end{pmatrix} \exp i(\beta x - \omega t)$ are assumed, where D_{w_1} and D_{w_2} are the corresponding magnitudes of w_1 and w_2, and β and ω are the wavenumber and the angular frequency of the propagating wave. The corresponding solution results in two vibrational modes as shown in Fig. 5.4 (b). Mode 1 corresponds to the in-phase mode with $D_{w_1}^{(1)} = D_{w_2}^{(1)}$ and mode 2 corresponds to the anti-phase mode with $D_{w_1}^{(2)} = -D_{w_2}^{(2)}$. We note that below the cut-off frequency, f_c, only the in-phase branch exists, see Fig 5.4 (b). The value of the cut-off frequency depends on the nanoribbon and elastic matrix properties [218], $f_c = \frac{1}{2\pi}\sqrt{\frac{k_w+2c}{\rho A}}$, which in this system is around 20.5 THz for nanoribbons of 4nm width. [218].

Clearly, the dispersion curves plotted in the Fig.5.4 (b) are symmetric with respect to wavenumber β, implying that the wave propagation in such a waveguide is reciprocal, i.e. waves traveling in forward and backward directions have the same properties. In order to break this symmetry in the wave propagation phenomenon we follow the technique suggested in Refs. [214, 163]. In particular, we consider wave propagation with a spatio-temporally modulated elastic matrix. In this case we expect that for an appropriately chosen modulation, one-way conversion between the guided modes may be induced, i.e. interaction between the guided waves is possible in one propagation direction only.

We assume spatial-temporal modulation of the elastic matrix constant so that $k_w = k_{w0} + \delta k_w \cos(\Omega t - B\,x)$ where k_{w0} is the original stiffness constant and δk_w is the modulation depth. In order to maximize the coupling between modes, we modulate only the upper elastic matrix, as shown in Fig. 5.5. To solve the governing equations for the modulated system, we assume a general solution as the superposition of the guided modes:

$\overrightarrow{u}' = a_1(x) \begin{pmatrix} D_{w_1}^{(1)} \\ \\ D_{w_1}^{(1)} \end{pmatrix} \exp i(\beta_1\, x - \omega_1 t) + a_2(x) \begin{pmatrix} D_{w_1}^{(2)} \\ \\ -D_{w_1}^{(2)} \end{pmatrix} \exp i(\beta_2\, x - \omega_2 t)$, where $\beta_{1,2}$ and $\omega_{1,2}$ are the wavevectors and frequencies of in-phase and anti-phase modes, and $a_1(x)$ and $a_2(x)$ are their slowly varying spatial amplitudes. Next, using the standard techniques of the perturbation theory (see Appendix B), two ordinary differential equations are obtained.

$$\frac{d^2}{dx^2} \begin{pmatrix} a_1 \\ \\ a_2 \end{pmatrix} = \begin{pmatrix} -A_{11} & 0 \\ \\ 0 & -A_{22} \end{pmatrix} \begin{pmatrix} a_1 \\ \\ a_2 \end{pmatrix} \tag{5.3.3}$$

where $A_{11} = A_{22} = \frac{\delta k_w^2}{256(E\,I)^2 \beta_1^3 \beta_2^3} \exp i(\beta' x)$, and $\beta' = \beta_2 - \beta_1 - B$. Based on the incoming signal frequency ω_1 and the available modulation frequency Ω, a full mode conversion from mode 1 to mode 2 occurs when $\omega_2 = \omega_1 + \Omega$ and when the B parameter of the modulation is chosen such that $B = \beta_2 - \beta_1$ or $\beta' = 0$. The system shows one-way behavior because the modulation $k_w = k_{w0} + \delta k_w \cos(\Omega t - B\, x)$ does not convert the mode at $(-\beta_1, \omega_1)$ to any other modes. The resulting end point of the intended transition in the negative β region does not lie on the anti-phase branch of the dispersion curve (Fig. 5.4 (b)). This one-way behavior arises because the modulation breaks both time-reversal and spatial-inversion symmetry.

If we consider the propagation of the in-phase mode in the system, the initial conditions will be $a_1(0) = 1$ and $a_2(0) = 0$. The solution to equation 5.3.3 is then written as $a_1(x) = \cos(\xi x)$ and $a_2(x) = \sin(\xi x)$, where ξ is the conversion wavevector. As described in Fig. 5.6 (a), complete transition from in-phase to anti-phase mode is observed for the wave propagating in one direction (solid lines), while in the opposite direction the in-phase mode will not be influenced (dashed lines). The general solution of the governing

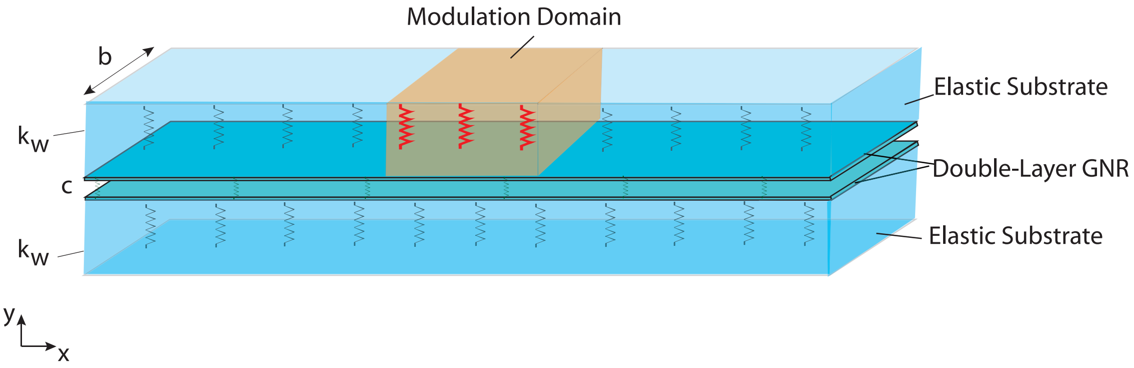

Figure 5.5: Schematic of continuum beam model for double-layer GNR on an elastic substrate with stiffness k_w. The shaded area represents the modulation domain.

equations is then $\cos(\xi x)\begin{pmatrix} D_{w_1}^{(1)} \\ D_{w_1}^{(1)} \end{pmatrix} \exp i(\beta_1 x - \omega_1 t) + \sin(\xi x)\begin{pmatrix} D_{w_1}^{(2)} \\ -D_{w_1}^{(2)} \end{pmatrix} \exp i(\beta_2 x - \omega_2 t)$ with $\xi = \frac{\delta k_w}{16 E I \sqrt{\beta_1^3 \beta_2^3}}$, and the corresponding conversion length of $l_c = \frac{\pi}{2\xi} = \frac{8\pi E I \sqrt{\beta_1^3 \beta_2^3}}{\delta k_w}$. As expected, the conversion length is inversely proportional to the modulation depth which means with a stronger modulation, the mode conversion requires a smaller modulation domain. To analyze the conversion length further, we investigate dependence on the modulation parameters. The intent of adding a modulation domain is to convert an incoming in-phase mode signal with frequency ω_1 and wavenumber β_1 to the anti-phase mode using the available modulation frequency Ω and tunable modulation wavenumber B. Therefore, we plot the dependence of the conversion length on wavenumber β_1 for different values of Ω. As shown in Fig. 5.6 (b), the required conversion length is larger for higher wavenumbers, as l_c varies proportional to $(\beta_1 \beta_2)^{\frac{3}{2}}$ with $\beta_2 = [(\rho A(\Omega + \sqrt{\frac{E I \beta_1^4 - k_w}{\rho A}})^2 + k_w + 2c)/(E I)]^{\frac{1}{4}}$. It is worth mentioning that the choice of Ω and β_1 is not arbitrary and should satisfy two criteria. First, the corresponding mode 1 frequency, ω_1, needs to

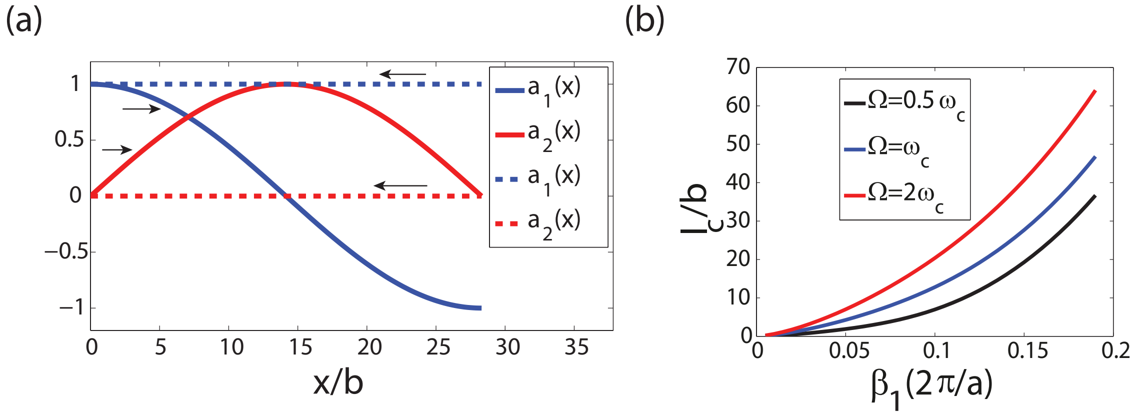

Figure 5.6: (a) Variation of mode amplitudes along the modulation domain. As shown by the arrows, the solid lines correspond to forward propagation with full conversion and the dashed lines correspond to backward propagation with no mode conversion. (b) Conversion length for different values of Ω as a function of wave number of in-phase mode.

be below the cut-off frequency. Second, the resulting frequency value $\Omega + \omega_1$ needs to lie on the dispersion curve of mode 2 in the forward propagation direction (positive β side) and lie on a band gap region in the backward propagation direction (negative β side) consistent with Fig. 5.4 (b) .

As an example, we choose a value slightly below the cut-off frequency to guarantee that at frequency ω_1 the system only supports the in-phase mode. For $\omega_1 = 0.95\omega_c$, $\Omega = 0.1\omega_c$ and $\delta k_w = 0.1k_w$, $l_c = 34.6\lambda_1$ where $\lambda_1 = \frac{2\pi}{\beta_1}$ is the wavelength of the corresponding mode 1 signal. Here we use normalized quantities in both the analytical and the numerical calculations. The corresponding frequency of mode 2 based on the dispersion curves will be $\omega_2 = 1.11\omega_1$. It is important to emphasize that the parameter values chosen are arbitrary and longer wavelength signals corresponding to smaller choices of ω_1 can also be used to observe the same isolation effect as long as the required conditions explained earlier are satisfied. Additionally, lower values of the modulation depth also result in a mode conversion, but require a longer modulation domain.

In order to confirm the analytical model, we used numerical simulations of the wave propagation and mode conversion in double-layer GNRs using finite difference time-domain (FDTD) method to solve the governing equations in the presence of spatio-temporal modulation. For this purpose, we choose a modulation domain with length l_c as predicted from the analytical model. The numerical simulation results are shown in Fig. 5.7. An incoming in-phase wave of wavelength λ_1 will be converted to an anti-phase wave of wavelength λ_2 after passing through the modulation domain. The Fourier spectra of both the incoming and outgoing signals are shown in Fig. 5.7 (b). From the FDTD simulations, the peak corresponding to the frequency of the outgoing signal (red curve) is around $\omega_2 = 1.08\omega_1$ which shows good agreement with the analytical method. The design of the system provides conversion of a signal of mode 1 to a signal of mode 2 in only one of the propagation directions. Therefore, in the opposite direction where no conversion between the two modes happens, we essentially observe a transmission ratio of 1 for the signal. In the other direction the signal of mode 1 is converted to mode 2 which implies a transmission ratio of close to zero. In fact, qualitatively, this type of isolation results in the following scattering matrix for the two ports: $\begin{pmatrix} 0 & 0 \\ 1 & 0 \end{pmatrix}$. More specifically, if we consider the Fourier spectrum of the outgoing signal in Fig. 5.7 (b), a transmission ratio of slightly above zero is observed for the forward propagation direction. However, this value of transmission ratio is influenced by the numerical errors within the framework of the

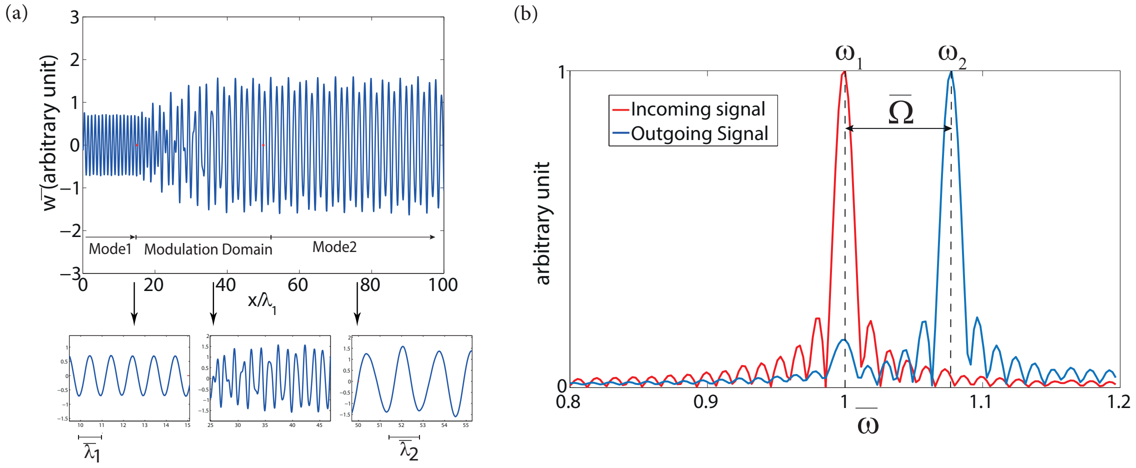

Figure 5.7: (a) FDTD simulation of in-phase to anti-phase mode conversion in double-layer graphene nanoribbons. x is scaled with respect to $\lambda_1 = \frac{2\pi}{\beta_1}$. (b) Fourier spectrum of the signal before and after the modulation domain. The horizontal axis is normalized with respect to the frequency of mode 1. The blue curve shows the Fourier transform of mode 1 which is peaked at a value of 1 corresponding to $\overline{\omega_1}$. The red curve is the Fourier transform of the signal after the modulation domain which shows a peak at $\overline{\omega_2} = 1.08$.

FDTD method and it is important to keep in mind that the analytical method suggests a transmission ratio of zero for this scenario.

Experimental realization of spatio-temporal modulation of elastic properties has been investigated recently. Spatial property modulation is possible through periodic arrangement of elastic material similar to the case of phononic crystals [166]. Temporal property modulation, although more difficult, is also possible in practice through applying electric or magnetic fields or mechanical strains in a periodic fashion [171, 172, 170]. In general, spatial modulations with nanometer scale periodicity provide suitable conditions for conversion between the two vibrational modes of double-layer GNRs. Furthermore, THz range frequencies are appropriate for temporal modulations to guarantee the unidirectional nature of such systems. Beyond double-layer GNRs, the aforementioned technique is also applicable to other systems. The key here is to have a system with two different branches of dispersion curve separated by a cut-off frequency. Using the same method, one-way mode conversion is achievable in systems such as single layer GNRs or double-wall carbon nanotubes where similar types of governing equations describe their behavior [221, 218, 222, 223, 224]. It is also important to mention that for very low wavelength limits the physics of the problem may differ from the predictions of continuum models and therefore atomistic level techniques such as molecular dynamics simulations [32] may be required for the analysis.

5.4 Conclusions

In conclusion, we have theoretically demonstrated that in a spatio-temporally modulated acoustic waveguide, the symmetry of mode conversion in forward and backward directions may be broken. We showed that similar to optical and electronic systems, and in the context of the acoustic-electromagnetic analogy [225, 226], phonon isolation may be achieved over a short distance. Such a principle may be implemented for on-chip acoustic devices. We also explored one-way acoustic signal isolation in graphene nanoribbons which can be extended to other low dimensional oscillators. The realization of a NEMS based signal isolators raises intriguing possibilities for a wide range of applications in scanning probe microscopes, force and displacement detection devices and chemical and biological sensors.

Chapter 6

Project Conclusions

6.1 Contributions

The following is a summary of the most important contributions made by this dissertation.

Nanocrystal superlattices are artificial solids formed by assembly of monodisperse building blocks that present surprising and transformable properties. A fundamental understanding of mechanical, phononic, and thermal properties of these materials is essential for optimizing and tuning their properties. The different length scales involved in the superlattice structures adds to the complexity of these systems which makes it challenging to use computational models to study such materials.

This dissertation investigated modeling techniques at different length scales for studying NCSLs. Coarse grained and atomistic models as well as effective medium theory were used to calculate the elastic moduli of NCSLs. It was concluded that existing coarse grained models require modification to account for strong attractive interactions between the ligands and a more detailed presentation of electrostatic forces. The atomistic models, on the other hand, present an accurate description of such interactions and predict the elastic moduli reasonably well.

Thermal properties of spherical gold NCSLs where calculated using equilibrium MD simulations based on validated empirical potentials. The resulting thermal conductivities show good agreements with the limited available experimental data. The MD simulations were also used to predict thermal conductivity of NCSLs with nanoparticles of different core sizes and surface ligand coverage. We also studied PbSe NCSLs which are promising materials for thermoelectric applications. Thermal conductivity of these octahedral nanocrystals were calculated using both empirical potentials and first principles calculations, and the resulting values based on empirical potentials were different from the first principles calculations by about 15%.

Phononic properties of NCSLs was also studied. Phononic band structure calculations showed that shape, size, and superlattice structures can be effectively used to tune the phononic band structure of NCSLs which is helpful in designing pass bands and stop bands for phonons.

Finally, the concept of one-way phonon isolation was presented and studied in acoustic waveguides and low dimensional materials. Using spatio-temporal modulation of mechanical properties, we showed that a one-way mode conversion for individual phonons is possible which can potentially be used to filter out specific phonon frequencies or acoustic waves for applications such as on-chip acoustic signal isolation or unidirectional acoustic transmission lines in NEMS devices.

6.2 Future Directions

Nanocrystal superlattices provide great opportunities for realizing and engineering interesting thermal and phononic behavior. One important extension of this work could include exploring the first principles based calculations for developing more accurate molecular simulations. Thermal properties of many interesting NCSLs of different shapes cannot be accurately modeled with typical empirical potentials. By calculating the accurate interatomic forces from first principles and quantum chemistry (which is useful for treating nanocrystal surface atoms), one can build a framework where the interactions between neighboring atoms of a nanocrystals are described by such accurate models. Subsequently, the use of molecular dynamics simulations with such accurate force fields will provide a powerful tool for studying thermal properties of a variety of NCSLs.

In a similar manner, the phonon dispersion curves of different NCSLs can be predicted more accurately and for higher frequencies using atomistic models with first principles based force fields. The main challenge for this purpose is the high computational cost of lattice dynamics calculations since the nanocrystal building blocks consist of few thousand or even tens of thousands of atoms which results in a complicated dispersion curve with tens of thousands of dispersion branches. Also from a fundamental scientific view point, such calculations could help answer the questions about range of validity and the applicability of continuum models more rigorously. The importance of experimental measurements of phonon dispersion curves of NCSLs should also be emphasized here since, at the current stage of research, no such experimental data exists for any type of nanocrystal superlattices.

Another interesting future direction is to study local elastic properties of NCSLs with a focus on the organic-inorganic interfaces. Theoretical calculations and experimental measurements of discrete and continuum elastic properties of NCSLs will provide more accurate data as inputs to atomistic and continuum models. Furthermore, the interface effects studied via atomistic models can provide important insight into the behavior of phonons at the interface which plays a significant role in phononic band structure and thermal property calculations for NCSLs.

One other potential future direction is to use NCSLs as the building blocks for creating phononic analogs of photonic behavior. The periodic structure of NCSLs and the combination of core and ligand components with different material properties makes them great candidates for realizing one-way phononic devices. The spatial property modulation that already exist in NCSL films is suitable for achieving phonon mode conversion. The more challenging task is the introduction of temporal modulations that will guarantee the one-way nature of phonon isolation.

Appendix A

Analytical Solution of SH Wave Equation In Presence of Spatio-Temporal Modulation

In this work, the analytical derivation of the solution to wave equation and the conversion length mentioned in section 5.2.2 is discussed. We begin by considering the SH wave equation in an unbounded plate waveguide:

$$\rho_0 \frac{\partial^2 u_z}{\partial t^2} = c_{44}[\frac{\partial^2 u_z}{\partial x^2} + \frac{\partial^2 u_z}{\partial y^2}] \tag{A.0.1}$$

The eigenfunctions corresponding to symmetric and antisymmetric guided modes of the waveguid can be written as $u_z^{(1)} \exp i(\omega_1 t - k_1 x)$ and $u_z^{(2)} \exp i(\omega_2 t - k_2 x)$ where $u_z^{(1)} = 1$ and $u_z^{(2)} = \sin(\frac{\pi y}{2b})$ are the mode profiles and b is the width of the waveguide. If we apply a density modulation of the form $\rho = \rho_0 + \delta\rho \cos(\Omega t - K\, x)$, the wave equation can be written as the following

$$[\rho_0+0.5\delta\rho(\exp(i(\Omega t-K\,x))+\exp(-i(\Omega t-K\,x)))]\frac{\partial^2 u_z}{\partial t^2}=c_{44}[\frac{\partial^2 u_z}{\partial x^2}+\frac{\partial^2 u_z}{\partial y^2}] \quad \text{(A.0.2)}$$

The general solution for Eq. A.0.2 can be written as a superposition of the guided modes: $u_z=0.5a_1(x)u_z^{(1)}\exp(i(\omega_1 t-k_1x))+0.5a_1(x)u_z^{(1)}\exp(-i(\omega_1 t-k_1x))+0.5a_2(x)u_z^{(2)}\exp(i(\omega_2 t-k_2x))+0.5a_2(x)u_z^{(2)}\exp(-i(\omega_2 t-k_2x))$ where $a_1(x)$ and $a_2(x)$ are the slowly varying spatial amplitudes of the two modes. From this point on, we will use the following abbreviations: $I\equiv i(\omega_1 t-k_1x)$, $II\equiv i(\omega_2 t-k_2x)$, and $\Delta\equiv i(\Omega t-K\,x)$. Substituting the general solution into Eq. A.0.2, we will have

$$\begin{gathered}[\rho_0+0.5\delta\rho\exp(\Delta)+0.5\delta\rho\exp(-\Delta)](-0.5\omega_1^2a_1u_z^{(1)}\exp(I)-0.5\omega_1^2a_1u_z^{(1)}\exp(-I)-0.5\omega_2^2a_2u_z^{(2)}\\ \exp(II)-0.5\omega_2^2a_2u_z^{(2)}\exp(-II))=c_{44}[0.5a_1\frac{\partial^2u_z^{(1)}}{\partial y^2}\exp(I)+0.5a_1\frac{\partial^2u_z^{(1)}}{\partial y^2}\exp(-I)\\ +0.5a_2\frac{\partial^2u_z^{(2)}}{\partial y^2}\exp(II)+0.5a_2\frac{\partial^2u_z^{(2)}}{\partial y^2}\exp(-II)+0.5\frac{\partial^2a_1}{\partial x^2}u_z^{(1)}\exp(I)+0.5\frac{\partial^2a_1}{\partial x^2}u_z^{(1)}\exp(-I)\\ -i\,k_1\frac{\partial a_1}{\partial x}u_z^{(1)}\exp(I)+i\,k_1\frac{\partial a_1}{\partial x}u_z^{(1)}\exp(-I)-0.5k_1^2a_1u_z^{(1)}\exp(I)-0.5k_1^2a_1u_z^{(1)}\exp(-I)\\ +0.5\frac{\partial^2a_2}{\partial x^2}u_z^{(2)}\exp(-II)-i\,k_2\frac{\partial a_2}{\partial x}u_z^{(2)}\exp(II)+i\,k_2\frac{\partial a_2}{\partial x}u_z^{(2)}\exp(-II)-0.5k_2^2a_2u_z^{(2)}\exp(II)\\ -0.5k_2^2a_2u_z^{(2)}\exp(-II)] \qquad \text{(A.0.3)}\end{gathered}$$

Since $u_z^{(1)}\exp(I)$, $u_z^{(1)}\exp(-I)$, $u_z^{(2)}\exp(II)$, and $u_z^{(2)}\exp(-II)$ are all solutions of the wave equation with density ρ_0, the above equation will be simplified to

$$\begin{gathered}0.25\delta\rho(\exp(\Delta)+\exp(-\Delta))[-\omega_1^2a_1u_z^{(1)}\exp(I)-\omega_1^2a_1u_z^{(1)}\exp(-I)-\omega_2^2a_2u_z^{(2)}\exp(II)\\ -\omega_2^2a_2u_z^{(2)}\exp(-II)]=c_{44}[0.5\frac{\partial^2a_1}{\partial x^2}u_z^{(1)}\exp(I)+0.5\frac{\partial^2a_1}{\partial x^2}u_z^{(1)}\exp(-I)\\ -i\,k_1\frac{\partial a_1}{\partial x}u_z^{(1)}\exp(I)+i\,k_1\frac{\partial a_1}{\partial x}u_z^{(1)}\exp(-I)+0.5\frac{\partial^2a_2}{\partial x^2}u_z^{(2)}\exp(II)+0.5\frac{\partial^2a_2}{\partial x^2}u_z^{(2)}\exp(-II)\end{gathered}$$

$$-i\,k_2\frac{\partial a_2}{\partial x}u_z^{(2)}\exp(II)+i\,k_2\frac{\partial a_2}{\partial x}u_z^{(2)}\exp(-II)] \tag{A.0.4}$$

By neglecting second order derivatives of slowly varying amplitudes a_1 and a_2 in the framework of perturbation theory, and by multiplying both sides of the above equation by ${u_z^{(1)}}^*\exp(-I)$ (which is the complex conjugate of the first solution to the wave equation), we will have

$$0.25\delta\rho(\exp(\Delta)+\exp(-\Delta))[-\omega_1^2a_1u_z^{(1)}{u_z^{(1)}}^*-\omega_1^2a_1u_z^{(1)}{u_z^{(1)}}^*\exp(-2I)-\omega_2^2a_2u_z^{(2)}{u_z^{(1)}}^*\exp(II-I)$$

$$-\omega_2^2a_2u_z^{(2)}{u_z^{(1)}}^*\exp(-II-I)]=c_{44}[-i\,k_1\frac{\partial a_1}{\partial x}u_z^{(1)}{u_z^{(1)}}^*+i\,k_1\frac{\partial a_1}{\partial x}u_z^{(1)}{u_z^{(1)}}^*\exp(-2I)$$

$$-i\,k_2\frac{\partial a_2}{\partial x}u_z^{(2)}{u_z^{(1)}}^*\exp(II-I)+i\,k_2\frac{\partial a_2}{\partial x}u_z^{(2)}{u_z^{(1)}}^*\exp(-II-I)] \tag{A.0.5}$$

Now if we integrate both sides of the above equation with respect to time over a long time period (0 to ∞), all the terms with nonzero exponents will vanish. If we have $-\Delta-I+II=0$, which is equivalent to $K=k_2-k_1$ and $\Omega=\omega_2-\omega_1$, only one term from each side of the above equation will survive. By integrating this equation over the width of the waveguide, we will have

$$0.25\delta\rho(-\omega_2^2a_2)\int_{-\frac{b}{2}}^{0}u_z^{(2)}{u_z^{(1)}}^*dy=c_{44}[-i\,k_1\frac{\partial a_1}{\partial x}\int_{-\frac{b}{2}}^{\frac{b}{2}}u_z^{(1)}{u_z^{(1)}}^*dy] \tag{A.0.6}$$

In this equation the left hand side integral is performed only over the modulation domain which is half of the waveguide width. Simplifying the above equation will result in the following ODE

$$\frac{\partial a_1}{\partial x}=-\frac{0.25\delta\rho\omega_2^2a_2\int_{-\frac{b}{2}}^{0}u_z^{(2)}{u_z^{(1)}}^*dy}{i\,k_1c_{44}\int_{-\frac{b}{2}}^{\frac{b}{2}}u_z^{(1)}{u_z^{(1)}}^*dy} \tag{A.0.7}$$

Repeating the same steps and multiplying Eq. A.0.4 by by $u_z^{(2)^*}\exp(-II)$, we will get the following ODE

$$\frac{\partial a_2}{\partial x} = -\frac{0.25\delta\rho\omega_1^2 a_1 \int\limits_{-\frac{b}{2}}^{0} u_z^{(1)} u_z^{(2)^*} dy}{i\, k_2 c_{44} \int\limits_{-\frac{b}{2}}^{\frac{b}{2}} u_z^{(2)} u_z^{(2)^*} dy} \tag{A.0.8}$$

The last two ODE's could be written as $\frac{\partial a_p}{\partial x} = \frac{A_{pq}}{i} a_q$ where $\{p, q\}$ represents either $\{1, 2\}$ or $\{2, 1\}$, and

$$A_{pq} = \frac{\delta\rho\omega_q^2 \int\limits_{-\frac{b}{2}}^{0} u_z^{(q)} u_z^{(p)^*} dy}{4c_{44} k_p \int\limits_{-\frac{b}{2}}^{\frac{b}{2}} u_z^{(p)} u_z^{(p)^*} dy} \tag{A.0.9}$$

Differentiating the two resulting ODE's one more time will result in the following second order ODE's

$$\frac{d^2}{dx^2}\begin{pmatrix} a_1 \\ \\ a_2 \end{pmatrix} = \begin{pmatrix} -A_{12}A_{21} & 0 \\ \\ 0 & -A_{21}A_{12} \end{pmatrix}\begin{pmatrix} a_1 \\ \\ a_2 \end{pmatrix} \tag{A.0.10}$$

These equations will subsequently result in periodic solutions with a conversion length equal to $l_c = \frac{\pi}{2\sqrt{A_{12}A_{21}}}$ which is equivalent to the resulting conversion length shown in section 5.2.2.

Appendix B

Analytical Solution of Graphene Nanoribbon Wave Equations

In the case of graphene nanoribbons, a similar method can be used to solve the Euler-Bernoulli equations. Eqs. 5.3.1 and 5.3.2 can be rewritten as $\mathbf{L}\overrightarrow{u} = 0$ where $\overrightarrow{u} = \begin{pmatrix} w_1 \\ w_2 \end{pmatrix}$, and $\mathbf{L}$ is a linear operator,

$$L = \begin{pmatrix} E\,I\frac{\partial^4}{\partial x^4} + \rho A\frac{\partial^2}{\partial t^2} - c - k_{w0} & c \\ c & E\,I\frac{\partial^4}{\partial x^4} + \rho A\frac{\partial^2}{\partial t^2} - c - k_{w0} \end{pmatrix} \tag{B.0.1}$$

Assuming a solution of the form $\overrightarrow{u} = \begin{pmatrix} D_{w_1} \\ D_{w_2} \end{pmatrix} \exp i(\beta x - \omega t)$ will result in the following equation for D_{w_1} and D_{w_2}

$$\begin{pmatrix} EI\beta^4 - \rho A\omega^2 - c - k_{w0} & c \\ c & EI\beta^4 - \rho A\omega^2 - c - k_{w0} \end{pmatrix} \begin{pmatrix} D_{w_1} \\ D_{w_2} \end{pmatrix} = \begin{pmatrix} 0 \\ 0 \end{pmatrix} \tag{B.0.2}$$

The nontrivial solution of the above equation happens when the 2 by 2 matrix is singular which results in the following dispersion relations

$$\omega_1^2 = \frac{EI\beta_1^4 - k_{w0}}{\rho A} \tag{B.0.3}$$

$$\omega_2^2 = \frac{EI\beta_2^4 - k_{w0} - 2c}{\rho A} \tag{B.0.4}$$

Where mode 1 corresponds to the in-phase mode with $D_{w_1}^{(1)} = D_{w_2}^{(1)}$ and mode 2 corresponds to the anti-phase mode with $D_{w_1}^{(2)} = -D_{w_2}^{(2)}$.

In the presence of the spatial-temporal modulation $k_w = k_{w0} + \delta k_w \cos(\Omega t - Bx)$, a general solution as the superposition of the guided modes is assumed:

$$\overrightarrow{u}' = a_1(x) \begin{pmatrix} D_{w_1}^{(1)} \\ D_{w_1}^{(1)} \end{pmatrix} \exp i(\beta_1 x - \omega_1 t) + a_2(x) \begin{pmatrix} D_{w_1}^{(2)} \\ -D_{w_1}^{(2)} \end{pmatrix} \exp i(\beta_2 x - \omega_2 t) \tag{B.0.5}$$

Using this general solution and plugging it in the Euler-Bernoulli equations with modulated k_w, we can follow the same steps discussed in Appendix A to get to the following ordinary differential equations

$$\frac{\partial a_1}{\partial x} = \frac{i\delta k_w}{16EI\beta_1^3} a_2 \tag{B.0.6}$$

$$\frac{\partial a_2}{\partial x} = \frac{i\delta k_w}{16EI\beta_2^3} a_1 \tag{B.0.7}$$

Differentiating the above equations one more time will result in Eq. 5.3.3.

Bibliography

[1] F. Ercolessi, W. Andreoni, and E. Tosatti. Melting of small gold particles: Mechanism and size effects. *Phys. Rev. Lett.*, 66:911, 1991.

[2] R. Ferrando, J. Jellinek, and R. L. Johnston. Nanoalloys: From Theory to Applications of Alloy Clusters and Nanoparticles. *Chem. Rev.*, 108:845, 2008.

[3] E. V. Shevchenko, D. V. Talapin, N. A. Kotov, S. O'Brien, and C. B. Murray. Structural diversity in binary nanoparticle superlattices. *Nature*, 439:55–59, 2006.

[4] C. B. Murray, C. R. Kagan, and M. G. Bawendi. Self-Organization of CdSe Nanocrystallites into Three-Dimensional Quantum Dot Superlattices. *Science*, 270:1335–1338, 1995.

[5] X. Ye, J. Chen, M. Engel, J. A. Millan, W. Li, L. Qi, G. Xing, J. E. Collins, C. R. Kagan, J. Li, S. C. Glotzer, and C. B. Murray. Competition of shape and interaction patchiness for self-assembling nanoplates. *Nat. Chem.*, 5:446, 2013.

[6] E. V. Shevchenko, D. V. Talapin, C. B. Murray, and S. O'Brien. Structural Characterization of Self-Assembled Multifunctional Binary Nanoparticle Superlattices. *J. Am. Chem. Soc.*, 128:3620–3637, 2006.

[7] T. Paik and C. B. Murray. Shape-Directed Binary Assembly of Anisotropic Nanoplates: A Nanocrystal Puzzle with Shape-Complementary Building Blocks. *Nano Lett.*, 13:2952, 2013.

[8] S. J. Oh, N. E. Berry, J. H. Choi, E. A. Gaulding, H. Lin, T. Paik, B. T. Diroll, S. Muramoto, C. B. Murray, and C. R. Kagan. Designing High-Performance PbS and PbSe nanocrystal electronic devices through stepwise, post-synthesis, colloidal atomic layer deposition. *Nano Lett.*, 14:1559, 2014.

[9] H. Chan, A. Demortiere, L. Vukovic, P. Kral, and C. Petit. Colloidal Nanocube Supercrystals Stabilized by Multipolar Coulombic Coupling. *ACS Nano*, 6:4203, 2012.

[10] D. V. Talapin, E. V. Shevchenko, C. B. Murray, A. V. Titov, and P. Kral. Dipole-Dipole Interactions in Nanoparticle Superlattices. *Nano Lett.*, 7:1213–1219, 2007.

[11] M. D. Eldridge, P. A. Madden, and D. Frenkel. Entropy driven formation of a superlattice in a hard sphere binary mixture. *Nature*, 365:37, 1993.

[12] W.-L. Ong, S. M. Rupich, D. V. Talapin, A. J. H. McGaughey, and J. A. Malen. Surface chemistry mediates thermal transport in three-dimensional nanocrystal arrays. *Nat. Mater.*, 12:410–415, 2013.

[13] W.-L. Ong, S. Majumdar, J. A. Malen, and A. J. H. McGaughey. Coupling of Organic and Inorganic Vibrational States and Their Thermal Transport in Nanocrystal Arrays. *J. Phys. Chem. C*, 118:7288, 2014.

[14] D. V. Talapin, J.-S. Lee, M. V. Kovalenko, and E. V. Shevchenko. Prospects of Colloidal Nanocrystals for Electronic and Optoelectronic Applications. *Chem. Rev.*, 110:389, 2010.

[15] M. G. Panthani and B. A. Korgel. Nanocrystals for Electronics. *Annu. Rev. Chem. Biomol. Eng.*, 3:287, 2012.

[16] M. E. Turk, J.-H. Choi, S. J. Oh, A. T. Fafarman, B. T. Diroll, C. B. Murray, C. R. Kagan, and J. M. Kikkawa. Gate-Induced Carrier Delocalization in Quantum Dot Field Effect Transistors. *Nano Lett.*, 14:5948, 2014.

[17] W.-K. Koh, S. R. Saudari, A. T. Fafarman, C. R. Kagan, and C. B. Murray. Thiocyanate-Capped PbS Nanocubes: Ambipolar Transport Enables Quantum Dot Based Circuits on a Flexible Substrate. *Nano Lett.*, 11:4764, 2011.

[18] D. K. Kim, Y. Lai, B. T. Diroll, C. B. Murray, and C. R. Kagan. Flexible and low-voltage integrated circuits constructed from high-performance nanocrystal transistors. *Nat. Commun.*, 3:1216, 2012.

[19] Y. Shirasaki, G. J. Supran, M. G. Bawendi, and V. Bulovic. Emergence of colloidal quantum-dot light-emitting technologies. *Nat. Photon.*, 7:13, 2013.

[20] J. Y. Kim, O. Voznyy, D. Zhitomirsky, and E. H. Sargent. 25th Anniversary Article: Colloidal Quantum Dot Materials and Devices: A Quarter-Century of Advances. *Adv. Mater.*, 25:4986, 2013.

[21] I. J. Kramer and E. H. Sargent. The Architecture of Colloidal Quantum Dot Solar Cells: Materials to Devices. *Chem. Rev.*, 114:863, 2014.

[22] R. Y. Wang, J. P. Feser, J.-S. Lee, D. V. Talapin, R. Segalman, and A. Majumdar. Enhanced Thermopower in PbSe Nanocrystal Quantum Dot Superlattices. *Nano Lett.*, 8:2283, 2008.

[23] T. C. Harman, P. J. Taylor, M. P. Walsh, and B. E. LaForge. Quantum Dot Superlattice Thermoelectric Materials and Devices. *Science*, 297:2229, 2002.

[24] G. G. Yadav, J. A. Susoreny, G. Zhang, H. Yang, and Y. Wu. Nanostructure-based thermoelectric conversion: an insight into the feasibility and sustainability for large-scale deployment. *Nanoscale*, 3:3555–3562, 2011.

[25] O. L. Lazarenkova and A. A. Balandin. Electron and phonon energy spectra in a three-dimensional regimented quantum dot superlattice. *Phys. Rev. B*, 66:245319, 2002.

[26] H. F. Schaefer III. *Quantum Chemistry: The Development of Ab Initio Methods in Molecular Electronic Structure Theory.* Dover, 2004.

[27] P. Hohenberg and W. Kohn. Inhomogeneous Electron Gas. *Phys. Rev.*, 136:B864, 1964.

[28] W. Kohn and L. J. Sham. Self-Consistent Equations Including Exchange and Correlation Effects. *Phys. Rev.*, 140:A1133, 1965.

[29] D. J. Griffiths. *Introduction to Quantum Mechanics.* Pearson Prentice Hall, 2004.

[30] S. Baroni, P. Giannozzi, and A. Testa. Green's-function approach to linear response in solids. *Phys. Rev. Lett.*, 58:1861, 1987.

[31] P. Giannozzi et al. Quantum espresso: a modular and open-source software project for quantum simulations of materials. *Journal of Physics: Condensed Matter*, 21(39):395502, 2009.

[32] M. P. Allen and D. J. Tildesley. *Computer Simulation of Liquids*. Oxford Science Publication, 2001.

[33] T. V. M. Ndoro, E. Voyiatzis, A. Ghanbari, D. N. Theodorou, M. C. Bohm, and F. Muller-Plathe. Interface of Grafted and Ungrafted Silica Nanoparticles with a Polystyrene Matrix: Atomistic Molecular Dynamics Simulations. *Macromolecules*, 44:2316, 2011.

[34] B. Song, H. Yuan, C. J. Jameson, and S. Murada. Role of surface ligands in nanoparticle permeation through a model membrane: a coarse-grained molecular dynamics simulations study. *Molecular Physics*, 110:2181, 2012.

[35] P. Podsiadlo, G. Krylova, B. Lee, K. Critchley, D. Gosztola, D. V. Talapin, P. D. Ashby, and E. V. Shevchenko. The Role of Order, Nanocrystal Size, and Capping Ligands in the Collective Mechanical Response of Three-Dimensional Nanocrystal Solids. *J. Am. Chem. Soc.*, 132:8953–8960, 2010.

[36] J. Yin, M. Retsen, J.-H. Lee, E. L. Thomas, and M. C. Boyce. Mechanics of Nanoindentation on a Monolayer of Colloidal Hollow Nanoparticles. *Langmuir*, 27:10492–10500, 2011.

[37] E. Tam, P. Podsiadlo, E. Shevchenco, D. F. Ogletree, M.-P. Delplaneke-Ogletree, and P. D. Ashby. Mechanics Properties of Face-Centered Cubic Supercrystals of Nanocrystals. *Nano Lett.*, 10:2363–2367, 2010.

[38] H. Marquardt, A. Gleason, K. Marquardt, L. Miyagi S. Speziale, G. Neusser, H. Wenk, and R. Jeanloz. Elastic properties of mgo nanocrystals and grain boundaries at high pressures by brillouin scattering. *Phys. Rev. B*, 84:064131, 2011.

[39] U. Landman and W. D. Luedtke. Small is different: energetic, structural, thermal, and mechanical properties of passivated nanocluster assemblies uzi landman. *Faraday Discuss. R. Soc. Chem.*, 125:1–22, 2004.

[40] A. Striolo, J. Ward, , J. M. Prausnitz, W. J. Parak, D. Zanchet, D. Gerion, D. Milliron, and A. P. Alivisatos. Molecular weight, osmotic second virial coefficient, and extinction coefficient of colloidal cdse nanocrystals. *J. Phys. Chem. B*, 106:5500–5505, 2002.

[41] A. E. Saunders and B. A. Korgel. Second virial coefficient measurements of dilute gold nanocrystal dispersions using small-angle x-ray scattering. *J. Phys. Chem. B*, 108:16732–16738, 2004.

[42] E. Rabani. Structure and electrostatic properties of passivated CdSe nanocrystals. *J. Chem. Phys.*, 115:1493–1497, 2001.

[43] P. Schapotschnikow, B. Hommersom, and T. J. H. Vlugt. Adsorption and Binding of Ligands to CdSe Nanocrystals. *J. Phys. Chem.*, 113:12690–12698, 2009.

[44] E. Rabani. An interatomic pair potential for cadmium selenide. *J. Chem. Phys.*, 116:258–262, 2002.

[45] N. Lubna, G. Kamath, J. J. Potoff, N. Rai, , and J. I. Siepman. Transferable Potentials for Phase Equilibria. 8. United-Atom Description for Thiols, Sulfides, Disulfides, and Thiophene. *J. Phys. Chem. B*, 109:24100–24107, 2005.

[46] I. Alber, J. L. Bassani, M. Khantha, V. Vitek, and G. Wang. Grain boundaries as heterogeneous systems: atomic and continuum elastic properties. *Phil. Trans. R. Soc. Lond. A*, 339:555–586, 1992.

[47] V. Vitek and T. Egami. Atomic Level Stresses in Solids and Liquids. *Physica Status Solidi*, 144:145–156, 1987.

[48] S. Plimpton. Fast Parallel Algorithms for Short-Range Molecular Dynamics. *J. Comput. Phys.*, 117:1–19, 1995.

[49] E. F. Pettersen, T.D. Goddard, C. C. Huang, G. S. Couch, D. M. Greenblatt, E. C. Meng, and T. E. Ferrin. UCSF Chimera-a visualization system for exploratory research and analysis. *J. Comput. Chem.*, 25:1605–1612, 2004.

[50] H. C. Hamaker. The london-van der waals attraction between spherical particles. *Physica 4*, 10:1058–1072, 1937.

[51] J. N. Israelachvili. *Intermolecular and Surface Forces*. Elsevier, 2009.

[52] P. G. de Gennes. Polymer Solutions near an Interface. *Macromolecules*, 14:1637, 1981.

[53] B. A. Korgel, S. Fullam, S. Connolly, , and D. Fitzmaurice. Assembly and self-organization of silver nanocrystal superlattices: Ordered soft spheres. *J. Phys. Chem. B*, 102:8379–8388, 1998.

[54] G. Ge and L. Brus. Evidence for Spinodal Phase Separation in Two-Dimensional Nanocrystal Self-Assembly. *Phys. Chem. B.*, 104:9573–9575, 2000.

[55] T. C. Choy. *Effective medium theory.* Oxford University Press, 1999.

[56] M. Levy, H. E. Bass, and R. R. Stern. *Handbook of Elastic Properties of Solids, Liquids, and Gases.* Academic Press, 2001.

[57] Z. Hashin. Analysis of Composit Materials-A Survey. *J. Appl. Mech.*, 50:481–505, 1983.

[58] N. Phan-Thien. Effective Lame's moduli of cubic arrays of elastic spheres embedded in an elastic matrix. *J. Appl. Mech. Phys.*, 34:387–397, 1983.

[59] R. G. C. Arridge. The thermal expansion and bulk modullus of composites consisting of arrays of spherical particles in a matrix, with body-or face-centered cubic symmetry. *Proc. R. Soc. Lond. A*, 438:291–310, 1992.

[60] R. C. McPhedran and G. W. Milton. Bound and Exact Theories for Transport Properties of Inhomogenous Media. *Appl. Phys. A*, 26:207–220, 1981.

[61] J.-G. Guo and Y.-P. Zhao. The surface and size-dependent elastic moduli of nanostructures. *Surface Review and Letters*, 14:667–670, 2007.

[62] H. D. Espinosa, R. A. Bernal, and M. Minary-Jolan. A review of mechanical and electromechanical properties of piezoelectric nanowires. *Adv. Mater.*, 24:4656–4675, 2012.

[63] R. E. Miller and V. B. Shenoy. Size-dependent elastic properties of nanosized structural elements. *Nanotechnology*, 11:139–147, 2000.

[64] Z. Chen, J. Moore, G. Radtke, H. Sirringhaus, and S. O'Brien. Binary nanoparticle superlattices in the semiconductor-semiconductor system: Cdte and cdse. *J. Am. Chem. Soc.*, 129:15702–15709, 2007.

[65] M. Shamsa, W. Liu, and A. A. Balandin. Phonon-hopping thermal conduction in quantum dot superlattices. *Appl. Phys. Lett.*, 87:202105, 2005.

[66] A. Khitun, A. A. Balandin, J. L. Liu, and K. L. Wang. In-plane lattice thermal conductivity of a quantum-dot superlattice. *J. Appl. Phys.*, 88:696, 2000.

[67] J. L. Liu, A. Khitun, K. L. Wang, W. L. Liu, G. Chen, Q. H. Xie, and S. G. Thomas. Cross-plane thermal conductivity of self-assembled Ge quantum dot superlattices. *Phys. Rev. B*, 67:165333, 2003.

[68] T. Luo and J. R. Lloyd. Equilibrium Molecular Dynamics Study of Lattice Thermal Conductivity/Conductance of Au-SAM-Au Junctions. *J. Heat Transfer*, 132:032401, 2010.

[69] R. Kubo. Statistical-Mechanical Theory of Irreversible Processes. I. General Theory and Simple Applications to Magnetic and Conduction Problems. *J. Phys. Soc. Jpn.*, 12:570, 1957.

[70] D. A. McQuarrie. *Statistical Mechanics*. University Science Books, 2000.

[71] J. Che, T. Cagin, W. Deng, and W. A. Goddard. Thermal conductivity of diamond and related materials from molecular dynamics simulations. *J. Chem. Phys.*, 113:6888, 2000.

[72] J. Dong, O. F. Sankey, and C. W. Myles. Theoretical study of lattice thermal conductivity in Ge framework semiconductors. *Phys. Rev. Lett.*, 86:2361, 2001.

[73] A. J. H. McGaughey and M. Kaviany. Thermal conductivity decomposition and analysis using molecular dynamics simulations. *Int. J. Heat Mass Transfer*, 47:1799, 2004.

[74] C. L. Yaws. *Handbook of Thermal Conductivity*, volume 2. Gulf Publishing Company, 1995.

[75] S. Volz and G. Chen. Lattice dynamic simulation of silicon thermal conductivity. *Physica B*, 263:709, 1999.

[76] P. Chantrenne and J. Barrat. Finite Size Effects in Determination of Thermal Conductivities: Comparing Molecular Dynamics Results With Simple Models. *J. Heat Transfer*, 126:577, 2004.

[77] M. B. Zanjani and J. R. Lukes. Size dependent elastic moduli of CdSe nanocrystal superlattices predicted from atomistic and coarse grained models. *J. Chem. Phys.*, page 139, 2013.

[78] S. Shen, A. Henry, J. Tong, R. Zheng, and G. Chen. Polyethylene nanofibres with very high thermal conductivities. *Nat. Nanotechnol.*, 5:251, 2010.

[79] N. J. Hardy, M. D. Hanwell, and T. H. Richardson. Temperature effects on the electrical conductivity of thiol encapsulated gold nanoparticle thin film. *J. Mater. Sci.*, 18:943, 2007.

[80] P. Schapotschnikow, M. A. van Huis, H. W. Zandbergen, D. Vanmaekelbergh, and T. J. H. Vlugt. Morphological Transformations and Fusion of PbSe Nanocrystals Studied Using Atomistic Simulations. *Nano Lett.*, 10:3966, 2010.

[81] R. Prasher. Ultralow thermal conductivity of a packed bed of crystalline nanoparticles: A theoretical study. *Phys. Rev. B*, 74:165413, 2006.

[82] C. V. Madhusudana. *Thermal Contact Conductance.* Springer, 1995.

[83] S. Jennings. The mean free path in air. *Journal of Aerosol Science*, 19:159, 1988.

[84] S. Basu, Z. M. Zhang, and C. J. Fu. Review of near-field thermal radiation and its application to energy conversion. *Int. J. Energy Res.*, 33:1203, 2009.

[85] A. Narayanaswamy and G. Chen. Thermal near-field radiative transfer between two spheres. *Phys. Rev. B*, 77:075125, 2008.

[86] D. Polder and M. Van Hove. Theory of Radiative Heat Transfer between Closely Spaced Bodies. *Phys. Rev. B*, 4:3303, 1971.

[87] A. I. Volokitin and B. N. J. Persson. Resonant photon tunneling enhancement of the radiative heat transfer. *Phys. Rev. B*, 69:045417, 2004.

[88] G. Chen. Phonon Wave Heat Conduction in Thin Films and Superlattices. *J. Heat Transfer*, 121:945, 1999.

[89] Z. Tian, J. Garg, K. Esfarjani, T. Shiga, J. Shiomi, and G. Chen. Phonon conduction in PbSe, PbTe, and $\mathrm{PbTe}_{1-x}\mathrm{Se}_x$ from first-principles calculations. *Phys. Rev. B*, 85:184303, 2012.

[90] M. T. Dove. *Introduction to Lattice Dynamics.* Cambridge University Press, 1993.

[91] N. Zen, T. A. Puurtinen, T. J. Isotalo, S. Chaudhuri, and I. J. Maasilta. Engineering thermal conductance using a two-dimensional phononic crystal. *Nat. Commun.*, 5:3435, 2014.

[92] W. Cheng, J. wang, U. Jonas, G. Fytas, and N. Stefanou. Observation and tuning of hypersonic bandgaps in colloidal crystals. *Nat. Mat.*, 5:830, 2006.

[93] M. I. Hussein, M. J. Leamy, and M. Ruzzene. Dynamics of phononic materials and structures: Historical origins, recent progress and future outlook. *Appl. Mech. Rev.*, 66:040802, 2014.

[94] M. Maldovan. Narrow Low-Frequency Spectrum and Heat Management by Thermocrystals. *Phys. Rev. Lett.*, 110:025902, 2013.

[95] B. L. Davis and M. I. Hussein. Nanophononic Metamaterial: Thermal Conductivity Reduction by Local Resonance. *Phys. Rev. Lett.*, 112:055505, 2014.

[96] L. Wang and B. Li. Phononics gets hot. *Phys. World*, 21:27, 2008.

[97] J. Tang, H.-T. Wang, D. H. Lee, M. Fardy, Z. Huo, T. P. Russell, and P. Yang. Holey Silicon as an Efficient Thermoelectric Material. *Nano Lett.*, 10:4279, 2010.

[98] J.-K. Yu, S. Mitrovic, D. Tham, J. Varghese, and J. R. Heath. Reduction of thermal conductivity in phononic nanomesh structures. *Nat. Nanotech.*, 5:718, 2010.

[99] P. E. Hopkins, C. M. Reinke, M. F. Su, R. H. Olsson, E. A. Shaner, Z. C. Leseman, J. R. Serrano, L. M. Phinney, and I. El-Kady. Reduction in the Thermal Conductivity of Single Crystalline Silicon by Phononic Crystal Patterning. *Nano Lett.*, 11:107, 2011.

[100] T. Gorishnyy, C. K. Ullal, M. Maldovan, G. Fytas, and E. L. Thomas. Hypersonic Phononic Crystals. *Phys. Rev. Lett.*, 94:115501, 2005.

[101] E. L. Thomas, T. Gorishnyy, and M. Maldovan. Colloidal crystals go hypersonic. *Nat. Mat.*, 5:773, 2006.

[102] S. Mohammadi, A.A. Eftekhar, A. Khelif, H. Moubchir, R. Westafer, W.D. Hunt, and A. Adibi. Complete phononic bandgaps and bandgap maps in two-dimensional silicon phononic crystal plates. *Electon. Lett.*, 43:898, 2007.

[103] M. I. Hussein and M. J. Frazier. Band structure of phononic crystals with general damping. *J. Appl. Phys.*, 108:093506, 2010.

[104] M. S. Kushwaha, P. Halevi, L. Dobrzynski, and B. Djafari-Rouhani. Acoustic band structure of periodic elastic composites. *Phys. Rev. Lett.*, 71:2022, 1993.

[105] M. Maldovan. Sound and heat revolutions in phononics. *Nature*, 503:209–217, 2013.

[106] J. O. Vasseur, P. A. Deymier, B. Chenni, B. Djafari-Rouhani, L. Dobrzynski, and D. Prevost. Experimental and Theoretical Evidence for the Existence of Absolute

Acoustic Band Gaps in Two-Dimensional Solid Phononic Crystals. *Phys. Rev. Lett.*, 86:3012, 2001.

[107] M.-H. Lu, L. Feng, and Y.-F. Chen. Phononic crystals and acoustic metamaterials. *Materials Today*, 12:34, 2009.

[108] A. Khelif, A. Choujaa, B. Djafari-Rouhani, M. Wilm, S. Ballandras, and V. Laude. Trapping and guiding of acoustic waves by defect modes in a full-band-gap ultrasonic crystal. *Phys. Rev. B*, 68:214301, 2003.

[109] A. Khelif, A. Choujaa, S. Benchabane, B. Djafari-Rouhani, and V. Laude. Guiding and bending of acoustic waves in highly confined phononic crystal waveguides. *Appl. Phys. Lett.*, 84:4400, 2004.

[110] J.-H. Sun and T.-T. Wu. Analyses of mode coupling in joined parallel phononic crystal waveguides. *Phys. Rev. B*, 71:174303, 2005.

[111] M. M. Sigalas. Defect states of acoustic waves in a two-dimensional lattice of solid cylinders. *J. Appl. Phys.*, 84:3026, 1998.

[112] S. Yang, J. H. Page, Z. Liu, M. L. Cowan, C. T. Chan, and P. Sheng. Focusing of Sound in a 3D Phononic Crystal. *Phys. Rev. Lett.*, 93:024301, 2004.

[113] M. S. Kushwaha. Stop-bands for periodic metallic rods: Sculptures that can filter the noise. *Applied Physics Letters*, 70:3218–3220, 1997.

[114] D. Yu, J. Wen, H. Zhao, Y. Liu, and X. Wen. Vibration reduction by using the idea of phononic crystals in a pipe-conveying fluid. *J. Sound Vib.*, 318:193, 2008.

[115] R. H. Olsson III and I. El-Kady. Microfabricated phononic crystal devices and applications. *Meas. Sci. Technol.*, 20:012002, 2009.

[116] M. Eichenfield, J. Chan, R. M. Camacho, K. J. Vahala, and O. Painter. Microfabricated phononic crystal devices and applications. *Nature (London)*, 462:78, 2009.

[117] M. Stimulak and M. Ravnik. Tunable photonic crystals with partial bandgaps from blue phase colloidal crystals and dielectric-doped blue phases. *Soft Matt.*, 10:6339, 2014.

[118] J. Valenta, J. Linnros, R. Juhasz, J.-L. Rehspringer, F. Huber, C. Hirlimann, S. Cheylan, and R. G. Elliman. Photonic band-gap effects on photoluminescence of silicon nanocrystals embedded in artificial opals. *J. Appl. Phys.*, 93:4471, 2003.

[119] C. Liao, H. Zhang, L. Tang, Z. Zhou, Y. Lv, C.and Cui, and J. Zhang. Nonlinear optical response of semiconductor-nanocrystals-embedded photonic band gap structure. *Appl. Phys. Lett.*, 104:171901, 2014.

[120] H. Xia, L. Zhang, Q.-D. Chen, L. Guo, H.-H. Fang, X.-B. Li, J.-F. Song, X.-R. Huang, and H.-B. Sun. Band-Gap-Controllable Photonic Crystals Consisting of Magnetic Nanocrystal Clusters in a Solidified Polymer Matrix. *The Journal of Physical Chemistry C*, 113:18542, 2009.

[121] R. Wang, X.-H. Wang, B.-Y. Gu, and G.-Z. Yang. Effects of shapes and orientations of scatterers and lattice symmetries on the photonic band gap in two-dimensional photonic crystals. *J. Appl. Phys.*, 90:4307, 2001.

[122] A. R. Tao, D. P. Ceperley, P. Sinsermsuksakul, A. R. Neureuther, and P. Yang. Self-Organized Silver Nanoparticles for Three-Dimensional Plasmonic Crystals. *Nano Lett.*, 8:4033, 2008.

[123] X. D. Wang, C. Neff, E. Graugnard, Y. Ding, J. S. King, L. A. Pranger, R. Tannenbaum, Z.L. Wang, and C. J. Summers. Photonic Crystals Fabricated Using Patterned Nanorod Arrays. *Advanced Materials*, 17:2103, 2005.

[124] M. B. Zanjani and J. R. Lukes. Phonon dispersion and thermal conductivity of nanocrystal superlattices using three-dimensional atomistic models. *J. Appl. Phys.*, 115:143515, 2014.

[125] O. L. Lazarenkova and A. A. Balandin. Miniband formation in a quantum dot crystal. *J. Appl. Phys.*, 89:5509, 2001.

[126] D. A. Cheney. *Computational Modeling of Geometry Dependent Phonon Transport in Silicon Nanostructures.* PhD thesis, University of Pennsylvania, 2013.

[127] D. A. Cheney and J. R. Lukes. Comparison of Atomistic and Continuum Methods for Calculating Ballistic Phonon Transmission in Nanoscale Waveguides. *J. Heat Transfer*, 135:091101, 2013.

[128] T. Seetawan and H. Wattanasarn. First Principle Simulation of Mechanical Properties of PbS, PbSe, CdTe and PbTe by Molecular Dynamics. *Procedia Engineering*, 32:609, 2012.

[129] X. Ye, L. Jin, H. Caglayan, J. Chen, G. Xing, C. Zheng, V. Doan-Nguyen, Y. Kang, N. Engheta, C. R. Kagan, and C. B. Murray. Improved Size-Tunable Synthesis of

Monodisperse Gold Nanorods through the Use of Aromatic Additives. *ACS Nano*, 6:2804–2817, 2012.

[130] K. Ueda, T. Dotera, and T. Gemma. Photonic band structure calculations of two-dimensional Archimedean tiling patterns. *Phys. Rev. B*, 75:195122, 2007.

[131] A.-P. Hynninen, J. H. J. Thijssen, E. C. M. Vermolen, and M. Dijkstraand A. van Blaaderen. Self-assembly route for photonic crystals with a bandgap in the visible region. *Nat. Mater.*, 6:202, 2007.

[132] Y. Wan, Z. Cai, L. Xia, L. Wang, Y. Li, Q. Li, and X. S. Zhao. Simulation and fabrication of binary colloidal photonic crystals and their inverse structures. *Materials Letters*, 63:2078, 2009.

[133] R. A. Bernal, R. Agrawal, B. Peng, K. A. Bertness, N. A. Sanford, A. V. Davydov, and H. D. Espinosa. Effect of Growth Orientation and Diameter on the Elasticity of GaN Nanowires. A Combined in Situ TEM and Atomistic Modeling Investigation. *Nano Lett.*, 11:548, 2011.

[134] R. Agrawal, B. Peng, E. E. Gdoutos, and H. D. Espinosa. Elasticity Size Effects in ZnO Nanowires-A Combined Experimental-Computational Approach. *Nano Lett.*, 8(11):3668, 2008.

[135] Sean T. Sivapalan, Brent M. DeVetter, Timothy K. Yang, Matthew V. Schulmerich, Rohit Bhargava, and Catherine J. Murphy. Surface-Enhanced Raman Spectroscopy of Polyelectrolyte-Wrapped Gold Nanoparticles in Colloidal Suspension. *J. Phys. Chem. C*, 117:10677, 2013.

[136] N. W. Ashcroft and N. D. Mermin. *Solid State Physics.* Thomson Learning, 1976.

[137] J. W. Lynn, H. G. Smith, and R. M. Nicklow. Lattice Dynamics of Gold. *Phys. Rev. B*, 8:3493, 1973.

[138] J. Baumgartl, J. Dietrich, J. Dobnikar, C. Bechinger, and H. H. von Grunberg. Phonon dispersion curves of two-dimensional colloidal crystals: the wavelength-dependence of friction. *Soft Matter*, 4:2199, 2008.

[139] B. Kraczek and P. W. Chung. Investigation of direct and indirect phonon-mediated bond excitation in α-RDX. *J. Chem. Phys.*, 138:074505, 2013.

[140] A. F. Bower. *Applied Mechanics of Solids.* Taylor and Francis Group, 2010.

[141] J. A. Barker, M. L. Klein, and M. V. Bobetic. Elastic Constants and Phonon Dispersion Curves for Solid Argon near O K. *Phys. Rev. B*, 2:4176, 1970.

[142] L. Wang and B. Li. Phononics gets hot. *Physics World*, 21:27, 2008.

[143] X. Ding, S.-C. Lin, B. Kiraly, H. Yue, S. Li, I.-K. Chiang, J. Shi, S. J. Benkovic, and T. J. Huang. On-chip manipulation of single microparticles, cells, and organisms using surface acoustic waves. *PNAS*, 109:11105, 2012.

[144] I. Voiculescu and A. N. Nordin. *Microelectromechanical Systems and Devices.* InTech, 2012.

[145] N. Courjal, M. P. Bernal, G. Ulliac, J. Dahadah, S. Benchabane, and J-M. Merolla. LiNbO3 acousto-optical and electrooptical micromodulators. *Journal of European Optical Society*, 4:09018, 2009.

[146] S.-H. Shen, W. Fang, and S.-T. Young. Design considerations for an acoustic MEMS filter. *Microsystem Technologies*, 10:585, 2004.

[147] M. Bisoffi, B. Hjelle, D. C. Brown, D. W. Branch, T. L. Edwards, S. M. Brozik, V. S. Bondu-Hawkins, and R. S. Larson. Detection of viral bioagents using a shear horizontal surface acoustic wave biosensor. *Biosensors and Bioelectronics*, 23:1397, 2008.

[148] I. Voiculescu and A. N. Nordin. Acoustic wave based MEMS devices for biosensing applications. *Biosensors and Bioelectronics*, 33:1, 2012.

[149] H. Jin, J. Zhou, X. He, W. Wang, H. Guo, S. Dong, D. Wang, Y. Xu, J. Geng, J. K. Luo, and W. I. Milne. Flexible surface acoustic wave resonators built on disposable plastic film for electronics and lab-on-a-chip applications. *Sci. Rep.*, 3, 2013.

[150] L. Haofeng, J. Rui, L. Weilong, C. Chen, and L. Xinyu. Surface acoustic wave sensors of delay lines based on MEMS. *J. Nanosci. Nanotechnol.*, 10:7258, 2010.

[151] M. S. Weinberg, B. T. Cunningham, and C. W. Clapp. Modeling Flexural Plate Wave Devices. *J. MEMS*, 9:370, 2000.

[152] A. Bybi, S. Grondel, J. Assaad, A.-C. Hladky-Hennion, C. Granger, and M. Rguiti. Reducing crosstalk in array structures by controlling the excitation voltage of individual elements: A feasibility study. *Ultrasonics*, 53:1135, 2013.

[153] S. Winters, G. Bernhardt, and J. F. Vetelino. A Dual Lateral-Field-Excited Bulk Acoustic Wave Sensor Array. *IEEE Transactions on Ultrasonics, Ferroelectrics, and Frequency Control*, 60:573, 2013.

[154] B. Liang, X. S. Guo, J. Tu, D. Zhang, and J. C. Cheng. An acoustic rectifier. *Nat. Mater.*, 9:989, 2010.

[155] N. Boechler, G. Theocharis, and C. Daraio. Bifurcation-based acoustic switching and rectification. *Nat. Mater.*, 10:665, 2011.

[156] Y. Tanaka, T. Murai, and N. Nishiguchi. Rectification of elastic waves in a thin plate. *J. Appl. Phys.*, 111:024507, 2012.

[157] B. Liang, B. Yuan, and J. C. Cheng. Acoustic diode: Rectification of acoustic energy flux in one-dimensional systems. *Phys. Rev. Lett*, 103:104301, 2009.

[158] Z. J. He, S. S. Peng, Y. T. Ye, Z. W. Dai, C. Y. Qiu, M. Z. Ke, and Z. Y. Liu. Asymmetric acoustic gratings. *Appl. Phys. Lett.*, 98:083505, 2011.

[159] X. Gu, Z. Lin, B. Liang, J. Cheng, and D. Zhang. Modeling and optimization of an acoustic diode based on micro-bubble nonlinearity. *J. Acoust. Soc. Am.*, 133:1119–1125, 2013.

[160] X. F. Li, X. Ni, L. Feng, M. H. Lu, C. He, and Y. F. Chen. Tunable unidirectional sound propagation through a sonic-crystal-based acoustic diode. *Phys. Rev. Lett.*, 106:084301, 2011.

[161] A. E. Miroshnichenko, E. Brasselet, and Yu. S. Kivshar. Reversible optical nonreciprocity in periodic structures with liquid crystals. *Appl. Phys. Lett.*, 96:063302–3, 2010.

[162] A. Alberucci and G. Assanto. All optical isolation by directional coupling. *Opt. Lett.*, 33:1641–1643, 2008.

[163] Z. Yu and S. Fan. Complete optical isolation by indirect interband photonic transition . *Nature Photonics*, 3:91–94, 2009.

[164] H. Lira, Z. Yu, S. Fan, and M. Lipson. Electrically Driven Nonreciprocity Induced by Interband Photonic Transition on a Silicon Chip . *Phys. Rev. Lett.*, 109:033901, 2012.

[165] B. A. Auld. *Acoustic Fields and Waves in Solids.* Krieger Publishing Company, 1990.

[166] P. E. Hopkins, C. M. Reinke, M. F. Su, R. H. Olsson, E. A. Shaner, Z. C. Leseman, J. R. Serrano, L. M. Phinney, and I. El-Kady. Reduction in the Thermal Conductivity of Single Crystalline Silicon by Phononic Crystal Patterning. *Nano Lett.*, 11:107, 2011.

[167] T.-T. Wu, J.-C. Hsu, and J.-H. Sun. Phononic Plate Waves. *IEEE Transactions on Ultrosonics, Ferroelectrics, and Frequency Control*, 58:2146, 2011.

[168] X. Dong, Y. Ye, B. Wang, C. Qiu, M. Ke, and Z. Liu. Experimental demonstration of the acoustic frequency conversions by temporal phononic crystals. *arXiv:1305.1550 [cond-mat.mtrl-sci]*, 2013.

[169] D. W. Wright and R. S. Cobbold. Acoustic wave transmission in time-varying phononic crystals. *Smart. Matter. Struct.*, 18:015008, 2009.

[170] J.-H. Jang, C. K. Ullal, T. Gorishnyy, V. V. Tsukruk, and E. L. Thoma. Mechanically Tunable Three-Dimensional Elastomeric Network/Air Structures via Interference Lithography. *Nano Lett.*, 6:740, 2006.

[171] F. Casadei, T. Delpero, A. Bergamini, P. Ermanni, and M. Ruzzene. Piezoelectric resonator arrays for tunable acoustic waveguides and metamaterials. *J. Appl. Phys.*, 112:064902, 2012.

[172] J. R. Cullen, S. Rinaldi, and G. V. Blessing. Elastic versus magnetoelastic anisotropy in rare earthiron alloy. *J. Appl. Phys.*, 49:1960, 1978.

[173] Z. Varga, G. Filipcsei, and M. Zrinyi. Magnetic field sensitive functional elastomers with tuneable elastic modulus. *Polymer*, 47:227, 2006.

[174] K. S. Novoselov, A. K. Geim, S. V. Morozov, D. Jiang, Y. Zhang, S. V. Dubonos, I. V. Grigorieva, and A. A. Firsov. Electric Field Effect in Atomically Thin Carbon Films. *Science*, 306:666, 2004.

[175] A. K. Geim and K. S. Novoselov. The rise of graphene. *Nat. Mater.*, 6:183, 2007.

[176] J. C. Meyer, A. K. Geim, M. I. Katsnelson, K. S. Novoselov, T. J. Booth, and S. Roth. The structure of suspended graphene sheets. *Nature*, 446:60, 2007.

[177] X. Jia, M. Hofmann, V. Meunier, B. G. Sumpter, J. Campos-Delgado, J. M. Romo-Herrera, H. Son, Y.-P. Hsieh, A. Reina, J. Kong, M. Terrones, and M. S. Dresselhaus. Controlled Formation of Sharp Zigzag and Armchair Edges in Graphitic Nanoribbons. *Science*, 323:1701, 2000.

[178] D. S. Bethune, C. H. Kiang, M. S. De Vries, G. Gorman, R. Savoy, J. Vazquez, and R. Beyers. Cobalt-catalysed growth of carbon nanotubes with single-atomic-layer walls. *Nature*, 363:605, 1993.

[179] N. G. Chopra, R. J. Luyken, K. Cherrey, V. H. Crespi, M. L. Cohen, S. G. Louie, and A. Zettl. Boron Nitride Nanotubes. *Science*, 269:966, 1995.

[180] Z.-G. Chen, J. Zou, G. Liu, F. Li, Y. Wang, L. Wang, X.-L. Yuan, T. Sekiguchi, H.-M. Cheng, and G. Q. Lu. Novel Boron Nitride Hollow Nanoribbons. *Science*, 2:2183, 2008.

[181] Y. J. Chen, H. Z. Zhang, and Y. Chen. Pure boron nitride nanowires produced from boron triiodide. *Nanotechnology*, 17:786, 2006.

[182] A. P. Suryavanshi, M.-F. Yu, J. Wen, C. Tang, and Y. Bando. Elastic modulus and resonance behavior of boron nitride nanotubes. *Appl. Phys. Lett.*, 84:2527, 2004.

[183] K. F. Mak, C. Lee, J. Hone, J. Shan, and T. F. Heinz. Atomically Thin MoS2: A New Direct-Gap Semiconductor. *Phys. Rev. Lett.*, 105:136805, 2010.

[184] Y. Zhang, Y.-W. Tan, H. L. Stormer, and P. Kim. Experimental observation of the quantum Hall effect and Berry's phase in graphene. *Nature*, 438:201, 2005.

[185] K. Wakabayashi, Y. Takane, and M. Sigrist. Perfectly Conducting Channel and Universality Crossover in Disordered Graphene Nanoribbons. *Phys. Rev. Lett.*, 99:036601, 2007.

[186] A. Vakil and N. Engheta. Transformation Optics Using Graphene. *Science*, 332:1291, 2011.

[187] M. Liu, X. Yin, E. Ulin-Avila, B. Geng, T. Zentgraf, L. Ju, F. Wang, , and X. Zhang. A graphene-based broadband optical modulator. *Nature*, 474:64, 2011.

[188] S. Ghosh, W. Bao, D. L. Nika, S. Subrina, E. P. Pokatilov, C. N. Lau, and A. A. Balandin. Dimensional crossover of thermal transport in few-layer graphene. *Nat. Mater.*, 9:555, 2010.

[189] A. A. Balandin, S. Ghosh, W. Bao, I. Calizo, D. Teweldebrhan, F. Miao, and C. N. Lau. Superior Thermal Conductivity of Single-Layer Graphene. *Nano Lett.*, 8:902, 2008.

[190] D. Li and R. B. Kaner. Graphene-Based Materials. *Science*, 320:1170, 2008.

[191] C. Lee, X. Wei, J. W. Kysar, and J. Hone. Measurement of the Elastic Properties and Intrinsic Strength of Monolayer Graphene. *Science*, 321:1170, 2008.

[192] Q. Tang and Z. Zhou. Graphene-analogous low-dimensional materials. *Progress in Materials Science*, 58:1244, 2013.

[193] T. Rueckes, K. Kim, E. Joselevich, G. Y. Tseng, C. L. Cheung, and C. M. Lieber. Carbon Nanotube-Based Nonvolatile Random Access Memory for Molecular Computing. *Science*, 289:94, 2000.

[194] J. E. Jang, S. N. Cha, Y. J. Choi, D. J. Kang, T. P. Butler, D. G. Hasko, J. E. Jung, J. M. Kim, and G. A. J. Amaratunga. Nanoscale memory cell based on a nanoelectromechanical switched capacitor. *Nature Nanotechnol.*, 3:26, 2008.

[195] E. U. Stutzel, M. Burghard, K. Kern, F. Traversi, F. Nichele, and R. Sordan. A Graphene Nanoribbon Memory Cell. *Small*, 6:2822, 2010.

[196] M. Begliarbekov, S. Strauf, and C. P. Search. Quantum inductance and high frequency oscillators in graphene nanoribbons. *Nanotechnology*, 22:165203, 2011.

[197] J. S. Bunch, A. M. van der Zande, S. S. Verbridge, I. W. Frank, D. M. Tanenbaum, J. M. Parpia, H. G. Craighead, and P. L. McEuen. Electromechanical Resonators from Graphene Sheets. *Science*, 315:490, 2007.

[198] C. Chen, S. Rosenblatt, K. I. Bolotin, W. Kalb, P. Kim, I. Kymissis, H. L. Stormer, T. F. Heinz, and J. Hone. Performance of monolayer graphene nanomechanical resonators with electrical readout. *Nat. Nanotechnol.*, 4:861, 2009.

[199] D. Garcia-Sanchez, A. M. van der Zande, A. San Paulo, B. Lassagne, P. L. McEuen, and A. Bachtold. Imaging Mechanical Vibrations in Suspended Graphene Sheets. *Nano Lett.*, 8:1399, 2008.

[200] F. Scarpa, R. Chowdhury, K. Kam, S. Adhikari, and M. Ruzzene. Dynamics of mechanical waves in periodic graphene nanoribbon assemblies. *Nanoscale Research Lett.*, 6:430, 2011.

[201] H. G. Craighead. Nanoelectromechanical Systems. *Science*, 290:1532, 2000.

[202] S. S. Verbridge, D. F. Shapiro, H. G. Craighead, and J. M. Parpia. Macroscopic Tuning of Nanomechanics: Substrate Bending for Reversible Control of Frequency and Quality Factor of Nanostring Resonators. *Nano Lett.*, 7:1728, 2007.

[203] S. J. Papadakis, A. R. Hall, P. A. Williams, L. Vicci, M. R. Falvo, R. Superfine, and S. Washburn. Resonant Oscillators with Carbon-Nanotube Torsion Springs. *Phys. Rev. Lett.*, 93:146101, 2004.

[204] B. Ilic, S. Krylov, and H. G. Craighead. Theoretical and experimental investigation of optically driven nanoelectromechanical oscillators. *J. Appl. Phys.*, 107:034311, 2010.

[205] S. S. Verbridge, L. M. Bellan, J. M. Parpia, and H. G. Craighead. Optically Driven Resonance of Nanoscale Flexural Oscillators in Liquid. *Nano Lett.*, 6:2109, 2006.

[206] E. Forsen, G. Abadal, S. Ghatnekar-Nilsson, J. Teva, J. Verd, R. Sandberg, W. Svendsen, F. Perez-Murano, J. Esteve, E. Figueras, F. Campabadal, L. Montelius, N. Barniol, and A. Boisen. Ultrasensitive mass sensor fully integrated with complementary metal-oxide-semiconductor circuitry. *Appl. Phys. Lett.*, 87:043507, 2005.

[207] I. De Vlaminck, J. Roels, D. Taillaert, D. Van Thourhout, R. Baets, L. Lagae, and G. Borghs. Detection of nanomechanical motion by evanescent light wave coupling. *Appl. Phys. Lett.*, 90:233116, 2007.

[208] H. J. Mamin and D. Rugar. Sub-attonewton force detection at millikelvin temperatures. *Appl. Phys. Lett.*, 79:3358, 2001.

[209] R. G. Knobel and A. N. Cleland. Nanometre-scale displacement sensing using a single electron transistor. *Nature (London)*, 424:291, 2003.

[210] G. G. Yaralioglu, A. Atalar, S. R. Manalis, and C. F. Quate. Analysis and design of an interdigital cantilever as a displacement sensor. *J. Appl. Phys.*, 83:7405, 1998.

[211] S. R. Manalis, S. C. Minne, A. Atalar, and C. F. Quate. Interdigital cantilevers for atomic force microscopy. *Appl. Phys. Lett.*, 69:3944, 1996.

[212] B. Ilic, Y. Yang, K. Aubin, R. Reichenbach, S. Krylov, and H. G. Craighead. Enumeration of DNA Molecules Bound to a Nanomechanical Oscillator. *Nano Lett.*, 5:925, 2005.

[213] B. Ilic, D. Czaplewski, H. G. Craighead, P. Neuzil, C. Campagnolo, and C. Batt. Mechanical resonant immunospecific biological detector. *Appl. Phys. Lett.*, 77:450, 2000.

[214] M. B. Zanjani, A. R. Davoyan, A. M. Mahmoud, N. Engheta, and J. R. Lukes. One-way Phonon Isolation In Acoustic Waveguides. *Appl. Phys. Lett.*, 104:081905, 2014.

[215] R. Fleury, D. L. Sounas, C. F. Sieck, M. R. Haberman, and A. Alu. Sound Isolation and Giant Linear Nonreciprocity in a Compact Acoustic Circulator. *Science*, 343:516, 2014.

[216] B.-I. Popa and S. A. Cummer. Non-reciprocal and highly nonlinear active acoustic metamaterials. *Nat. Comm.*, 5:3398, 2014.

[217] T. Murmu and S. C. Pradhan. Vibration analysis of nano-single-layered graphene sheets embedded in elastic medium based on nonlocal elasticity theory. *J. Appl. Phys.*, 105:064319, 2009.

[218] J. Shi, Q. Ni, X. Li, and T. Natsuki. Wave propagation in embedded double-layer graphene nanoribbons as electromechanical oscillators. *J. Appl. Phys.*, 110:084321, 2011.

[219] G. Allegri, F. Scarpa, R. Chowdhury, and S. Adhikari. Wave Propagation in Periodically Supported Nanoribbons: A Nonlocal Elasticity Approach. *J. Vibration and Acoustics*, 135:041017, 2013.

[220] A. D. Senalp, A. Arikoglu, I. Ozkol, and V. Z. Dogan. Dynamic response of a finite length euler-bernoulli beam on linear and nonlinear viscoelastic foundations to a concentrated moving force. *J. Mech. Sci. Technol.*, 24:1957, 2010.

[221] A. Bhaskar. Elastic waves in Timoshenko bemas: the 'lost and found' of an eigenmode. *Proc. R. Soc. A*, 465:239, 2009.

[222] J. Yoon, C. Q. Ru, and A. Mioduchowski. Vibration of an embedded multiwall carbon nanotube. *Compos. Sci. Technol.*, 63:1533, 2003.

[223] Q. Wang. Wave propagation in carbon nanotubes via nonlocal continuum mechanics. *J. Appl. Phys.*, 98:124301, 2005.

[224] T. Natsuki, T. Hayashi, , and M. Endo. Wave propagation of carbon nanotubes embedded in an elastic medium. *J. Appl. Phys.*, 97:044307, 2005.

[225] S. T. Peng. Rigorous Analogies between Elastic and Electromagnetic Systems. *J Appl. Phys.*, 1:87–91, 1973.

[226] J. M. Carcione and F. Cavallini. On the acoustic-electromagnetic analogy. *Wave Motion*, 21:149–162, 1995.